Light absorption of atmospheric soot particles over Central Europe

Der Fakultät für Physik und Geowissenschaften

der Universität Leipzig

eingereichte

DISSERTATION

zur Erlangung des akademischen Grades

Doctor rerum naturalium

(Dr. rer. nat.)

vorgelegt

von Dipl.-Met. Stephan Nordmann

geboren am 19. Januar 1982 in Köthen

Leipzig, den 06. November 2012

Gutachter: Prof. Dr. Alfred Wiedensohler
Prof. Dr. Gregory R. Carmichael
Tag der Verleihung: 18.03.2013

Bibliographic description

Nordmann, Stephan

Light absorption of atmospheric soot particles over Central Europe

University of Leipzig, Dissertation

102 pp.[1], 142 Ref.[2], 49 Fig.[3], 7 Tab.[4]

Abstract

Soot particles are important components of the atmosphere; they play a significant role in the balance of global climate, and also contribute to adverse effects upon human health. Soot particles are usually emitted as a result of incomplete combustion of fossil fuels and biomass. The current anthropogenic emission rates are highly uncertain, both on regional and global scale, which can be partly attributed to different experimental methods for the quantification of soot. This uncertainty propagates in estimations of the radiative forcing by regional models.

In the atmosphere, soot particles influence the radiation balance by absorbing visible sunlight. It is important to note that the mass absorption coefficient, which is highly relevant for radiative forcing calculations, is not constant but can increase during atmospheric aging processes, changing the state of mixture of soot. Current values of the mass absorption coefficient, available in literature show a large variability. It is not clear if this variability is due to the state of mixture of soot or different measurement devices.

In the present work, a new method for determining the mass absorption coefficient based on successive measurements of the light absorption coefficient and soot mass concentration of atmospheric samples is presented. Basically, the soot mass concentration in an atmospheric particle sample from Multi Angle Absorption Photometer (MAAP) measurements is subsequently determined by Raman-spectroscopy. As a representative data basis, a large number of atmospheric samples are available from different observation sites of the German Ultrafine Aerosol Network (GUAN), ranging from traffic-related sites, regional background sites to mountain sites in Central Europe. The derived mass absorption coefficients for selected samples are discussed regarding their state of mixture using a microphysical optical model.

Based on these insights, a validation of the meso-scale Weather Research and Forecast (WRF) model on-line coupled with a chemistry module (WRF-Chem) is performed for Europe by using a high resolution soot emission inventory. The simulated absorption behavior is adjusted by using measured mass absorption coefficients, in order to account for the true mixing state of atmospheric soot particles. Based on the predictions of the WRF model for one selected episode, new quantitative values for the radiative forcing of soot particles in the troposphere over Europe are derived.

[1]Number of pages
[2]Number of references
[3]Number of figures
[4]Number of tables

Bibliographische Beschreibung

Nordmann, Stephan

Light absorption of atmospheric soot particles over Central Europe

Universität Leipzig, Dissertation

102 pp.[1], 142 Ref.[2], 49 Fig.[3], 7 Tab.[4]

Referat

Rußpartikel sind bedeutende Komponenten in der Atmosphäre. Sie spielen eine wichtige Rolle in der globalen Strahlungsbilanz und haben negative Effekte auf die menschliche Gesundheit. Rußpartikel werden als ein Produkt unvollständiger Verbrennung fossiler Energieträger und Biomasse emittiert. Aktuelle globale und regionale Emissionsraten sind sehr unsicher, was teilweise auf unterschiedliche Messmethoden von Rußpartikeln zurückgeführt werden kann. Diese Unsicherheiten pflanzen sich in den Berechnungen zum Strahlungsantrieb durch Modelle fort.
Die Strahlungsbilanz in der Atmosphäre wird durch die Absorption sichtbaren Sonnenlichtes durch Rußpartikel beeinflusst. Das Absorptionsverhalten wird dabei maßgeblich durch den Mischungszustand des Rußes mit anderen chemischen Komponenten beeinflußt. Für die Berechnung ihres Strahlungsantriebes sind Massenabsorptionskoeffizienten von großer Bedeutung, da sie vom Mischungszustand abhhängig sind. Aktuelle Literaturwerte zeigen eine große Variabilität des Massenabsorptionskoeffizienten. Es ist jedoch nicht klar, ob die Variabilität durch Veränderungen im Mischungszustand oder unterschiedliche Messmethoden für Ruß hervorgerufen wird.
In der vorliegenden Arbeit wird eine neue Methode zur Bestimmung atmosphärischer Massenabsorptionskoeffizienten vorgestellt. Sie beruht auf aufeinander folgende Messungen der Lichtabsorption und der Rußmassenkonzentration für ein und dieselbe atmosphärische Partikelprobe. Zur Lichtabsorptionsmessung werden Mehrwinkelabsorptionsphotometer und zur Messung der Rußmassenkonzentration ein Raman-Spektrometer verwendet. Eine repräsentative Basis atmosphärischer Partikelproben aus verkehrsnahen, regionalen und Mittelgebirgsstationen wurden im deutschen Messnetz für ultrafeine Partikel (engl. German Ultrafine Aerosol Network, GUAN) gesammelt. Für ausgewählte Proben wurden Massenabsorptionskoeffizienten bestimmt und mit einem mikrophysikalischen partikeloptischen Modell hinsichtlich des Effektes des Mischungszustandes diskutiert.
Basierend auf diesen Erkenntnissen wird das mesoskalige Wettermodell (engl. Weather Research and Forecast model, WRF), welches mit einem Chemiemodul gekoppelt ist (WRF-Chem) für Europa validiert. Für die Berechnungen werden neue und räumlich hochaufgelöste Emissionsdaten von Rußpartikeln verwendet. Das im Modell simulierte Absorptionsverhalten wird unter Verwendung der Massenabsorptionskoeffiezienten an die Messungen angepasst, um so den wahren Mischungszustand von atmosphärischen Rußpartikeln indirekt zu berücksichtigen. Mit diesen Berechnungen werden neue Werte des Strahlungsantriebes von Rußpartikeln in der Troposphäre über Europa vorgestellt.

[1] Anzahl der Seiten
[2] Anzahl der im Literaturverzeichnis ausgewiesenen Literaturangaben
[3] Anzahl der Abbildungen
[4] Anzahl der Tabellen

Contents

List of Figures

List of Tables

List of Abreviations

GUAN	**G**erman **U**ltrafine **A**erosol **N**etwork
BC	**B**lack **C**arbon
OC	**O**rganic **C**arbon
EC	**E**lemental **C**arbon
TC	**T**otal **C**arbon
GC	**G**raphitic **C**arbon
MAAP	**M**ulti **A**ngle **A**bsorption **P**hotometer
PSAP	**P**article **S**oot **A**bsorption **P**hotometer
PM	Particulate Matter
D_1	Raman active mode of soot at $1300\,cm^{-1}$
D_2	Raman active mode of soot at $1620\,cm^{-1}$
D_3	Raman active mode of soot at $1500\,cm^{-1}$
D_4	Raman active mode of soot at $1140\,cm^{-1}$
G	Raman active mode of soot at $1600\,cm^{-1}$
TOA	**T**op **O**f the **A**tmopshere
SMPS	**S**canning **M**obility **P**article **S**izer
TDMPS	**T**win **D**ifferential **M**obility **P**article **S**izer
DMA	**D**ifferential **M**obility **A**nalyzer
CPC	**C**ondensation **P**article **C**ounter
UBA	federal environmental agency (Umweltbundesamt)
DWD	German meteorological service (**D**eutscher **W**etter**d**ienst)
IfT	**I**nstitute **f**or **T**ropospheric Research
EMEP	**E**uropean **M**onitoring and **E**valuation **P**rogramme
EUCAARI	European Integrated Project on Aerosol-Cloud-Climate-Air Quality Interactions
ARCTAS	**A**rctic **R**esearch of the **C**omposition of the **T**roposphere from **A**ircraft and **S**atellites
WRF	**W**eather **R**esearch and **F**orecast model
MOSAIC	**MO**del for **S**imulating **A**erosol **I**nteractions and **C**hemistry
MEGAN	**M**odel of**E**missions of **G**ases and **A**erosols from **N**ature
VOC	**V**olatile **O**rganic **C**ompounds
MODIS	**MO**derate resolution **I**maging **S**pectroradiometer
AERONET	**AE**rosol **RO**botic **NET**work

Notation

δ_{GC}	mass absorption coefficient concerning graphitic carbon (m^2g^{-1})
δ_{EC}	mass absorption coefficient concerning elemental carbon (m^2g^{-1})
δ_{mod}	mass absorption coefficient from model (m^2g^{-1})
σ_{ap}	absorption coefficient (Mm^{-1})
σ_{sca}	scattering coefficient (Mm^{-1})
σ_{ext}	extinction coefficient (Mm^{-1})
AOT	aerosol optical thickness (dimensionless)
D_p	particle diameter (m)
D_{p_g}	geometric mean diameter (m)
σ_g	geometric standard deviation (m)
$\frac{dN}{d\log D_p}$	particle number size distribution (cm^{-3})
$\frac{dN_s}{d\log D_p}$	soot particle number size distribution (cm^{-3})
$\frac{dV}{d\log D_p}$	particle volume size distribution ($\mu m^3 cm^{-3}$)
$\frac{dV_s}{d\log D_p}$	soot particle volume size distribution ($\mu m^3 cm^{-3}$)
$\frac{dV_{ext,s}}{d\log D_p}$	externally mixed soot particle volume size distribution ($\mu m^3 cm^{-3}$)
$\frac{dV_{int,s}}{d\log D_p}$	internally mixed soot particle volume size distribution ($\mu m^3 cm^{-3}$)
$\frac{dV_{int,ns}}{d\log D_p}$	internally mixed none-soot particle volume size distribution ($\mu m^3 cm^{-3}$)
N	total particle number concentration(cm^{-3})
m	mass concentration ($\mu g\, m^{-3}$)
m_{GC}	mass concentration of graphitic carbon ($\mu g\, m^{-3}$)
m_{EC}	mass concentration of elemental carbon ($\mu g\, m^{-3}$)
m_{BC}	mass concentration of balck carbon ($\mu g\, m^{-3}$)
m_{load}	mass load on glass microfiber filters ($\mu g\, cm^{-2}$)
A_{spot}	loaded spot diameter on glass microfiber filters (cm^{-2})
t_{samp}	sampling time (s)
$\dot{V}$	flow rate ($l\, min^{-1}$)
ρ_p	particle density ($g\, cm^{-3}$)
x	size parameter (dimensionless)
λ	wavelength (nm)
ω	frequency (Hz)
k	wavenumber (cm^{-1})
C_{sca}	scattering cross section (m^2)
C_{ext}	extinction cross section (m^2)
C_{ap}	absorption cross section (m^2)
a_n	expansion coefficient for the scattered field

b_n	expansion coefficient for the scattered field
SSA	single scattering albedo (dimensionless)
F	radiant flux density ($\mathrm{W\,m^{-2}}$)
ϵ	externally mixed soot fraction (dimensionless)
D_{core}	diameter of the the concentric soot inclusion in a mixed spherical particle (m)
MB	mean bias
MNB	mean normalized bias (dimensionless)
R	Pearson correlation coefficient (dimensionless)
$RMSE$	root mean square error

1. Introduction

Soot particles are a product of an incomplete combustion of fossil fuels and biomass. On a global scale, soot particles emerge predominantly from man-made processes although natural sources exist as well. Ice core analysis taken in Greenland (McConnell et al., 2007), for example, show that soot particles had been present in the atmosphere already long before the industrialization. The derived concentrations showed a strong temporal variability and were attributed to biomass burning. After 1850, the concentrations rapidly increased to their maximum around 1920, which is associated with the combustion of fossil fuels, such as coal. After 1950, the concentrations decreased to their current level, although the energy consumption increased. The reason for the decrease is possibly the improvement of technological processes. Present-day emissions are mainly due to a combination of biomass and fossil fuel burning. Largest amounts of soot from fossil fuel burning are currently emitted in industrialized countries of the northern hemisphere as a result of more or less controlled energy production processes. Biomass burning of savanna, forests and agricultural waste dominate the soot emissions in Africa and South America (Bond et al., 2004). Soot particles are chemically rather inert with particle diameters around 100 nm being the most frequent, so that they may be transported across the globe even to the remotest regions like the Arctic (Heintzenberg, 1982).

Soot particles are good absorbers of solar radiation. They are characterized by an ability to absorb shortwave radiation across a broad spectral region and thereby heating their environment. Because of this absorption, soot decreases the reflectivity of the surface-atmosphere-cloud system. Deposited on snow, it may also lower its reflectivity. On global scale, the direct radiative forcing of soot is positive at top of the atmosphere and negative at the surface, leading to an overall warming effect (Ramanathan and Carmichael, 2008). Moreover, if soot particles are incorporated into cloud processes they may reduce cloud cover by heating their environment (Ackerman et al., 2000), which is also designated as the semi-direct effect. The Intergovernmental Panel on Climate Change (IPCC, Forster et al. (2007)) summarized the positive direct radiative forcing of soot to be in the range of Methane, but with a large uncertainty. Reported values of the radiative forcing are $0.2 \pm 0.15\,\mathrm{W\,m^{-2}}$ for soot from the combustion of fossil fuel, $0.03 \pm 0.12\,\mathrm{W\,m^{-2}}$ for soot from biomass burning and $0.1 \pm 0.1\,\mathrm{W\,m^{-2}}$ for soot deposited on snow. Besides the effect on climate, soot has an effect on human health. They may influence the cardiovascular system of the human body (Peters et al., 2000) and are carcinogenic.

Primary soot particles have a spherical shape and are decomposed of graphitic layers. Shortly after emission, these primary particles aggregate and form fractal shaped clusters. During atmospheric aging processes, their corresponding optical and microphysical properties may change as a result of internal mixture due to coagulation, condensation, or chemical reactions on the particle surfaces. The associated change in state of mixture makes their uniform detection across all the stages of their aging process difficult. There are many definitions for soot in literature,

basically depending on the method of their determination. Photometric methods base on the change in light transmittance through a particle laden filter medium. The change in transmittance may be due to scattering and absorption of light by the particles. Excluding the change due to scattering, the absorption coefficient may be derived. It can be converted to a mass concentration of black carbon (BC), applying a mass absorption coefficient. It is obvious that the term black carbon entirely accounts for the absorptive properties of soot. Another principle is the photoacoustic measurement. Particles are irradiated with periodically modulated visible light. Because of absorption by soot particles, this leads to a periodical change in heat transfer from the particles to the carrier gas. This, in turn, leads to small pressure changes and hence to a measurable acoustic signal (Petzold and Niessner, 1996). It is proportional to light absorption and therefore to BC mass concentrations. A relatively new technique is measuring soot particles by laser induced incandescence. The measurement principle is based on the heating of soot by intensive laser light until evaporation. The evaporation temperature is very high, so that radiation in the near-infrared spectral region is emitted. The emitted radiation is, in turn, characteristic for the composition of the analyzed particle (Schwarz et al., 2006). A common approach measuring atmospheric soot particles is based on the heating of the sample in certain temperature steps. In a first step, the organic carbon (OC) fraction is released in an helium or nitrogen atmosphere. Further heating of the sample in an oxygen-containing atmosphere leads to the pyrolysis of the elemental carbon (EC) fraction. EC is associated with BC, but not necessarily the same.

Another method, which is sensitive to the graphitic structures in soot particles is Ramanspectroscopy. The species measured with this method is therefore designated as graphitic carbon (GC). Rosen and Novakov (1977) unambiguously identified GC in atmospheric samples by Raman spectroscopy based on the characteristic band structure in the spectrum. In the following years, the application of Raman spectroscopy in atmospheric studies on GC was rare. Ivleva et al. (2007) applied Raman microspectroscopy for the analysis of soot, humic like substances (HULIS) and inorganic compounds in size resolved atmospheric particle samples. They found that GC from the samples is nearly similar to diesel soot in terms of their Raman signal. In addition, they found a difference in spectral features between spring/autumn and summer/winter samples. Signals from multiple chemical components such as sulphate, nitrate and GC in some Raman spectra were attributed to an internal mixed state of atmospheric particles. In addition, mineral particles could be identified by Raman spectroscopy (Batonneau et al., 2006). In several studies it was shown that multi-wavelength Raman spectroscopy can be used to determine the reactivity of diesel soot (Schmid et al., 2011).

Keller and Heintzenberg (1997) developed a method for the quantification of GC in atmospheric particle samples on polycarbonate filters by near infrared Fourier-transform (NIR-FT) Raman spectroscopy. Mertes et al. (2004) further developed this method to derive the GC content in particle samples on quartz fiber filters by NIR-FT Raman spectroscopy. Here, a new method is presented following these approaches. It is capable for the determination of GC on glass microfiber filters applied in a continuously operating absorption photometer (Multi Angle Absorption Photometer, MAAP). The method is calibrated for a mass determination using gravimetric measurements of particle samples containing well characterized test soot. Since the absorption

coefficient is measured by the MAAP, two independent measurements for individual samples on glass microfiber filters are available. This enables a determination of the atmospheric mass absorption coefficient concerning GC (δ_{GC}) as an important property of soot particles, since it may be directly applied in radiative transfer calculation. The application of this method on a broad spectrum of atmospheric particle samples with traffic to mountain characteristics from the German Ultrafine Aerosol Network (GUAN), allows a systematic analysis of δ_{GC}. Moreover, the continuous sampling inside the MAAP with a minimum of maintenance enables a subsequent selection of specific episodes to be analyzed with respect to δ_{GC}. With the aid of other measurements characterizing atmospheric particles concerning their size distribution in combination with a microphysical-optical model, the reason for changes in δ_{GC} will be examined. Current values from literature show a large span depending mainly on the particle composition, especially on the mixing state. The microphysical optical model will be used to analyze the mixing state of soot particles. A large fraction of the observed span is may be also due to the usage of different measurement devices for the absorption coefficient as well as the mass concentrations. Since mass concentrations of EC are often related to the absorption coefficient in other studies, the mass absorption coefficient concerning EC (δ_{EC}) is mostly available in literature. The relation between δ_{GC} and δ_{EC} will be discussed throughout this study.
In this work, the Weather Research and Forecast model coupled with a chemical transport module (WRF-Chem) will be used for estimating the radiative forcing of soot particles in Central Europe during an episode for which values of δ_{GC} were determined with the new Raman method. The model will first be extensively validated using aerosol measurements from the GUAN network. A sensitivity study of soot mass concentrations on emissions will be carried out in order to improve their simulations. The model values of mass absorption coefficient (δ_{mod}) will be adjusted to measurements of δ_{GC}, in order to improve the simulations of soot light absorption and calculate a reliable radiative forcing.

2. Theoretical Background

2.1. Life-cycle of atmospheric soot particles

Soot particles are a product of incomplete combustion processes, with usually either biomass or fossil fuel as a combustible. Their morphological structure and chemical properties depend on the conditions (e.g. temperature) during and shortly after the combustion process and will be explained in more detail in Section 2.3.3. According to a comprehensive inventory (Bond et al., 2004), global emissions of BC are estimated to be $8\,\mathrm{tg\,yr^{-1}}$ as illustrated in Figure 2.1. This global emission rate is, however, uncertain by a factor of 2. Open biomass burning of savanna or forests play an important role, since it accounts for 41 % of all BC emissions. The most important producers of anthropogenic BC emissions are industry (15 %), transport (12 %) and domestic (26 %), which account for the combustion of coal, diesel fuel, agricultural waste and other burnable material. Freshly emitted particles from high-temperature combustion are aggregates of small spherical primary particles, which usually have 100 nm and less as a typical diameter. Under favourable conditions fractal aggregates with sizes up to 1 μm may form. Fresh produced soot particles are "fluffy" and highly hydrophobic (Weingartner et al., 1997). During atmospheric aging processes these open fractal aggregates collapse to more compact and often nearly spherical clusters. Due to condensation of gaseous compounds or coagulation with other non-soot particles, a fraction of this carbonaceous species may further grow and thereby becoming internally mixed and more hydrophilic. Usually, this change in mixing state completely changes the particle's chemical reactivity, its activation behaviour to cloud droplets, and the optical properties of atmospheric soot particles. Due to a typical lifetime between 2 and 10 days (Ogren and Charlson, 1983; Cooke and Wilson, 1996), soot particles may be transported over long distances. An important removal process is wet deposition as evidenced from analyzing rain water samples in tropical (Ducret and Cachier, 1992) and rural continental sites (Ogren et al., 1984). It is not clear if this is a result of a collision of internally or externally mixed soot particles with rain droplets below the cloud or due to activation of internally mixed soot particles to cloud droplets. Dry deposition is of minor importance, because of particles sizes and associated deposition velocities. Soot may also be deposited in snow, thereby accelerates its melting and reduces the surface albedo (Clarke and Noone, 1985).

Due to their absorptive effect on incoming solar radiation, soot particles exert a positive net direct radiative forcing at top of the atmosphere as will be defined in Section 2.4. The Intergovernmental Panel on Climate Change (IPCC, Forster et al. (2007)) summarized the globally and anually averaged fossil fuel BC radiative forcing to be $0.2 \pm 0.15\,\mathrm{W\,m^{-2}}$. The radiative forcing of BC from biomass burning is estimated to be $0.03 \pm 0.12\,\mathrm{W\,m^{-2}}$. The effect of BC deposited on snow is $0.1 \pm 0.1\,\mathrm{W\,m^{-2}}$ with a low level of scientific understanding. A comparison of these values with the radiative forcing of Methane ($0.48 \pm 0.05\,\mathrm{W\,m^{-2}}$) shows the strong effect of BC

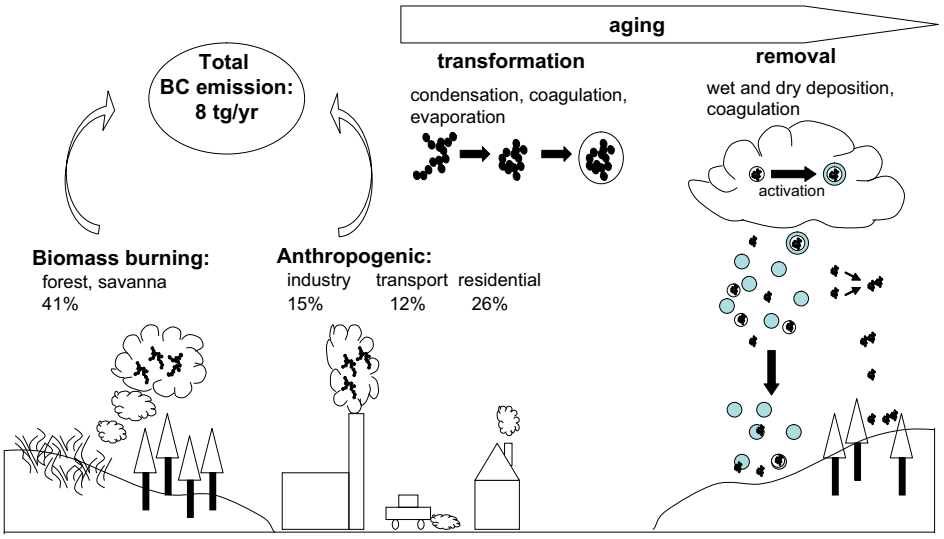

Figure 2.1.: *Soot life cycle from emission (numbers taken from Bond et al. (2004)), over modifications from an external to an internal mixture to important removal processes like wet deposition.*

on the radiation balance in the atmosphere.

2.2. Particle number size distributions

Aerosols are defined as liquid or solid particles suspended in gas as a whole. Atmospheric aerosols cover a wide range of sizes between a few nanometer and tens of micrometer. They may be represented by their number size distribution, which is the number of particles classified in size bins and covering the appropriate size range. To make number concentrations in bins with a different width comparable to each other, the number in each bin is normalized by the width. Since size distributions of atmospheric particles cover a broad size range, the bins are often chosen, so that their width is the same on a logarithmic scale. The resulting normalized number concentration is then designated as $\frac{dN}{d\log D_p}$. The total particle number may be obtained by the integral

$$N = \int_{D_{p1}}^{D_{p2}} \frac{dN}{d\log D_p} dD_p. \tag{2.1}$$

Since in practice the number size distribution is no continuous function, the integral has to be replaced by a sum. The total particle number is also called the zero'th moment of the number size distribution. The total particle mass is the third moment and is calculated from

$$m = \frac{\rho_p \pi}{6} \int_{D_{p1}}^{D_{p2}} {D_p}^3 \frac{dN}{d\log D_p} dD_p \tag{2.2}$$

with ρ_p being the particle density. Atmospheric particle number size distributions may be approximated by a set of overlapping log-normal functions. Log-normal distributions are calculated using the geometric mean diameter D_{p_g} with

$$\log D_{p_g} = \frac{\sum_i n_i \log D_{pi}}{N} \tag{2.3}$$

and the geometric standard deviation σ_g with

$$\log \sigma_g = \left(\frac{\sum_i n_i (\log D_{pi} - \log\ D_{p_g})^2}{N-1} \right)^{\frac{1}{2}}. \tag{2.4}$$

Here, n_i is the number of particles in each bin. Using D_{p_g} and σ_g, the number size distribution may be approximated by a log-normal function with

$$\frac{dN}{d \log D_p} = \frac{N}{\sqrt{2\pi} \log \sigma_g} \exp\left(-\frac{(\log D_p - \log D_{p_g})^2}{2(\log \sigma_g)^2} \right). \tag{2.5}$$

Different diameter definitions are commonly used. The aerodynamic diameter is the diameter a spherical particle with unit density would have if it settles with the same velocity as the actual, perhaps non-spherical, particle. The settling velocity, in turn, is derived from the condition that the drag force on the particle is equal and opposite of the gravity force. The volume equivalent diameter is the diameter of a sphere that has the same volume as the particle under consideration. Considering the motion of a particle in an electric field, the mobility diameter can be defined. It is the diameter of a sphere that has the same electrical mobility as the measured particle. When measuring aerosol particles with light scattering techniques, the optical diameter is used, which depends on the chemical composition, size and the shape of the detected particle. Since in reality not all particles have a spherical shape, a factor has to be introduced, which relates the properties of the non-spherical particle to that of a volume equivalent sphere. The shape factor is defined as the ratio of the restistance force of the non-spherical particle to the restistance force of the sphere having the same volume and settling velocity. Definitions of properties of atmospheric particles in this section are taken from Hinds (1999).

2.3. Light scattering by atmospheric particles

This Section introduces some basic concepts to describe the interaction of atmospheric particles with solar radiation. The process of elastic[1] light scattering can be seperated into three regimes: the Rayleigh- and Mie-scattering and the geometric optics. The three regimes may be characterised by the size parameter

$$x = \frac{\pi D_p}{\lambda} \tag{2.6}$$

of a spherical particle being illuminated by light with a wavelength λ. For $x \ll 1$, which is the case for very small scatterers on molecular scale, the interaction of light may be described by Rayleigh-scattering. In cases where $x \gg 1$, light incident on a particle can be subdivided in a large number of rays. At the boundary of the particle, each ray conforms to the rules of geometric optics, so that parts of light are transmitted and reflected at the interface between both media. In the case of fine particles, x is in the same size range as the wavelength of the incoming light. For these particles, Mie theory has to be applied, which will be briefly introduced in the next section. In general, the theory of elastic scattering may predict the scattered field of electromagnetic radiation having the same wavelength as the incident radiation. An additional

[1] no wavelength change between incident and scattered radiation

process that occurs during the interaction of light with a particle is the process of inelastic scattering. This means that some of the energy is retained in the scattering system, leading to an emission of light of a different wavelength. This process will be described in Section 2.3.2.

2.3.1. Elastic light scattering

Important aspects of the theory of elastic light scattering are presented in this Section following mainly the book of Bohren and Huffman (1983). An incoming electromagnetic wave on a particle leads to oscillatory movements of electric charges and thereby a reradiation in all spatial directions. This process is called light scattering. Some energy may be transformed to e.g thermal energy, which is called absorption. Following the publication of Mie (1908), an exact treatment of the problem of scattering of light by a homogeneous sphere in a non-absorbing medium is given in Bohren and Huffman (1983). Starting with Maxwells equations for the propagation of electromagnetic waves, the electric and magnetic fields in- and outside of a particle may be calculated. The scattering and extinction of a particle is described by the cross sections

$$\begin{aligned} C_{sca} &= \frac{2\pi}{k^2}\sum_{n=1}^{\infty}(2n+1)(\left|a_n\right|^2+\left|b_n\right|^2) \\ C_{ext} &= \frac{2\pi}{k^2}\sum_{n=1}^{\infty}(2n+1)Re\{a_n+b_n\}, \end{aligned} \tag{2.7}$$

which are calculated using the expansion coefficients for the scattered field a_n and b_n and the wavenumber k of the incoming radiation. The expansion coefficients depend on the size parameter as given in Equation 2.6 and the complex refractive index of the scattering material. The refractive index is a property of the medium in which electromagnetic waves propagate and describes its scattering and absorption behaviour by the real and imaginary part, respectively. The angle dependence of scattering of a spherical particle is also a solution of Mie theory. In the Rayleigh regime, depolarized light is scattered symmetrically in forward (0 °) and backward (180 °) direction with a minimum at a scattering angle of 90 °. As x increases, the angular scattered light becomes more and more asymmetric with higher intensities in forward direction. It shows a more complex angular pattern. The angular dependence of the scattered light may be illustrated by the phase function, which is defined as the differential scattering cross section (scattering into a specific direction) normalised by the total scattering cross section. It can be interpreted as the probability that light is scattered into a specific direction. The shape of the phase function may be characterized by the asymmetry parameter, which is negative if backscattering is dominant and positive vice versa.
From the difference between extinction and scattering cross sections, the absorption cross section

$$C_{ap} = C_{ext} - C_{sca}. \tag{2.8}$$

may be obtained. Considering an ensemble of absorbing and non-absorbing particles of different size and chemical composition, coefficients of extinction, scattering and absorption may be calculated. Different chemical compounds are considered by different refractive indices. For known volume fractions of individual compounds, the refractive index of the ensemble can be

derived by applying a mixing rule. The simple volume averaging rule is often used, although it is physically not consistent for small absorbing insoluble carbon particles mixed with other material (Bond and Bergstrom, 2006). The average refractive index is derived from the sum of each volume fraction multiplied by the appropriate refractive index. Another mixing rule is called the effective medium or Maxwell Garnett approximation, which represents the ensemble as small spherical carbon particles randomly distributed in the other material. Another possibility is that the absorbing carbon sphere is surrounded by a shell of uniform thickness in which all other non-absorbing compounds are mixed. This shell core configuration was first applied by Ackerman and Toon (1981). A change in state of mixture of carbon may lead to a significant increase in the light absorption ability (Fuller et al., 1999). Having the refractive index of the ensemble of particles, the extinction, scattering and absorption coefficients can be calculated by integrating the appropriate cross sections over all particles in the size range between D_{p1} and D_{p2}

$$\sigma_{ext;sca;ap} = \int_{D_{p_1}}^{D_{p_2}} C_{ext;sca;ap}(D_p) \frac{dN}{d\log D_p} dD_p. \tag{2.9}$$

The quotient of σ_{sca} and σ_{ext} is a dimensionless number and can take values between 0 and 1. It is a measure of the reflectivity of the aerosol and is called the single scattering albedo (SSA). Taking into account that the absorption coefficient is the difference between extinction and scattering coefficient, it can be derived from the equation

$$\sigma_{ap} = \sigma_{ext}(1 - SSA). \tag{2.10}$$

Another important quantity, describing the absorption behaviour of atmospheric particles is the mass absorption coefficient concerning GC or EC, which can be calculated by

$$\delta_{GC;EC} = \frac{\sigma_{ap}}{m_{GC;EC}}. \tag{2.11}$$

2.3.2. Inelastic light scattering-Raman effect

Light that is incident on a molecule or a crystal lattice may be modified, so that light of another wavelength may result after the interaction. This process is called inelastic scattering, since some of the photon energy may remain in the scattering system as excited vibrations or rotations after the scattering process. In cases when the scattering system is a crystal (e.g. graphite), phonones[2] may be excited. The effect of inelastic scattering was discovered by Sir Chandrasekhara Venkata Raman in the year 1928 and is therefore named Raman effect. He focused sunlight and put 2 filters between the lens and the scattering material. With this measurement setup, no light could be observed behind the sample. When removing one filter from the incident beam and placing it between the sample and the observer, some light was visible. This was the proof that a wavelength change must have been occured in the sample (Raman and Krishnan, 1928).
The Raman effect is illustrated in Figure 2.2. The incoming Photon has the energy $h\omega_i$, where ω_i is the frequency and h is the Planck constant. The molecule is in the energy state E_i. After the scattering process a photon with the energy $h\omega_s$ may be emitted. The energy difference $h(\omega_i$-

[2]Quantized oscillations in a crystal lattice

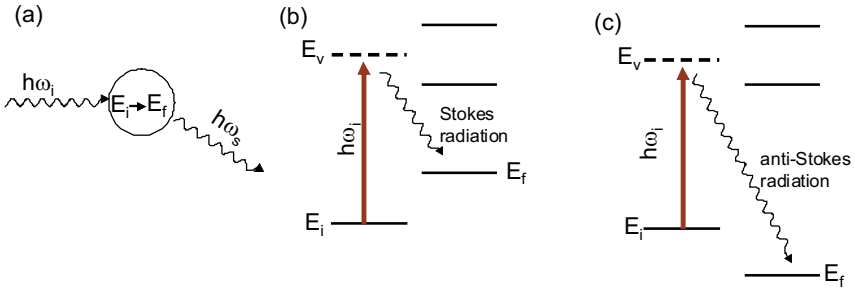

Figure 2.2.: *Illustration of the inelastic photon scattering (Raman scattering) (a), exemplary term diagram for Stokes scattering (b) and anti-Stokes scattering(c) (cf. Demtröder, 1993).*

ω_s) may be converted to rotational or vibrational energy of the molecule (cf. Figure 2.2 (a)). There are two possible processes that may occur in dependence on the initial energy state E_i of the molecule. If it is in a ground state when the photon is impinging, it may be lifted to a virtual energy state E_v. From that state, the photon with energy $h\omega_s$ may be emitted, while leaving the molecule in an excited state E_f. This process is called Stokes Raman scattering (cf. Figure 2.2 (b)). If the incoming photon interacts with a molecule that is already in an excited state, a photon with a higher energy than the incoming photon maybe emitted. This process is called anti Stokes scattering (cf. Figure 2.2 (c)). Both effects may be observed simultaneously, but since more molecules are in an electronic ground state, the intensity of the Stokes radiation is commonly higher. In the Raman spectrum, the intensity is plotted against the frequency shift ω_i-ω_s (cf. Demtröder, 1993).

2.3.3. Raman effect of soot

In a single ideal graphite crystal composed of stacked layers of C-atoms (graphene) in hexagonal arrangement, an incoming laser beam would be inelastically scattered and thereby inducing an in-plane vibrational stretching of the atoms. This Raman active mode has an E_2G symmetry and is located at a wave number of $1580\,\mathrm{cm}^{-1}$ (Tuinstra and Koenig, 1970; Reich and Thomsen, 2004). It is designated as the G-band. In cases when the graphitic lattice contains defects, another band appears in the Raman spectrum. It is attributed to a A_1g mode of small crystals or boundaries of larger crystallites with a Raman shift of $1355\,\mathrm{cm}^{-1}$ (Tuinstra and Koenig, 1970) and is designated as the D-band. The D-band position depends on the excitation energy (Thomsen and Reich, 2000). The width of the D-band can be a proxy for the degree of disorder in the graphite lattice (Cuesta et al., 1994; Ivleva et al., 2007). In addition, it was found by Tuinstra and Koenig (1970) that the intensity ratio of the D and G-band is proportional to the crystallite size. In the Raman spectrum of graphite, a shoulder at the high energy site of the G-band can often be observed. It can be attributed to an E_2G mode in bounding graphene layers (Dresselhaus and Dresselhaus, 1981) and is designated as the D_2-band, following Sadezky et al. (2005).

Freshly emitted soot particles are aggregates of spherules containing graphene layers that are often rolled up to onion-like structures and often occur together with other chemical compounds. However, for atmospheric soot particles the band structure is even more complex than previously

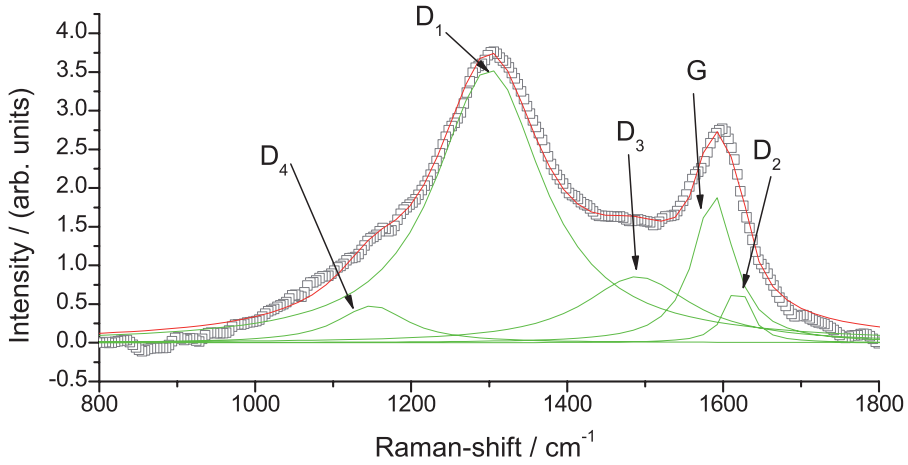

Figure 2.3.: *Raman spectrum of an atmospheric particle sample from a regional observation site. The spectrum is well reproduced by five Lorentzian shaped bands (G, D_1, D_2, D_3, D_4).*

described for ideal graphite crystals. The Raman signal in the wave number region between 800 and 1800 cm^{-1} is almost always a decomposition of 5 overlapping bands (Sadezky et al., 2005), originating from different excitations in the soot structure. An exemplary Raman spectrum of an atmospheric particle sample is shown in Figure 2.3. Two major bands can be seen in the spectrum of the atmospheric sample. The G-band at around 1600 cm^{-1} is shifted to larger wave numbers, which is an effect of the D_2-band. The presence of D_2 in atmospheric soot particles gives evidence that there are many small graphitic domains, i.e. many small graphite crystallites, whose boundaries contribute to this mode. Although the band at 1600 cm^{-1} might be a composition of the G and the D_2 band, it will be designated as the G-band in the following. This position of the major band was also observed in other studies measuring the Raman spectrum of atmospheric particle samples (Dippel and Heintzenberg, 1999; Ivleva et al., 2007). The second and broader signal is located at around 1300 cm^{-1} and is dominated by the D-band. To be consistent with Sadezky et al. (2005), it will be designated as D_1-band. The shift to this wavenumber may be explained by the excitation wavelength dependence of this mode. Following Thomsen and Reich (2000), the D_1-band position for an excitation wavelength of 1064 nm is at 1280 cm^{-1}. A shoulder on the lower energy side of the D_1-band can be seen in Figure 2.3. This mode can be attributed to stretching vibrations in polyene-like structures (Dippel et al., 1999) and is designated as D_4 (Sadezky et al., 2005). The high intensity between the G and D_1 mode was suggested to be caused by an amorphous carbon fraction (organic molecules, fragments and functional groups) and is designated as the D_3 band (Sadezky et al., 2005). Since the graphite signals in the Raman spectra of atmospheric particle samples are obvious, the carbonaceous species detected by Raman-spectroscopy is designated as graphitic carbon (GC).

2.4. Radiative forcing

The spectral distribution of solar radiation that enters the atmosphere has a maximum at wavelengths around 0.45 and 0.5 μm and follows Plank's law for blackbody radiation at 5777 K. This shortwave radiation is absorbed by ozone in the ultraviolet spectral region. In the near

infrared spectral region, absorption by greenhouse gases (e.g. CO_2) and water vapour are important. In the visible spectral region, scattering and absorption by aerosols and clouds are substantial processes. The earth surface is also an important absorber of solar radiation. Around 70% of the incoming light are absorbed by the atmosphere and the earth's surface.
The radiant flux density (F) is defined as the radiant energy across a surface element and has the unit of $\mathrm{W\,m^{-2}}$. It is called irradiance, when it is received on a surface. Here, the upward flux is denoted with F^+ and the downward flux with F^-. The shortwave radiation absorbed at the surface is transformed to terrestrial longwave radiation, which is emitted back into the atmosphere. In principle, the net radiation may be expressed in terms of upward and downward longwave (subscript l) and shortwave (subscript s) radiant fluxes as

$$F^* = F_s^- - F_s^+ + F_l^- - F_l^+. \tag{2.12}$$

The net radiation at the surface is balanced by fluxes of sensible, latent and ground heat. Calculating net radiation at the top of the atmosphere (TOA), F_l^- may be set to 0, since no longwave radiation enters the atmosphere. In addition, F_s^- is the solar constant, which is not really a constant, since it depends on the solar zenith angle and the eccentricity of the earth's orbit around the sun. Following the IPCC definition, the radiative forcing of the surface-troposphere system is the change in net (down minus up) irradiance (solar plus long-wave; in $\mathrm{W\,m^2}$) at the tropopause due to the perturbation in or the introduction of a forcing agent (e.g. CO_2). Stratospheric temperatures are allowed to readjust to radiative equilibrium, but with surface and tropospheric temperatures and state held fixed at the unperturbed values (Forster et al., 2007). This definition is usually applied for estimating the globally and annually averaged radiative forcing for gases and aerosol particles. For aerosol particles the instantaneous radiative forcing at top of the atmosphere is often calcultated, since stratospheric adjustment to radiative equilibrium is likely to be small (Haywood and Shine, 1997). The instantaneous aerosol radiative forcing ΔF can be calculated at the surface by

$$\Delta F = F_{aer}^* - F_0^*, \tag{2.13}$$

which is the difference of the net irradiance for the cases that aerosol particles have a feedback (aer) or no feedback (0) on radiation. At TOA, Equation 2.13 reduces to

$$\Delta F = (F_s^+ + F_l^+)_0 - (F_s^+ + F_l^+)_{aer}, \tag{2.14}$$

since downward shortwave radiation is the same for both cases and no longwave radiation enters the atmosphere. The net radiative forcing in the atmosphere may be calculated from the difference of the net radiative forcing at TOA and at the surface.
For the calculation of the radiant fluxes at the surface, it is important to know what happens with the radiation as it passes through the atmosphere. Imagine a small volume element containing aerosol particles and gases. Radiant energy passing through this element along a path may be lost due to absorption and scattering. It is also possible, that some radiant flux is gained, because of scattering from other directions or thermal emission of the medium itself. The conservation of energy leads to the general equation of radiative transfer, that describes the

change in radiance along a path of propagation in a medium due to scattering, absorption and thermal emission.

In many regional models it is sought to derive F^+ and F^- in different levels of the model atmosphere in terms of integrated values over all directions of incidence of solar radiation. For this purpose, so called two-stream approximations are often used. It is common to substitute the radiance[3] in the equation of radiative transfer by a linear function containing the cosine of the scattering angle, which is called the Eddington method. The phase function, which describes the scattering direction of light by particles in the atmosphere is also approximated. For isotropic scattering, it can be set to one, which is the simplest but not realistic case. The phase function may also be approximated by a second order Legendre polynomial containing the cosine of the scattering angle and the asymmetry factor. Applying these approximations to the radiative transfer equation leads to a system of linear differential equations for the change of F^+ and F^- with a changing optical thickness of the medium. This rough description of the complicated topic of atmospheric radiative transfer and possible solution methods is described in more detail in several books (e.g. Thomas and Stamnes, 2002; Lenoble, 1993; Liou, 2002).

[3] energy flux in a solid angle and across a surface perpendicular to the direction of incidence

3. Methods

3.1. Experimental data collection

3.1.1. The German Ultrafine Aerosol Network (GUAN)

In the present study, the data from 10 observation sites of the GUAN[1] network is used. This still growing network arose from an environmental research project aimed on the characterization of chemical and physical properties of ultrafine aerosol particles (Birmili et al., 2009). It offers the opportunity to measure ambient aerosol concentartions in environments as diverse as street canyons, urban residential areas, regional background and mountain sites, using state-of-the-art measurement devices. All instruments will be described in detail in Section 3.2. All measurement sites of GUAN used in the present study are summarized in Table 3.1 and Figure 3.1.

3.1.2. GUAN measurement sites

Measurement sites at mountain locations are situated in the Alps, the black forest and in the prealpine lands. The highest mountain, the Zugspitze, has a altitude of 2650 m. It is operated by the Federal Envrionmental Agency (Umweltbundesamt, UBA) and by the German Meteorological Service (Deutscher Wetterdienst, DWD). Due to its altitude, nearly free tropospheric conditions may be observed especially in the winter months. In the summer months, this location is often influenced by conditions associated by the planetary boundary layer, due to extended vertical mixing. The other mountain sites Hohenpeißenberg and Schauinsland are at a height of 988 m and 1210 m. They are operated by the DWD and UBA, respectively.
The regional site in Bösel is part of the air quality monitoring system of Lower Saxony (Staatliches Gewerbeaufsichtsamt, Hildesheim). It lies to the south of a village and is mostly surrounded by large agricultural areas, but maybe also influenced by the local industry. Nearly free of such effects is the regional measurement site in Waldhof, which is operated by the UBA. A third regional observation site is Melpitz, which is operated by the institute for tropospheric research (IfT). It is located to east of Leipzig and is surrounded by large areas of grassland. It is equipped with numerous physical and chemical measurement devices.
The measurement site at the IfT can be classified as an urban station, since it is located a few kilometer to the east of the city center, approximately 100 m from the next main road. The inlet is at a height of 16 m on the roof of the main building of the IfT, so that urban background conditions are measured. Another urban site is in Augsburg, which is located in the southern part of Germany and is operated by the Helmholtz Zentrum München.
The traffic site Leipzig-Eisenbahnstraße is situated in a street canyon, which is characterized

[1] http://wiki.tropos.de/GUAN

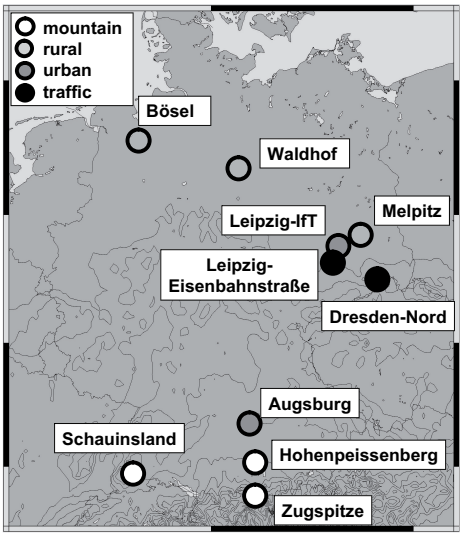

Figure 3.1.: *Geographical position of the measurement sites of the German Ultrafine Aerosol Network (GUAN).*

by buildings being 20 m apart and about 23 m high. It is located near the city center, but also not far away from the IfT. The traffic situation shows a clear diurnal cycle with around 20000 vehicles per working day (Rose et al., 2006). A second traffic dominated measurement site is located in Dresden. This site is part of the air quality monitoring network of Saxony (LFULG). The geographical location of each measurement site is given in Figure 3.1.

3.1.3. Overview of instrumentation in GUAN

Atmospheric particles are sampled by using either PM_{10} or whole air inlets. At most measurement sites, a cyclone (model SCC2.229, BGI, Waltham, USA) is applied to separate the PM_1 fraction, since only fine and ultrafine particles should be characterized. The aerosol is dried before the measurement using Nafion dryer.
The measurement sites of GUAN are equipped with Multi Angle Absorption Photometers (MAAP), which measure the BC mass concentration. It can be converted to the absorption coefficient at 637 nm by applying the mass absorption coefficient of $6.6\,m^2\,g^{-1}$ as will be described in Section 3.2.1. At Augsburg, the BC concentration is measured by an Aethalometer (Type 8100, Thermo Fisher Scientific Inc.). This was compared to the MAAP and a correction function was found by Birmili et al. (2010), so that the Aetholemeter output could be adjusted to the MAAP output. The aerosol number size distributions are measured using either scanning mobility particle sizers (SMPS) or twin differential mobility particle sizers (TDMPS), which will be described in more detail in Section 3.2.2. Discontinuous measurements of the chemical composition are performed by sampling particles with Berner impactors for subsequent analysis. The graphitic carbon (GC) content is measured for selected episodes using the new Raman method, which will be described in detail in Section 4.1. Details of the deployment of the measurement systems are given in Table 3.1.

Observation site	Location	Altitude	Operator	Type	Continuous measurements	Discontinuous measurements
Leipzig-Eisenbahnstraße	51.34° N, 12.37° E	90 m	IfT Leipzig	traffic	TDMPS[1]+TD[2], MAAP[3]	Berner-5[4], Raman[5]
Dresden-Nord	51.05° N, 13.74° E	115 m	LFULG Dresden	traffic	TDMPS[1], MAAP[3]	
Leipzig-IfT	51.34° N, 12.37° E	90 m	IfT-Leipzig	urban	TDMPS[1]+TD[2], MAAP[3]	Berner-5[4], Raman[5]
Augsburg	48.36° N, 10.91° E	484 m	HMGU	urban	TDMPS[1]+TD[2], Aethalometer[6]	Berner-5[4], Raman[5]
Bösel	53.00° N, 7.97° E	13 m	GAA Hildesheim	regional	SMPS[7]+TD[2], MAAP[3]	Berner-5[4], Raman[5]
Melpitz	51.54° N, 12.93° E	86 m	IfT-Leipzig	regional	TDMPS[1]+TD[2], MAAP[3]	Berner-5[4], Berner-10[4], Raman[5]
Waldhof	52.80° N, 10.76° E	55 m	UBA	regional	SMPS[7], MAAP[3]	
Hohenpeißenberg	47.80° N, 11.00° E	988 m	DWD	mountain	SMPS[7]+TD[2], MAAP[3]	Berner-5[4], Raman[5]
Schauinsland	47.91° N, 7.91° E	1210 m	UBA	mountain	SMPS[7]+TD[2], MAAP[3]	Berner-5[4], Raman[5]
Zugspitze	47.91° N, 7.91° E	2650 m	UBA and DWD	alpine mountain	SMPS[7]+TD[2], MAAP[3]	Raman[5]

[1] TDMPS (Twin Differential Mobility Particle Sizer), number size distribution between 3 and 800 nm
[2] TD (Thermodenuder), evaporates volatile compounds at 300 °C
[3] MAAP (Multi Angle Absorption Photometer), absorption coefficient at a wavelength of 637 nm
[4] Berner-5/10 (5/10-stage Berner impactor), particle sampling in 5/10 aerdynamic diameter classes between 0.05 and 10 μm for chemical analysis
[5] Raman (Raman spectrometer), mass concentration of graphitic carbon
[6] Aethalometer, mass concentration of black carbon
[7] SMPS (Scanning Mobility Particle Sizer), number size distribution between 10 and 800 nm

Table 3.1.: *Summary of measurement sites and deployed measurement systems in the German Ultrafine Aerosol Network (GUAN).*

3.2. Experimental techniques

3.2.1. Multi angle absorption photometer

The aerosol absorption coefficient can most accurately be determined by using a combination of extinction and scattering measurement. A more feasible approach is the photometry, where particles are collected on a filter and transmission of light through the loaded medium is measured. Such methods are calibrated by using extinction and scattering difference as an absorption coefficient reference (e.g. Bond et al., 1999; Virkkula et al., 2005). Problems associated with photometric methods are mainly due to the measurement of light attenuation caused by a combination of scattering and absorbing particles deposited on a scattering filter matrix. This has to be accounted for by applying several corrections on the photometer output.
An approach avoiding problems associated with particle scattering is the polar photometry. Moveable detectors are used to measure the scattered field of a particle laden filter medium (Kopp et al., 1999). A more suitable device for continuous measurements of the aerosol absorption coefficient is the MAAP. The version of the MAAP applied in the present study (type 5012, Thermo Scientific Inc.) is described in detail in Petzold et al. (2005). It measures light at a wavelength of 637 nm transmitted and scattered back from a particle laden glass microfiber filter medium (GF10, Whatman, Maidstone, Kent). The intensity of the transmitted light follows the

Lambertian cosine law for diffuse radiation, which means that it is proportional to the cosine of the scattering angle. It can therefore be measured using only one detector. In backward direction the scattered intensity depends on the aerosol composition and is a combination of diffusely and direct scattered radiation. Petzold and Schönlinner (2004) showed that it can be represented by a linear combination of a Lambertian cosine law and a Gaussian type distribution. They found that 2 well positioned detectors are enough to derive the fraction of diffusely scattered radiation. If particles are deposited on the glass microfiber filter, they only penetrate into the uppermost layer of the medium. The combination of filter matrix and particles can therefore be seen as a 2 layer system. To derive the absorption coefficient of the deposited particles, the radiative transfer through this 2 layer system is calculated following the method described in Petzold and Schönlinner (2004). From this method, the aerosol layer (embedded in filter matrix) single scattering albedo and optical thickness are derived by iteration. Using in addition the spot diameter and the volume of air drawn through the medium, the aerosol absorption coefficient can be derived, since only particles and not filter fibers are responsible for absorption. The direct output of the MAAP is m_{BC}, which is derived by dividing the absorption coefficient by a mass absorption coefficient of $6.6\,\mathrm{m^2\,g^{-1}}$.
Inside the MAAP, a filter-spot is loaded until a certain transmission is reached, which was set to 50 %. In addition, the MAAP was programmed so that a filter change was initiated every day at 00:00, in order to have daily samples for later analysis. The flow rates were adjusted to match the cut off flow rates of individual inlets at individual observation sites and were mostly between 6 and $16\,\mathrm{l\,min^{-1}}$. The temporal resolution was set to 1 min. In an experiment, 5 MAAP devices were compared for urban aerosol at Leipzig-IfT. Therefore, different flow-rate combinations were used. It was found that the variability between the MAAP was lowest (3%) for highest flow rates ($14\ \mathrm{l\,min^{-1}}$) and for the 10 min averaged absorption coefficient. For lowest flow-rates ($6\,\mathrm{l\,min^{-1}}$), the variability increased to 5 %. Adjusting all MAAP devices to different flow rates between 6 and $16\,\mathrm{l\,min^{-1}}$ as it is the case in the present study, a variability of around 8 % was found. In addition, the absorbing fraction of atmospheric aerosols was evaluated by a comparison of PM_1 and PM_{10} absorption coefficients at a regional and a traffic site. This was done, because no homogeneous cut off diameter at all measurement sites of GUAN could be realised. It was found, that PM_1 fraction is responsible for 90 % of absorption at regional and for 95 % at traffic sites. Correlation coefficients were around 0.98 and indicate a homogeneous ratio of PM_1 and PM_{10} absorption.

3.2.2. Mobility particle size spectrometer

To measure the particle number size distribution, TDMPS and SMPS systems are applied. These systems classify particles according to their mobility. This mobility can be transferred to a volume equivalent sphere diameter. A TDMPS system measures the particle number size distribution between mobility diameters of 3 and 800 nm. It consits of 2 differential mobility analyzers (DMA), which are sensitive to different size classes. In the first size class, particles between 20 and 800 nm are measured using a longer DMA in combination with a condensation particle counter (CPC 3010, TSI St. Paul (MN), USA). Smaller particles between 3 and 20 nm are detected using a short version of the DMA (UDMA) and a UCPC 3025 ((TSI St. Paul

(MN), USA) (Birmili et al., 1999). At most observation sites, only a SMPS is applied, which measures the particle number size distribution between 10 and 800 nm by using only 1 DMA and CPC. The temporal resolution of the size spectrometers was 10 min.
The TDMPS and SMPS systems were partly coupled with a thermodenuder, upstream of these size spectrometers. In this case, the size distributions with and without thermodenuder were measured in an alternating fashion. In a thermodenuder, volatile compounds are evaporated by thermal desorption. In the configuration described by Wehner et al. (2002) it is composed of a heating and a cooling unit. In the heating section, the aerosol is heated up to 300 °C . The cooling section is filled with activated carbon, which adsorbs evaporated gas phase compounds. Particle losses inside this device may occur due to thermophoretic and diffusional processes. Such a conditioning unit may be applied on the whole size distribution to get the total non-volatile particle fraction. If particles of a certain diameter are selected upstream of the thermodenuder, the mixing state of non-volatile particles may be measured. Such a device is called a volatile tandem DMA (VTDMA) and is used to study the external and internal mixed fraction of atmospheric soot particles (Rose et al., 2006). To explore the composition of the total non-volatile volume in regional locations, Engler et al. (2007) combined volatilization temperatures, chemical composition and thermodenuder-TDMPS measurements. The results suggest, that the non-volatile volume consists of EC, inorganic salts of Na, Ca, K, Mg and some organic compounds.

3.2.3. Thermographic EC/OC analysis

The following description of the thermographic method applied on Berner impactor samples is taken from Nordmann et al. (2009). In a Berner impactor, particles are deposited on aluminium foils in different stages. These stages are defined by an upper and lower aerodynamic diameter, depending on the cut off in the individual stages. Particulate carbon was characterized by a thermographic method similar to guideline VDI (1999) using a carbon analyzer (Ströhlein, C-mat 5500). In a first step, an aliquot from the Berner impactor aluminium foils was heated for eight minutes to 650 °C in a nitrogen atmosphere. Carbon compounds that evaporate under these conditions are referred to as organic carbon (OC). Evaporated OC is oxidised quantitatively on a CuO-catalyst at 850 °C to CO_2 and measured using an NDIR detector. In a second step, the remaining elemental carbon (EC) was determined by heating the sample under oxygen atmosphere at 650 °C for eight minutes, oxidising all carbon to CO_2, the latter being detected by infrared absorption. Foil blank values were subtracted from the results. As aluminium foils melt at 659°C, the operational temperature cannot be further elevated. Carbonates, notably, do not decompose at this temperature (Petzold and Nießner, 1996). Calibration of the instrument was performed with potassium hydrogen phthalate as an external standard. Typical measurement uncertainties of 5.5 % for OC and 8.9 % for EC were determined for mass concentration typical for atmospheric conditions (Neusüss et al., 2000). Numerous experimental procedures to distinguish OC and EC have been described (Penner and Novakov, 1996). Comparisons between various methods, including the one used in this study, during INTERCOMP2000 showed reasonable comparability for total carbon (TC), but considerable deviations for OC and EC between the participants (Schmid et al., 2001). It was concluded that the VDI (1999) method and its

variations without optical charring correction[2] may underestimate OC and, in turn, overestimate EC (ten Brink et al., 2004).

3.3. Raman spectroscopy

3.3.1. Raman spectrometer

To measure the Raman-spectrum of atmospheric particles, a near infrared-Fourier transform (NIR-FT) Spectrometer coupled with a Raman-Module FRA-106 (Bruker Daltonik, Bremen, Germany) was applied. The monochromatic light source is a ND: YAG Laser with a wavelength of 1064 nm. The sample to be measured is illuminated over mirror arrangement so that incoming and Raman scattered light do not influence. The fraction of light that is directly reflected and the Rayleigh scattered light are removed by a filter module, since their intensities are much larger than the light from Raman scattering. To measure the Raman scattered light at different wavelengths, an interferometer is applied. In the interferometer, the light that is scattered from a sample is passed through a beam splitter, which redirects one part to a fixed and the other part to a moveable mirror. After reflection, both light beams interfere, and the resulting wavelength is proportional to the mirror shift. From the interferometer, the light is passed to a Ge-Diode detector, which has to be cooled with liquid nitrogen to achieve highest sensitivity. Fourier transformation is used to convert the Raman scattered intensity from a function of the mirror shift to a function of wavenumber. This wavenumber is the so called Raman-shift. Details of the measurement setup can be seen in Bruker (1994) and Bruker (1995).
For the measurements in the present study, the laser power was adjusted to 530 mW and the spectral resolution was set to $8\,\mathrm{cm}^{-1}$. The samples were iluminated with a defocused beam in order to avoid a strong heating of the samples and to measure the average spectrum of circular area with a diameter of approximately 1 mm. This area is representativ for the whole spot, since it was loaded homogeneously. The wavelength calibration was performed before the measurement. Therefore, the characteristic band of a Nylon sample was used. All spectra were recorded as averages of 2900 to 3000 single measurements.

3.3.2. Evaluation of Raman-spectra

The raw spectra, recorded by the Raman spectrometer, have to be modified in order to remove signals stemming from background effects such as fluorescence and heating so that the undisturbed GC signals are remaining. The evaluation procedure is illustrated in Figure 3.2. The spectra of a loaded and an unloaded filter differ in the GC signal that is only visible in the spectrum of the loaded filter and in the less pronounced filter signals due to the particle loading (Figure 3.2 (a)). As described before, the filter band between 1453 and $1530\,\mathrm{cm}^{-1}$ was chosen for normalization of all spectra. Therefore, a vector normalization calculating the normalized values by

$$y_{norm_i} = \frac{y_i - \frac{1}{n_2-n_1}\sum_{j=n_1}^{n_2} y_j}{\sqrt{\sum_{j=n_1}^{n_2}(y_j - \frac{1}{n_2-n_1}\sum_{k=n_1}^{n_2} y_k)^2}} \tag{3.1}$$

[2]Method to account for the pyrolysis of OC to EC in the nitrogen atmosphere (Johnson et al., 1981)

is used (Bruker, 1999). Equation 3.1 is valid for a spectrum given by the intensities (y) at discrete Raman-shifts (index i). The integers n_1 and n_2 are the indices corresponding to Raman-shifts of 1453 and 1530 cm^{-1} . After this step, the spectra of the loaded and unloaded filter coincide in the wavenumber region between 1453 and 1530 cm^{-1} (Figure 3.2 (b)). In the following step, the filter signal is removed by subtracting the spectrum of the unloaded filter from the spectrum of the loaded filter (Figure 3.2 (c)). On the resulting spectrum, a baseline correction between 1110 and 1790 cm^{-1} is applied (Figure 3.2 (d)) and afterwards the G-band is integrated in the bounds between 1510 and 1736 cm^{-1} . Because of the large number of samples analyzed in this study, the described steps were automated.

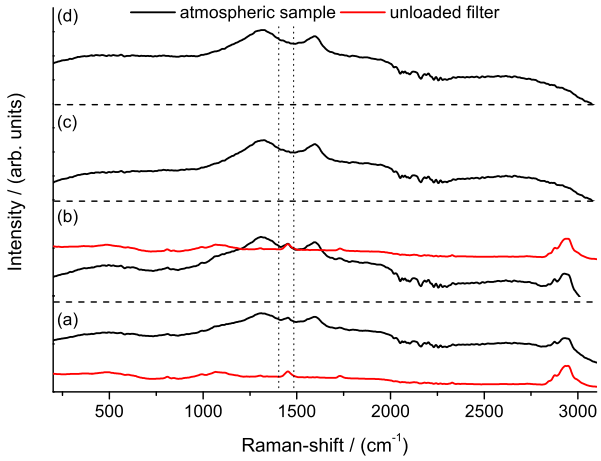

Figure 3.2.: *Evaluation of measured Raman-spectra with raw spectra of a loaded and an unloaded filter (a), normalized to the marked wavenumber region (b), eliminated filter signal (c) and baseline corrected spectrum (d).*

3.3.3. Calibration experiment

The main goal of the calibration experiment is to find the relationship between gravimetric measured masses of Printex®90 and the integral of the G-band in the Raman-spectrum of the same particles. The experimental setup is shown in Figure 3.3. For the generation of soot aerosols, a hydrosol of distilled water and Printex®90 was generated and nebulized. These aerosols were passed through a silica gel drier and a bipolar diffusion charger before they were led into the mixing chamber. The concentration could be regulated with the nebulizer and checked with the MAAP. With filter holders, polycarbonat (Nuclepore™, Whatman, Maidstone, Kent) filters with a pore size of 100 nm, glass microfiber (GF10, Whatman, Maidstone, Kent) and quartz fiber (Pallflex®, Pall, New York, USA, not shown in Figure 3.3) filter substrate were simultaneously loaded leaving flow rates constant by using mass flow controllers. The glass microfiber filter is the medium, which is used inside the MAAP. It should be measured by Raman-spectroscopy after loading. For the gravimetric mass determination, polycarbonat and quartz fiber filters were used. In contrast to the quartz fiber filters, polycarbonat filters have a low hygroscopicity. However, they can be electrostatic charged while they are loaded. The unloaded filters were first conditioned to a relative humidity of around 40% and a temperature of

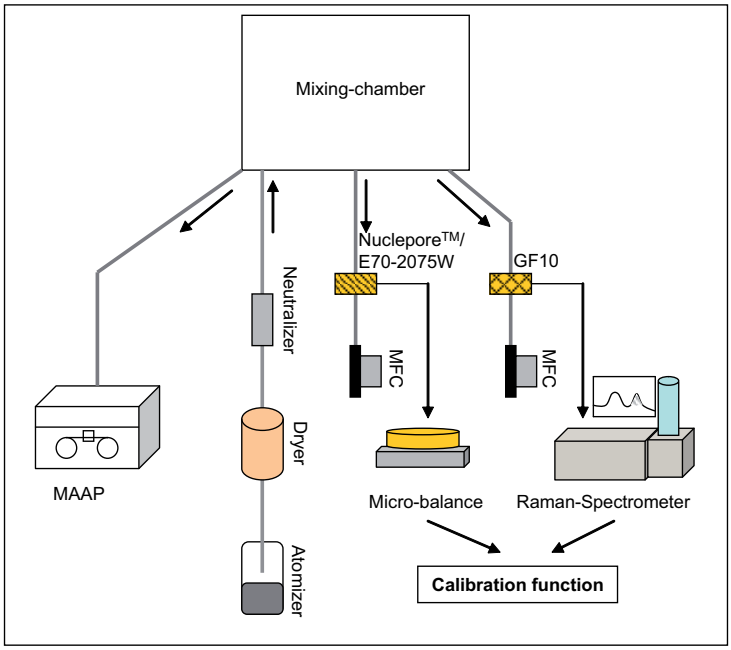

Figure 3.3.: *Experimental setup of the calibration experiment (MFC, mass flow controller).*

around 20 °C in the weighing chamber for several days. Subsequently, they were weighed using a micro balance (UMT, Mettler Toledo) to determine the blank value. The polycarbonat filters had a blank mass of around 10 mg with a standard deviation of 1 μg. The quartz fiber filters had a blank mass of 50 mg with a standard deviation of 3 μg. After loading, the filters were again conditioned in the weighing chamber and the Printex®90 mass was subsequently derived from the difference between the blank and the loaded masses of each filter. Every filter was weighed at least 10 times to derive an uncertainty. By using the flow ratio between the glass microfiber filters and the polycarbonat filters, the gravimetric mass was converted to the mass on the microfiber filters that were not weighed. These microfiber filters were then measured with the Raman-spectrometer and the resulting spectrum was evaluated as described in Section 3.3.2. To avoid background effects during the Raman measurement, the flow ratio was adjusted so that the mass on the glass microfiber filters is comparably low in contrast to the corresponding poycarbonat filters for the weighing procedure.

3.4. Microphysical-optical model to derive the soot mixing state

An important property of atmospheric soot particles is their state of mixture with other substances. It is hard to assess, since only a few instruments exist, which are able to measure the mixing state directly. Ma et al. (2012) developed an algorithm, which enables an indirect estimation of the fraction of external mixed soot particles based on measurements of the particle number size distribution, information about mass size distribution of elemental carbon, absorption coefficient and hemispheric backscattering fraction. They applied a shell-core model (Bohren and Huffman, 1983) to simulate the backscattering fraction at three different wavelengths based on the measured microphysical properties. The fraction of external mixed soot particles was varied until the deviation between measured and modeled backscattering fractions

was minimal. Another approach deriving the external mixed soot fraction by minimizing the deviation between model and measurement was introduced by Cheng et al. (2006). They minimized the difference between modeled and measured absorption, scattering and backscattering coefficients by using a volume averaging method and the Mie code for spherical particles (Bohren and Huffman, 1983) without any shell.

According to Ma et al. (2012), the particle volume size distribution, which is the third moment of the number size distribution (Equation 2.2) divided by the particle density, can be expressed as

$$\frac{dV}{d\log D_p} = \frac{dV_{ext,s}}{d\log D_p} + \frac{dV_{int,s}}{d\log D_p} + \frac{dV_{int,ns}}{d\log D_p} \tag{3.2}$$

with $\frac{dV_{ext,s}}{d\log D_p}$ is the externally mixed soot volume size distribution, $\frac{dV_{int,s}}{d\log D_p}$ is the internally mixed soot volume size distribution and $\frac{dV_{int,ns}}{d\log D_p}$ is the non-soot volume size distribution. Assuming further that external mixed soot particles are evenly distributed over the entire size distribution, one can introduce ϵ with

$$\epsilon = \frac{\int \frac{dV_{ext,s}}{d\log D_p}\, dD_p}{\int \frac{dV_s}{d\log D_p}\, dD_p} \tag{3.3}$$

as the externally mixed soot fraction and $\frac{dV_s}{d\log D_p}$ is the soot volume distribution. The external mixed soot fraction can take values between 0 and 1. Here, 0 means that all soot particles are internally mixed and 1 means that no particle is mixed with another substance in a shell-core configuration. When applying a shell-core Mie model to derive optical properties, the diameter of the core D_{core} as a function of particle size, as well as their number concentration must be known. Using ϵ, the core diameter can be calculated by

$$D_{core}(D_p) = \sqrt[3]{\frac{6}{\pi} \cdot \frac{(1-\epsilon) \cdot \frac{dV_s}{d\log D_p}}{\frac{dN}{d\log D_p} - \epsilon \cdot \frac{dN_s}{d\log D_p}}} \tag{3.4}$$

with $\frac{dN_s}{d\log D_p}$ is the particle number concentration of soot particles.

In this study, the shift in the particle number size distribution when removing volatile compounds was measured with a thermodenuder (cf. Sect. 3.2.2) for $T = 300\,^{\circ}\mathrm{C}$. This size distribution shows a high correlation with the aerosol absorption coefficient, as will be shown later in Section 4.2.3, and is therefore associated with $\frac{dV_s}{d\log D_p}$. To derive this distribution, the mass concentration of GC from Raman-spectroscopy is converted to a volume concentration by using a particle density of $1.8\,\mathrm{g\,cm^{-3}}$ (Park et al., 2004b). From the quotient of the GC volume concentration and the integrated thermodenuder volume size distribution, a factor is derived that is applied on each bin of the volume size distribution after the thermodenuder to derive $\frac{dV_s}{d\log D_p}$. This method implies the assumption that the real soot particle volume size distribution has a similar shape as the volume size distribution after the thermodenuder.

Based on this information about size distributions, the absorption coefficient at 637 nm can be calculated by a shell-core Mie model and subsequently compared to the measured values. Varying input variables to the model, the deviation between measurement and model can be minimized. Following the approaches mentioned in the beginning of this section, the deviation is minimized by varying ϵ using a χ^2 minimization method (cf. Appendix A). The uncertainty

of ϵ is estimated via a Monte-Carlo method, varying the other input parameters in the limits given by their individual uncertainties.
The density of soot was taken to be $1.8\,\mathrm{g\,cm^{-3}}$ Park et al. (2004b) with an uncertainty of 17 %. The refractive index was taken to be $1.85 + 0.71\,i$ as the average of values summarized in Bond and Bergstrom (2006) for the void fraction. The uncertainty was 5 % for the real part and 11 % for the imaginary part, as given from the range of values in Bond and Bergstrom (2006). Since changes in the refractive index of the non-absorbing aerosol components are small, the refractive index was chosen according to Wex et al. (2002); Cheng et al. (2006); Ma et al. (2012) as $1.55 + 10^{-7}\,i$ with an uncertainty of the real part of 1.5 %. The absolute uncertainty of the particle number concentrations with and without thermodenuder were taken to be 20 %, according to values given in Wiedensohler et al. (2012). The error in absorption coefficient was taken from Petzold and Schönlinner (2004) to be 12 %.
The procedure starts with calculating all relevant input parameters to the model, using random numbers to vary them in the limits of their uncertainties as presented before. In the next step, core diameters are calculated using Equation 3.4 with an initial guess of ϵ. Afterwards, the absorption coefficient is calculated by using absorption cross sections calculated by Mie subroutines for spherical and coated spherical particles provided in Bohren and Huffman (1983).The absorption coeffcient is calculated using the discretized form of Equation 2.9 for size dependent absorption cross sections of a combination of coated and uncoated particles. Calculated absorption coefficients are then compared to the measured values in terms of χ^2. For each set of input parameters, the best value of ϵ can then be found by applying the algorithm in Appendix A by repeating the optical calculations with modified values of ϵ in each iteration step. In sum, 800 iterations with modified input parameters were performed for each time step, resulting in an average ϵ and an uncertainty in terms of its standard deviation.

3.5. WRF-Chem model

3.5.1. General description

The Weather Research and Forecast model (WRF) is a massive parallelized state-of-the-art numerical model designed for research. It is suitable for a broad spectrum of applications in simulating atmospheric phenomena of horizontal extents ranging from meters to thousands of kilometers. WRF is applicable on a variety of computing platforms for operational numerical weather forecast, parameterized physics research and air quality modeling using the WRF-Chem package (Grell et al., 2005).
In WRF, the compressible and non-hydrostatic Euler equations can be integrated with 2 dynamical solvers: ARW (Advanced Research WRF), which was developed at NCAR (National Center of Atmospheric Research, Boulder, Colorado, USA) and NMM (Non-hydrostatic Mesoscale Model) which was developed at NCEP (National Center for Environmental Prediction, Camp Springs, Maryland, USA). The prognostic variables are the u,v and w wind directions, the perturbation potential temperature, the perturbation geopotential, perturbation surface pressure and several other optional scalars. All equations are transformed to the terrain following hydrostatic pressure as the vertical coordinate and are horizontally discretized on an arakawa c-grid,

which means that velocities are staggered about a half grid length to thermodynamic variables. WRF offers the opportunity to insert higher resolution domains into a coarser grid, a procedure that is called nesting. The boundary conditions of the inner grid are taken from the coarse grid. There are two possibilities for nesting. The first one is the one-way nesting, which is used if there should be no feedback of the fine grid to the coarse grid. A two-way nesting is applied, if variables simulated for the fine grid should influence variables on the coarse grid. Only a horizontal nesting is implemented. A two-way nesting is applied in the present study.
WRF can account for a variety of microphysical settings, ranging from simple bulk schemes to more sophisticated schemes allowing for mixed phase cloud resolving simulations. Planetary boundary layer physics are suitable for turbulent kinetic energy prediction. The surface may consist of several layers allowing for a vegetation and soil moisture representation. Also snow cover and sea ice maybe included. The longwave and shortwave radiation field can be calculated for a broad spectral region including clouds, gases and aerosol effects (Skamarok et al., 2008).
WRF may be on-line coupled with a chemical transport module (WRF-Chem) treating aerosol particles and gases. On-line coupling means that aerosol particles may for example directly influence the radiative transfer in the atmosphere. Moreover, they may act as cloud condensation nuclei and thereby changing cloud cover and radiative effects of clouds, which is also designated as the indirect effect. Clouds, in turn, may reduce aerosol concentrations by e.g. wet scavenging processes (Chapman et al., 2009).

Aerosol module

For representing aerosol particles in WRF-chem, the MOdel for Simulating Aerosol Interactions and Chemistry (MOSAIC) is used. In this model, aerosol particles are treated sectional. This means that they are represented in a specific number of bins, which are defined by their upper and lower dry diameter so that water uptake or loss may not transfer particles between those bins. With this model, mass and number of particles may be simulated. MOSAIC treats the following chemical species: sulfate, methane sulfonate, nitrate, chloride, carbonate, ammonium, sodium, calcium, black carbon, organic carbon and other inorganic mass such as silica, other minerals and trace metals. All species are assumed to be internally mixed in each bin. A shell-core configuration as described in Section 2.3.1 is also possible. Particle growth and shrinkage may occur by an uptake of trace gases such as sulfuric acid, nitric acid, hydrogen chloride, ammonia and secondary organic species. In addition particle coagulation and the formation of new particles by nucleation of sulfuric acid and water vapor are included (Fast et al., 2006; Zaveri et al., 2008).

Optical Particles Properties and radiative transfer

In WRF-Chem, every chemical constituent is associated with a complex index of refraction. One possible option to determine a refractive index for a MOSAIC bin is using a volume averaging method including aerosol water. Mie theory is then applied to find efficiency factors of extinction and scattering as well as asymmetry factor. To calculate the extinction and scattering coefficients, the size distributions are integrated over all size bins. To accelerate the calculations, the Mie code is called only once in the beginning of the simulation to derive scattering and extinc-

tion cross sections for a broad range of size parameters and a range of refractive indices typical for atmospheric aerosols. Then, the method presented in Ghan et al. (2001) and modified for the sectional approach is applied. Expansion coefficients calculated with this method are used to derive cross sections in each of the following time steps instead of using full Mie-theory. The aerosol optical properties are calculated at 4 wavelengths (0.3, 0.4, 0.6 and 1 μm) and are then passed to the radiative transfer model, which is called the Goddard short-wave scheme (Chou et al., 1998). In this model, aerosol optical properties are accounted for in 11 spectral bands between 0.18 and 10 μm in the ultraviolet, visible and near infrared wavelength region. Since the optical properties are only calculated at 4 wavelengths, interpolation and extrapolation is used to calculate the optical properties at the aerosol influenced spectral bands. The Goddard short-wave scheme also accounts for ultraviolet absorption by ozone and scattering of visible light by gases and clouds. In the infrared spectral region, contributions to absorption come from water vapor, O_2, CO_2 and clouds. The transmission and reflection functions for each atmospheric layer are then calculated and a 2 stream adding method is applied to derive the fluxes in the atmosphere and at the surface (Fast et al., 2006). The changes in atmospheric radiation fluxes due to aerosol particles may have a feedback on the atmospheric physics and the dynamics module in the meteorology simulation.

3.5.2. Model domains and meteorological settings

The model grid was chosen to consist of 2 nested domains. The parent grid has a spatial resolution of 36 km and covers most of Europe as well as parts of Russia and Africa. This corresponds to 125 grid cells in west-east and 86 grid cells in north-south direction. The nested domain has a resolution of 12 km and covers whole Germany and some neighbouring countries. It has 97 grid cells in west-east and also in south-north direction. The domains are shown in Figure 3.4. Both domains consist of 27 layers in a terrain following coordinate system. The time period between March 23 to April 10, 2009 was simulated using a timestep of 180 s in the parent grid and 60 s in the nest.

The model physics schemes are listed in Table 3.2. The microphysics scheme accounts for 6 forms of water including ice, snow and graupel. The surface physics include soil temperature and moisture in 6 layers and snow and frozen soil in multiple layers. The boundary layer is represented by a prognostic turbulent kinetic energy scheme. Also included are schemes for surface physics, longwave and shortwave radiation, cumulus clouds and urban physics.

The model is driven by global fields of meteorological variables. Therefore, FNL[3] (final) operational global analysis data from NCEP on a $1.0° \times 1.0°$ grid available every 6 hours is taken. The sea surface temperature is updated using global satellite data from NCEP[4]. The informations about the underlying surface including static fields of vegetation, terrain height, reflectivity and so on, are also taken into account.

[3] http://rda.ucar.edu/datasets/ds083.2/
[4] http://polar.ncep.noaa.gov/sst/oper/Welcome.html

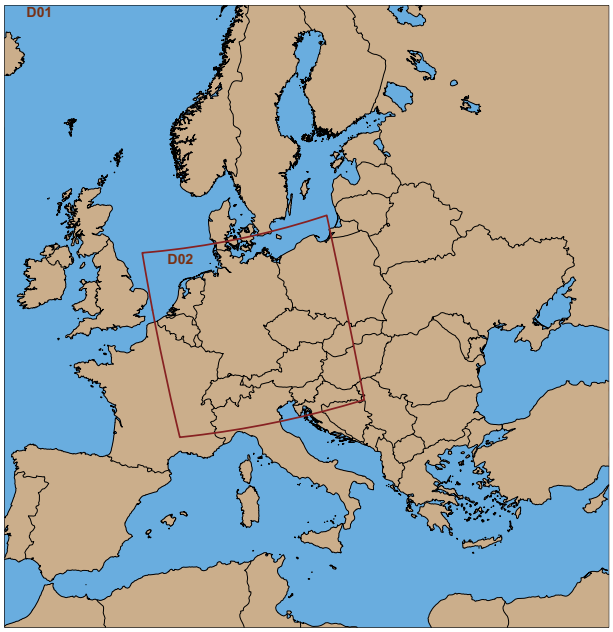

Figure 3.4.: *Model domains, with D01 is the coarse domain with a horizontal resolution of 36 km and D02 is the nested domain with a horizontal resolution of 12 km.*

3.5.3. Emissions

For a full simulation with WRF-Chem, gridded emissions of gases and particles are needed as a model input. Usually, PM emissions are reported as total mass concentration fluxes (PM_{10}, $PM_{2.5}$ and compound-wise). Therefore, EC and OC emission rates are estimated by using factors to derive them from total PM emissions (Bond et al., 2004; Streets et al., 2001). These emission factors are then combined with fuel consumption data that is reported for different sectors and fuel types. Often, total particulate matter is split into fine (PM_1) or ($PM_{2.5}$), as well as coarse particles (PM_{10}). From these fractions, EC emission rates in PM_1, $PM_{2.5}$ and PM_{10} are derived. Four main data sources were used to derive the high resolution EC/OC emission inventory developed in the framework of the European integrated project on aerosol cloud climate and air quality interactions (EUCAARI), which is used this study:

1. GAINS model for PM emissions (Klimont et al., 2002; Kupiainen and Klimont, 2004)
2. Global BC emission inventory for 1996 (Bond et al., 2004)
3. BC emission inventory for China 1995 (Streets et al., 2001)
4. Particulate motor vehicle emissions, ehaust and non-exhaust (Schauer et al., 2006)

The EC emissions are originally gridded on a 1/8° x 1/16° longitude- latitude grid, which corresponds to a spatial resolution of about 7 km. It covers an area over Europe from −10° to 60° in longitude and 35° to 70° in latitude. The targeting year is 2005. Sources such as power plants are gridded as point sources, and emissions from e.g. population or traffic are gridded as area sources. An extract of the inventory can be seen in Figure 3.5, where the emission rates of EC in PM_{10} are mapped on a 4 km WRF grid. Urban areas such as Berlin in the northeast of Germany, but also important roads and ship-tracks reflect in the EC emission rates.

Physics	Scheme	Comments
microphysics	Lin et al. (1983)	bulk water microphysical parametrization technique for 6 forms of water (including ice, snow and graupel)
surface	RUC land surface model	operational scheme with soil temperature and moisture in 6 layers, multilayer snow and frozen soil physics
boundary layer	Mellor-Yamada-Janjic (Janjic, 1994)	prognostic turbulent kinetic energy with local vertical mixing
cumulus	Grell 3D	improvement of the Grell-Devenyi scheme (Grell and Devenyi, 2002)
urban	urban canopy model	3-category model with surface effects of roofs, walls and streets
shortwave radiation	Goddard scheme (Chou et al., 1998)	two-stream model including clouds, gases and aerosols
longwave radiation	RRTM	accounts for multiple bands, trace gases and microphysics species

Table 3.2.: *Summary of of physical settings, following the description in the tutorial of WRF v3.3.*

To make use of this high spatial resolution of the EUCAARI EC/OC inventory, but also account for possible changes in emissions since 2005, the EC emissions from the Arctic research of the composition of the troposphere from aircraft and satellites (ARCTAS) inventory[5] developed by D. Streets and Q. Zhang with a targeting year of 2008 was used to scale the EUCAARI emissions. This was done by calculating the EC emissions in both inventories on a 1° x 1° grid by simply averaging the emission rates in the original grid. A scaling map was then derived by dividing each ARCTAS emission rate in individual 1° grid cell by the corresponding EUCAARI EC emission rate in the same grid cell. The resulting scaling map for the nested domain is shown in Figure 3.6. It can be seen that there are some grid cells with very low scaling factors at this locations, where EC emissions in EUCAARI contain point sources with very high emission rates. This suggests the assumption that point source emissions are not included in ARCTAS. For that reason, these very low scaling factors were not considered when multiplying the scaling map with the original EUCAARI emissions in the last step of this scaling procedure. The emissions of other compounds over Europe such as SO_2, NO_x, CO, NH_3 and NH_4 are originally on a 0.5° grid and are taken from EMEP. The targeting year is 2008. The emissions of volatile organic compounds (VOC) are given as total emissions from the reanalysis of the troposhperic chemical composition (RETRO) emission inventory and were splitted to compounds used in CBMZ chemical mechanism of WRF-Chem.
Biogenic emissions from the model of emissions of gases and aerosols from nature (MEGAN) (Guenther et al., 2006), as well as, wildfires that are detected by moderate resolution imaging spectroradiometer (MODIS) are considered.

3.5.4. Aerosol mass absorption coefficient adjustment in WRF-Chem

For calculating optical aerosol properties using Mie theory for spheres, the particle size and the refractive index must be known. The method of calculating volume equivalent diameters assigned to each MOSAIC bin and the corresponding refractive indices is described in Barnard

[5] http://www.cgrer.uiowa.edu/arctas/emission.html

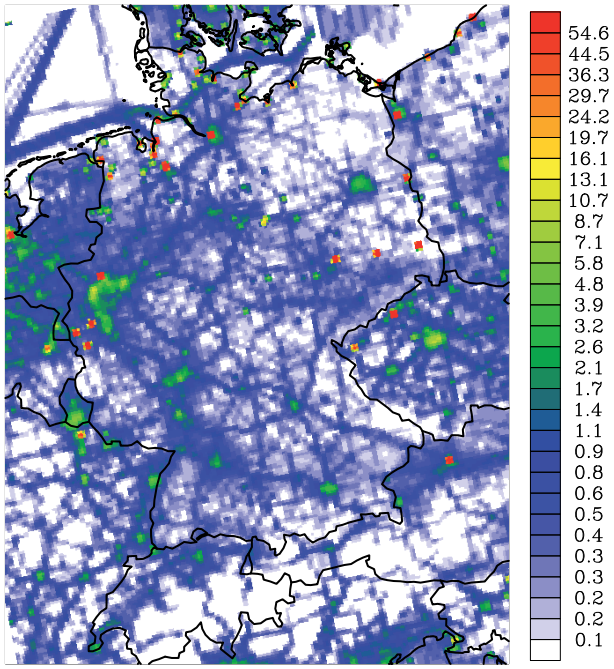

Figure 3.5.: *Emission rates of EC ($ng\,m^2\,s^{-1}$) on a grid with a horizontal resolution of 4 km.*

et al. (2010) and will only be briefly summarized here. In WRF-chem, the chemical masses and number concentrations are given for each of the 4 bins and each of the 11 chemical compounds. Taking densities for each chemical substance, the masses are converted to volumes, which are used to derive the volume equivalent diameter by dividing the summed volume over all chemical substances by the particle number concentration in each bin, separately. The bulk refractive indices for each bin are derived by a mixing rule described in Bond and Bergstrom (2006). In this method, the refractive indices are calculated by volume weighted averaging, as described in Section 2.3.1. All these calculations are performed in a subroutine called 'optical_prep_sectional'. Since the optical properties are very sensitive to the refractive index of BC, this parameter was chosen for the adjustment of the modeled (δ_{mod}) to the measured mass absorption coefficient δ_{GC} values.

For this procedure, a full model run was first performed using all original settings. In the next step, the simulated mass concentrations of all chemical constituents are read in from the model output. Using bilinear interpolation, the model mass concentrations are calculated at the locations, where δ_{GC} measurements are available. Passing the interpolated mass concentrations of all chemical constituents to the subroutine described above, volume equivalent diameters and corresponding refractive indices are derived, which in turn are passed to the Mie subroutine to calculate absorption coefficients of the modeled particle population at individual measurement sites. It is important to mention that the absorption coefficients are calculated for dry particles by setting the aerosol water content to zero before passing the mass concentrations to 'optical_prep_sectional'. This is done to make the modeled optical properties comparable to the measured values, since optical properties are sensitive to the aerosol water content. Following Equation 2.11 and dividing the modeled dry absorption coefficients by the modeled BC mass concentrations, values of δ_{mod} are derived at each of the measurement locations. This procedure can be summarized by the following scheme:

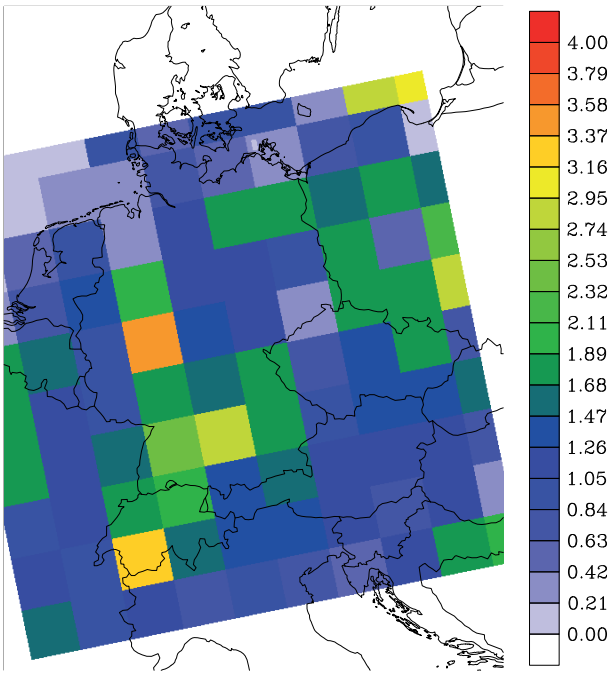

Figure 3.6.: *Scaling map from quotient of ARCTAS and EUCAARI EC emissions on a grid with a horizontal resolution of* 1° .

1. Getting mass concentrations from full model run.
2. Interpolate mass concentrations to measurement site coordinates.
3. Setting aerosol water to 0.
4. Calculate volume equivalent diameter and refractive index in subroutine 'optical_prep_sectional'.
5. Calculate optical properties in subroutine 'mieaer'.
6. Calculate δ_{mod}.

.

The deviation between δ_{mod} and δ_{GC} is calculated by using Equation A.1 with $K = 5$, because values of δ_{GC} from 5 measurement sites are used. For this approach, the imaginary part of the complex refractive index of BC is the independent variable q in Equation A.1. Repeating the presented steps (4.) to (6.) several times with modified q according to the algorithm presented in Appendix A, the deviation between δ_{mod} and δ_{GC} can be minimized, and a new imaginary part of the complex refractive index can be found. If this value should be used in WRF-Chem, the model has to be recompiled with the new imaginary part, which has to be set in the subroutine 'optical_prep_sectional'.

4. Experimental Results

4.1. Calibration of the Raman-Spectrometer

4.1.1. Reference material and filter substrate

Prior to the calibration of the Raman spectrometer for the determination of atmospheric GC mass concentrations, the applicability of furnace soot (Printex®90) as a calibration substance was tested. Particles were generated as described in Section 3.3.3 and sampled on the filter substrates. The corresponding Raman-spectra were measured for different samples. Exemplary spectra of Printex®90, atmospheric particles and the blank filter substrate are shown in Figure 4.1. The spectra were evaluated by applying a Levenberg-Marqardt algorithm (Press et al., 1986) in order to fit 3 modes to the characteristic GC signal. According to Section 2.3.3 these modes are a combination of the G and D_2-band, the D_3-band and the D_1 band. For simplicity, the D_4-band was not considered. The starting values of the full width at half maximum (FWHM), intensity and position of the modes were chosen to be the same for each spectrum. The average position of the G-peak was found to be $1594.4\,\mathrm{cm}^{-1}$ with a standard deviation of $0.2\,\mathrm{cm}^{-1}$. For atmospheric samples, the G-band position is at $1595.9\,\mathrm{cm}^{-1}$ with a higher variability of $0.9\,\mathrm{cm}^{-1}$. Considering values that are given in literature ranging from $1571\,\mathrm{cm}^{-1}$ (pure graphite) to $1598\,\mathrm{cm}^{-1}$ for different types of soot Sadezky et al. (2005), the differences in the graphitic structure between Printex®90 and atmospheric soot particles should only be small. The properties of the other 2 fitted bands are also only slightly different. The intensity ratio of the G- and the D_1-peak was found to be inversely proportional to the size of the graphite crystals (Tuinstra and Koenig, 1970), as mentioned in Section 2.3.3. For the analyzed samples in this study it was $1.36 \pm 0.03\,\mathrm{cm}^{-1}$ for Printex®90 and $1.31 \pm 0.02\,\mathrm{cm}^{-1}$ for atmospheric samples and therefore again very similar for both types of soot.
A particle number size distribution of the Printex®90 was measured with a TDMPS system downstream of the mixing chamber. It shows a mono-modal shape with a maximum around 90 nm (Figure 4.1). Typical mobility diameters of regional and urban background soot particles are in a similar size range (Rose et al., 2006).
As mentioned before, Raman-spectroscopy is sensitive to the graphitic structures in atmospheric particles. Therefore, the fractions of GC in Printex®90 and atmospheric samples were compared. The GC fractions were defined by using natural (Graphite Powder Natural, Alfa Aesar) and synthetic (Graphite puriss., Sigma Aldrich) graphite. Fractions of EC and OC in these graphite samples were determined by using a thermographic method based on the VDI (1999) guideline and described in Section 3.2.3. A third step was added to this procedure heating the sample to 850 °C in an oxygen atmosphere and detecting the released CO_2. By treating the graphite samples with the prescribed steps, it was found that the EC and OC fractions were

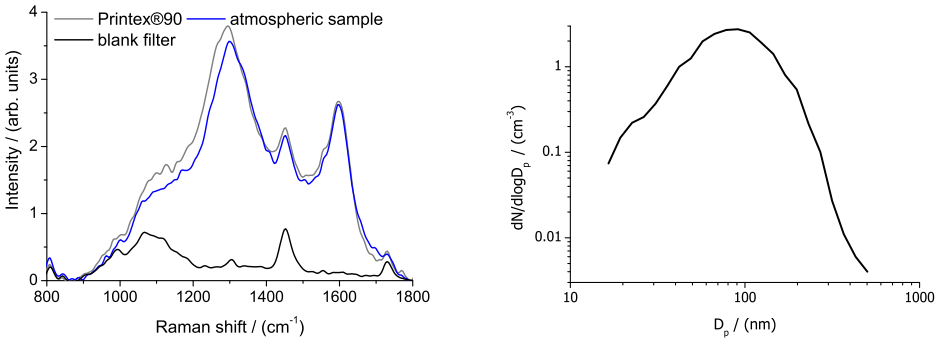

Figure 4.1.: *Comparison of Raman spectra of Printex® 90, atmospheric particles and the blank filter substrate (left) and size distribution of airborne Printex® 90 particles measured with a Twin Differential Mobility Analyzer (TDMPS) (right). Raw concentrations are used.*

very small and nearly all carbon was pyrolized in the third step. For that reason, the carbon that is released from either Printex®90 or atmospheric samples during the third step is also attributed to the GC fraction in these samples. In Figure 4.2, the fractions of EC and GC in the total non-organic carbon for 9 atmospheric, 4 Printex®90 and 2 graphite samples are shown. The $PM_{2.5}$ atmospheric samples were taken at the regional site in Melpitz. Problems associated with the potential misinterpretation of carbonate carbon (e.g. $CaCO_3$) as GC at temperatures above 650 °C are mitigated by analyzing the $PM_{2.5}$ aerosol reservoir, since the fraction of carbonate carbon in this size range is generally low (e.g. Huang et al., 2006). While the GC fractions in graphite samples were nearly 100%, they were smaller for atmospheric (21 %) and Printex®90 (20 %) samples. This indicates that the GC fraction in atmospheric soot particles and in Printex®90 are very similar. Uncertainties of the thermographic methods are mainly due to charring of the OC fraction during the first step, because a correction by monitoring the reflectance of the analyzed sample was not applied. This may result in an underestimation of OC and an overestimation of EC (ten Brink et al., 2004). Since a notable fraction of OC was found in the atmospheric samples in contrast to the Printex®90 samples, the EC fraction in atmospheric samples might be slightly overestimated, if some of the OC charred during step 1, which could not be further quantified. Nevertheless, the small differences between these 2 types of soot, regarding also size and structure, indicate the applicabilaty of Printex®90 as a calibration substance.

Problems that occur during the Raman-measurement are mainly due to fluorescence and heating of the sample, which are visible as high signal intensities at low ($\approx 500\,\mathrm{cm}^{-1}$) and high ($\approx 3000\,\mathrm{cm}^{-1}$) Raman-shifts, respectively. To eliminate these signals in individual Raman-spectra, it is necessary to normalize to a stable pattern that is always present in all spectra. Therefore, it was tested if stable modes of the blank GF10 MAAP filter substrate are visible in the Raman spectrum. For this purpose, all spectra were normalized on the band between 1453 and $1530\,\mathrm{cm}^{-1}$, and the average as well as the standard deviation was calculated (Figure 4.3). Unsurprisingly, the standard deviation in the normalization wavenumber region is very small. It increases towards lower and higher wavenumber shifts, but shows no local maximum in regions

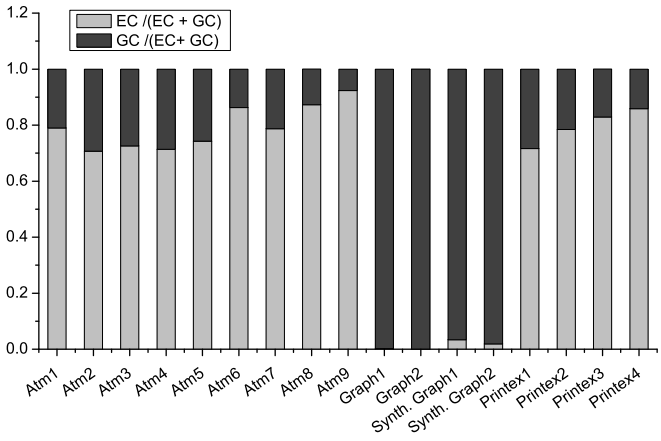

Figure 4.2.: *Fraction of graphitic carbon (GC) in the non-organic total carbon concentration (EC +GC) in atmospheric (Atm), graphite (Graph, Synth. Graph) and Printex® 90 (Printex) samples.*

of other bands of the filter substrate (e.g. $2900\,\mathrm{cm}^{-1}$). This is an indicator that the relative intensities of the bands remain constant so that the filter band between 1453 and $1530\,\mathrm{cm}^{-1}$ can be used for normalization.

4.1.2. Results

The results of the calibration experiment presented in Section 3.3.3 are shown in Figure 4.4. A linear relationship between the mass loading of Printex®90 on the glass microfiber filters and the corresponding G-band integral was found at least in the mass loading range between 0.5 and $6\,\mu\mathrm{g\,cm}^{-2}$. This is a typical range of mass loadings that are reached inside the MAAP, if the transmission is set to 50 % as it was done in the present study. The corresponding integrals over the G-band were between 40 and 800 a.u.. Using an error weighted orthogonal regression that assumes errors in both variables (Cantrell, 2008), the slope (0.00681) and the offset (0.332) were calculated. The linear relationship is very good with an coefficient of determination of 0.95. Using the calibration function to derive m_{load}, m_{GC} can be determined by

$$m_{GC} = \frac{m_{load}\, A_{spot}}{\dot{V}\, t_{samp}}. \tag{4.1}$$

In this equation, A_{spot} is the diameter of the loaded spot, $\dot{V}$ is the flow rate and t_{samp} is the sampling time.

The uncertainties of the integral over the G-band were estimated by repeating the Raman measurements for several filters. The uncertainties may come from small inhomogeneities in the particle loading on filters or from the spectra evaluation described in the Section 3.3.2. On average, an uncertainty of 7.5 % was found. The errors of m_{load} were estimated by Gaussian error propagation using the uncertainties of the A_{spot} (5 %), the flow ratio (7 %) and the Printex®90 mass on the weighed filter samples (6 %). On average, an error of 15 % was found for m_{load} on the glass microfiber filter (cf. Nordmann et al., 2009). The uncertainties of the fit function were

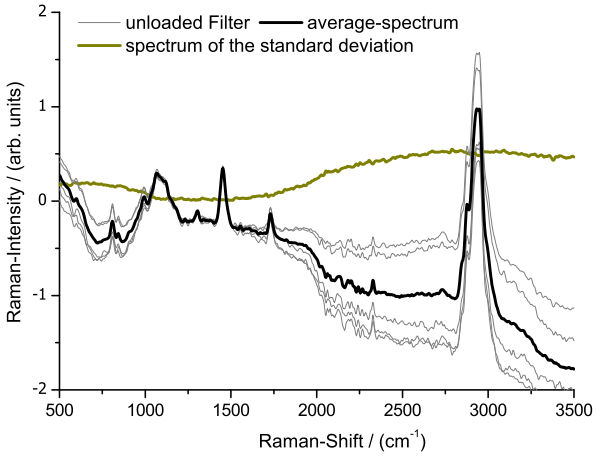

Figure 4.3.: *Comparison of 5 Raman-spectra of the unloaded filter medium, which is used inside the Multi Angle Absorption Photometer (MAAP).*

derived as a byproduct of the orthogonal regression procedure to be 1.4 % for the slope and 4 % in offset. The reason for this positive offset could not be identified. One possible explanation refers to the procedure of gravimetric mass determination. When polycarbonat filters are loaded, they may become electrostatically charged. This charge could not be removed prior the weighing procedure, and may have influenced the results. Moreover, a slight dependence of the offset on the flow ratio between weighing filter medium and the filter medium that is measured by Raman-spectroscopy was found, whereas slopes remain nearly constant. Because of these different flow ratios, different ratios of filtration efficiencies of the filter media may lead to this systematic offset. Nevertheless, the usage of a non-zero offset would lead preferably to a non zero offset when comparing absorption coefficients and m_{GC} of individual filter samples, as will be shown in a later section. This means, that absorption occurs although GC concentrations are zero. For that reasons, this non zero offset is neglected when deriving m_{load} from the integral over the G-band in the Raman-spectrum in the following steps.

4.1.3. Evaluation of the Raman-method

The new Raman-method was evaluated using EC measurements of atmospheric particle samples of different aerodynamic size classes, that were taken on aluminium foils using Berner impactors. The EC masses were determined by the method described in Section 3.2.3. For the comparison with the Raman spectroscopic measurements of m_{GC} in samples of MAAP measurements, m_{EC} was summed over the first 3 of 5 impactor stages, whereas stage 3 had a cut of 1.2 μm aerodynamic particle diameter. The upper cut off for the particle samples taken inside the MAAP was 1 μm. Since m_{EC} from Berner samples represent daily averaged values, the Raman-spectroscopic derived m_{GC} values had to be averaged, giving different values different weights depending on t_{samp}.

The resulting scatterplot is shown in Figure 4.5. The values of m_{EC} and m_{GC} ranged between 0.2 and 3.5 μg m^{-3}. The linear regression shows a slope of 1.05 and a negligible non-zero offset of -0.09 with a coefficient of determination of 0.87. This indicates a very close relationship between

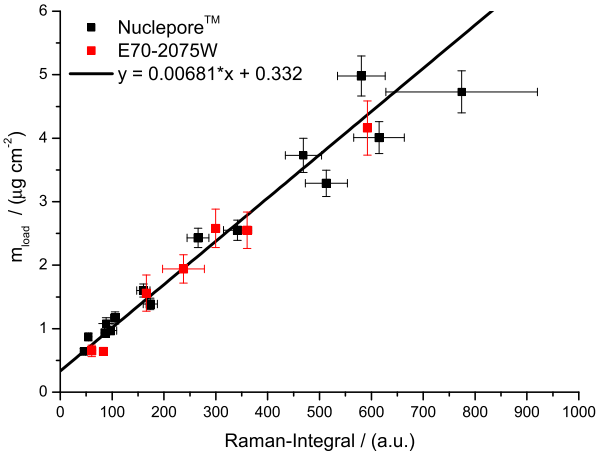

Figure 4.4.: *Relation between gravimetric mass of Printex® 90 and corresponding integral over the G-band in the Raman-Spectrum. Black dots indicate the usage of a polycarbonate filter and red dots of a quartz filter.*

m_{EC} and m_{GC} and that the new Raman method is comparable to the thermographic method.

4.2. Atmospheric measurements

4.2.1. Spatial and temporal variability of aerosol absorption coefficients in Germany

Continuous measurements of the aerosol light absorption coefficient were performed in GUAN since the beginning of 2009 using MAAPs at 10 observation sites. The time series of the smoothed daily averaged values of σ_{ap} is shown in Figure 4.6. It can be seen that the lowest values were observed in the winter months at the high altitude site Zugspitze. Taking all other sites into account, σ_{ap} covered approximately 3 orders of magnitude during the winter season. In contrast, only 2 orders of magnitude were covered in the summer months. The values at the mountain sites were in the same size range as regional background σ_{ap}, which was rarely observed in the winter months. This can be attributed to the enhanced vertical exchange of polluted air masses in the summer, induced by the enhanced incoming solar radiation. In Figure 4.6, three episodes are marked, which will be referred to later in this chapter. These episodes were chosen for applying the new Raman-method presented in Section 4.1, because they were characterized by rather different meteorological conditions.
Based on half hourly measurements, relative frequency distributions were calculated to illustrate typical value ranges of σ_{ap}. The data was sorted into logarithmic equidistant classes, since at least 3 orders of magnitude are covered. Properties of the resulting distributions were derived by fitting logarithmic normal distributions. The most obvious differences can be seen from the position of the maxima of the distributions in dependence on the measurement site in Figure 4.7. In urban areas, especially at near traffic observational sites, the most frequent values of σ_{ap} at Leipzig Eisenbahnstraße and Dresden-Nord are 13.5 and 16.5 Mm^{-1}, respectively. Typical values at urban background locations such as Augsburg and Leipzig-IfT were around 7 and 10 Mm^{-1}.

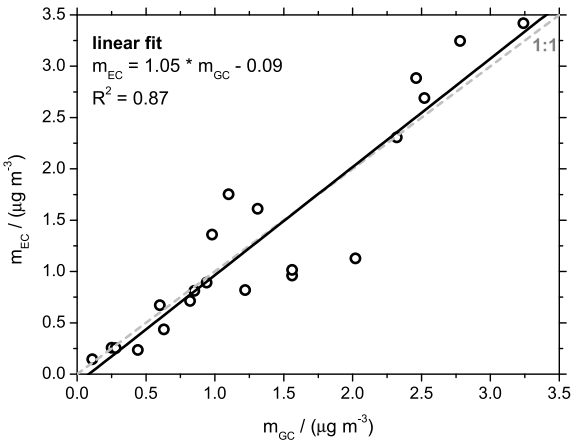

Figure 4.5.: *Comparison between daily averaged mass concentrations of graphitic carbon (m_{GC}) from Raman-spectroscopy and corresponding mass concentrations of elemental carbon (m_{EC}) from thermographic analysis of daily Berner impactor samples.*

The distributions at the regional observation sites Melpitz, Bösel and Waldhof show maxima between 2.5 and 4 Mm^{-1}. It has to be mentioned that only data of approximately one year was available for Waldhof. Slightly lower values were observed at mountain sites, ranging between 0.7 and 2.2 Mm^{-1} at Zugspitze and Hohenpeißenberg, respectively. The broadest distribution was calculated for the Zugspitze data. It has a tendency to higher values and could therefore be best fitted by using two modes indicating a pronounced seasonality of the absorption coefficient. The diurnal variability of the measured σ_{ap} for different measurement sites can be seen in Figure 4.8. The calculations based on the half hourly values for weekdays (Monday-Friday) and weekends (Saturday and Sunday) were performed separately. The weekdays diurnal cycle at near traffic urban observation sites shows a maximum in the morning and a second broad maximum in the afternoon, probably due to enhanced emissions during the rush hours. At urban background locations, the diurnal cycle exhibits also a bimodal shape with a maximum in the morning, but the second maximum is later in the evening in comparison to the traffic sites. The diurnal cycles at regional sites are similar, but the maxima are less pronounced. At the mountain sites, only one broad maximum at the early afternoon is visible in the diurnal cycle. At the weekend, the highest concentrations at urban and regional sites are observed during night, which is in contrast to the diurnal cycles during weekdays. Opposed to this, the diurnal cycle at mountain sites is very similar during weekdays and weekend.

4.2.2. Size distributions of EC and non-volatile particles

To characterize soot particles concerning their size, measurements of m_{EC} in different aerodynamic diameter classes and volume size distributions of ambient and non-volatile particles were used. The approach of measuring the number size distributions of a heated initially monodisperse aerosol stream was applied in other studies by using a volatile tandem differential mobility analyzer to determine the external and internal mixed fraction of non-volatile particles (Frey et al., 2008), which are associated with soot particles (Rose et al., 2006). In this study, a

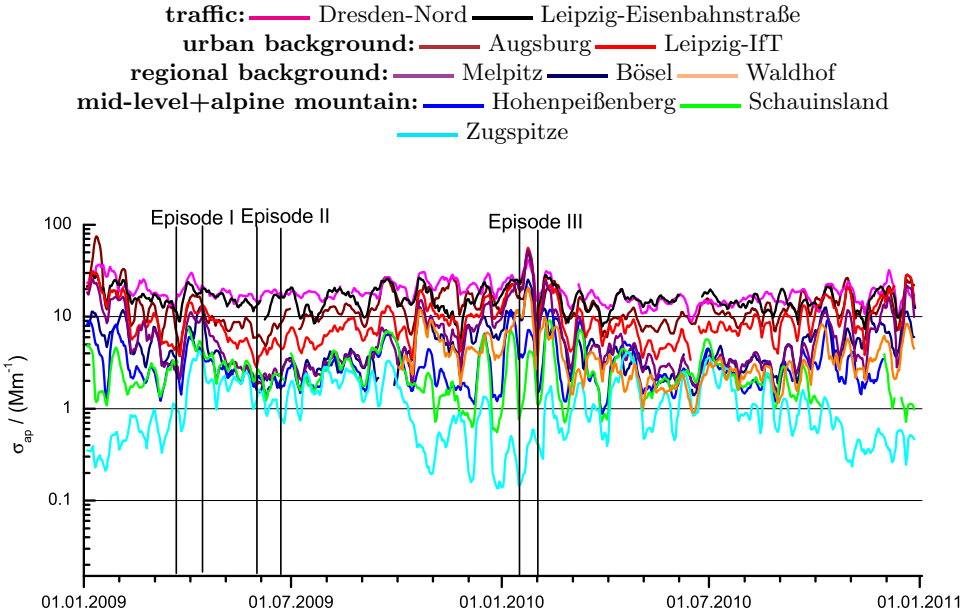

Figure 4.6.: *Annual cycle of the absorption coefficient (σ_{ap}) at 10 observation sites of the German Ultrafine Aerosol Network (GUAN). Episodes I to III are marked because of later reference.*

simplified version was used just heating the whole polydisperse aerosol stream to 300 °C and evaporating volatile compounds to measure the non-volatile size distribution as described in Section 3.2.2. Unfortunately, it is not possible to have a closer structural insight into measured soot particles in terms of e.g. fractal dimension, size of monomers or effective density of these fractal agglomerates by having only this information. Fractal properties can be determined by transmissions electron microscopy (Köylü et al., 1995; Park et al., 2004a; Wentzel et al., 2003). To estimate effective densities, tandem measurements selecting particles with a specific mobility diameter and subsequently classify these monomobile particles according to their aerodynamic size (Kelly and McMurry, 1992; Park et al., 2003).

Average mass size distribution from at least 45 Berner impactor samples from each measurement site collected in 2009 and 2010 were compared. A homogeneous distribution of available samples over typical air masses and over all seasons was aspired, to be as representative as possible for a time period of 2 years. The mass size distributions were derived by dividing the average masses in each of the 5 size classes by the width of each size bin and subsequently fitting log-normal functions to the distributions. In addition, the volume size distributions of non-volatile particles are shown as an average for the years 2009 and 2010. It has to be mentioned that the mass size distributions from Berner sampling refer to the the aerodynamic diameter of EC, whereas non-volatile volume distribution are based on the mobility diameter.

The results are shown in Figure 4.9. In general, the maximum of the EC mass size distributions shifts to larger diameters, when going from urban to mountain sites. This behaviour can not be seen in the non-volatile volume size distributions. Going more into detail, the maximum of the mass size distribution of EC is around 400 nm at the traffic site Leipzig-Eisenbahnstraße. The maximum of the non-volatile volume size distribution is slightly shifted to smaller diame-

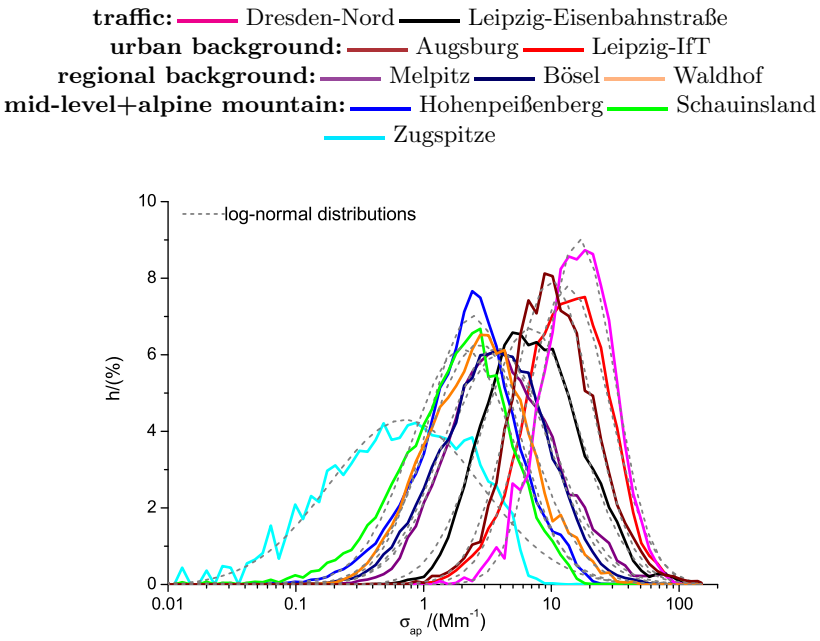

Figure 4.7.: *Statistics on 2 year absorption coefficient (σ_{ap}) measurements at 10 observation sites in the German Ultrafine Aerosol Network (GUAN). Gray lines represent fitted log-normal functions.*

ters around 300 nm. For urban and regional background locations, particles with diameters of around 550 nm dominated the EC mass concentrations. In contrast, the non-volatile volume size distribution shows a maximum around 250 nm. At mountain observation sites the difference is even larger with a maximum of the mass sizes distributions around 800 nm and again between 200 and 300 nm for the non-volatile volume distribution.
One plausible explanation for the observed difference is based on the mixing state of atmospheric soot particles. In previous studies it was found by using electron microscopy that a significant fraction of soot particles exist internally mixed at regional sites in contrast to urban locations (e.g. Hasegawa and Ohta, 2002). Assuming that the ambient soot particles carried a volatile shell especially at mountain sites, it would evaporate in the thermodenuder leading to a particle shrinking. This particle would be classified in a higher diameter class if it is unconditioned, which is the case for the mass size distributions. In contrast, freshly emitted soot particles at traffic locations do not carry a shell, which could evaporate in the thermodenuder. This is in agreement with the measurements of non-volatile particle volume size distributions and mass size distributions of EC. It has to be mentioned that a comparison of these distributions from different measurement devices is highly uncertain, since they are based on different diameter definitions and not necessarily the same aerosol reservoir.

4.2.3. Correlation of absorption coefficient with non-volatile particles

To get further information about the size of the particles that are responsible for light absorption, the particle ambient and thermodenuder number size distributions measured in 2009 and 2010 were compared to measured values of σ_{ap} in terms of the coefficient of determination (R^2).

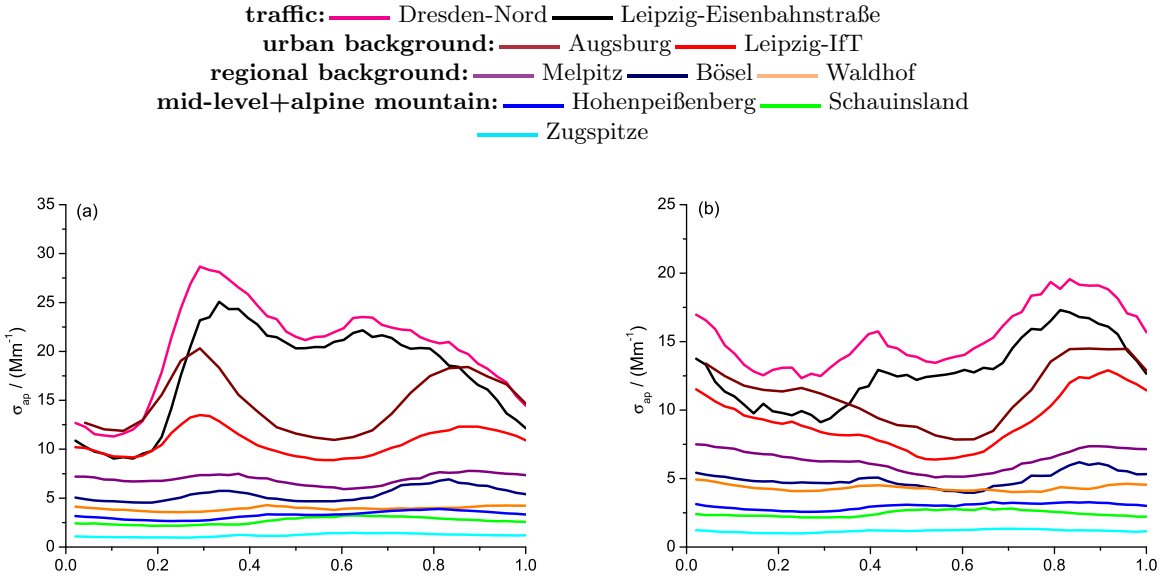

Figure 4.8.: *Diurnal cycle of absorption coefficients (σ_{ap}), for (a) from Monday to Friday and (b) from Saturday to Sunday.*

Therefore, the time series for each size bin for 2009 and 2010 was compared to the time series of the absorption coefficient, in each case for a temporal resolution of 30 minutes. The results are shown in Figure 4.10. In general, σ_{ap} is much better correlated with the non-volatile than with the ambient particle number size distributions. The maxima of R^2 range between 0.7 and 0.9 for thermodenuder distributions. The position of the maximum is between 100 and 200 nm at all observation sites. A tendency to a bimodal shape can be seen, especially for the mid-level mountain sites. As indicated by the width of the curves of R^2, the absorbing particles seem to be relatively homogeneously distributed over a broad diameter range of the non-volatile particles. The values of R^2 are almost entirely above 0.6 in a diameter range between 80 and 500 nm. They decrease rapidly below and above this range.

For ambient particles, highest values of R^2 are between 0.5 and 0.8. Except for the traffic site Leipzig-Eisenbahnstraße and the urban background site Augsburg, the curves of R^2 exhibit a more or less pronounced bimodal shape. The first maximum is located at around 100 nm at all sites and therefore matches the aforementioned position of the maxima of the R^2 curves for non-volatile particles. This is especially visible for the traffic site, where freshly emitted absorbing soot particles are measured. These particles are mostly externally mixed and should therefore maintain there size after passing the thermodenuder. The position of the second and more distinct maximum varies between 250 and 500 nm at non-urban observation sites and is even more pronounced than the first maximum. Assuming a large fraction of internally mixed soot particles at rural and mountain locations, this behavior could be explained by a volatile shell surrounding the soot particles and evaporating in the thermodenuder. Taking the difference between the position of the maximum in the R^2 curves for ambient and non-volatile particles as a rough estimation of the diameter shrinking of light absorbing particles, values between 20 and 70% can be derived. The lowest value is estimated for the urban background site Leipzig-IfT.

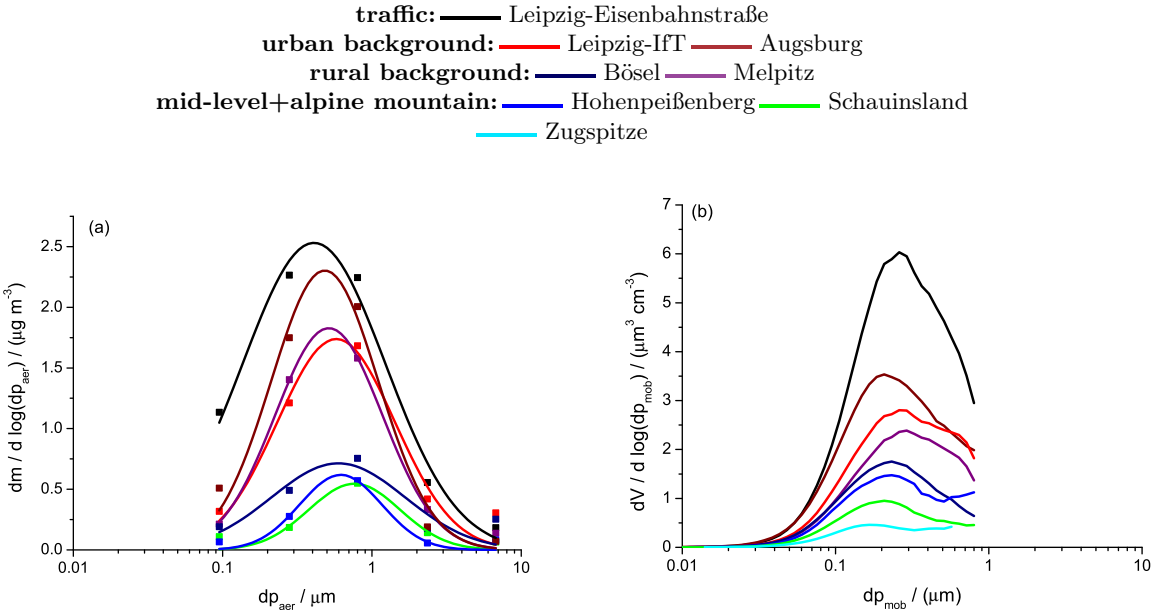

Figure 4.9.: *Characteristic size distributions from 2009 and 2010 for (a) mass concentration of EC in 5-stage Berner impactor samples (logarithmic normal distributions are fitted to each data set), and (b) non-volatile particle volume from SMPS/TDMPS-thermodenuder measurements.*

4.3. Experimental mass absorption coefficients for atmospheric soot particles

4.3.1. Meteorological characterization of measurement periods

For the application of the Raman-method to determine m_{GC} and δ_{GC} of atmospheric soot particles, 3 distinct time periods in 2009 and 2010 were chosen. The meteorological conditions during these time periods are presented in this section. To illustrate relevant meteorological fields, WRF runs were performed in the domains presented in Section 3.5.2. The general weather situation in Central Europe is generally characterized by a change of more or less persistent pressure patterns at the surface. These changes occur due to long waves in the upper troposphere, which can be seen in the field of the geopotential height of the 500 hPa surface. This height is in close relation to the temperature of the air mass, which means that cold air masses are characterized by a low geopotential, in contrast to warm air masses. However, these long waves show troughs (i.e. regions with low geopotential) as well as ridges. Air masses were classified and labeled according to their source regions and transformations described in Geb (1981). Source regions were identified using 72 h backward trajectories calculated with the HYSPLIT model (Draxler and Hess, 1997). Following the method of Geb (1981), every air mass is characterized by an annual cycle of the pseudopotential temperature. Therefore, fields of the pseudopotential temperature[1] were taken into account and compared to tabulated values in Geb (1981).
The first episode (Episode I) of interest was from March 25 to April 10, 2009. In the beginning, the general weather situation was characterized by a trough situated over Central Europe, re-

[1] http://www.wetter3.de/Archiv/

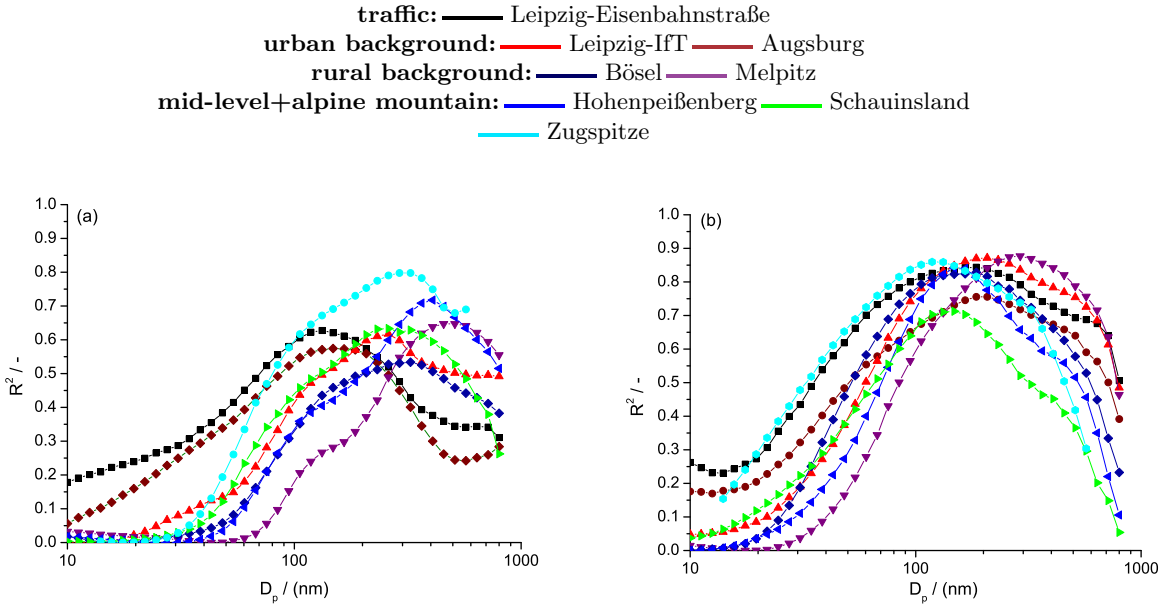

Figure 4.10.: *Coefficient of determination (R^2) between absorption coefficient (σ_{ap}) and volume size distributions of 2009 and 2010 for (a) ambient aerosol measurements and (b) non-volatile particles after thermodenuder.*

sulting in mostly maritime subpolar air masses (mP), which influenced large areas of Germany. Some shorter waves that moved along the frontal zone led to incorporations of warmed maritime subpolar air masses (mPs). The air masses mP and mPs dominated the meteorological situation from the beginning of Episode I to March 31, 2009. With the shift of the trough to eastern directions, the circulation pattern changed. The following ridge can be seen in the field of the geopotential height of the 500 hPa layer, shown in Figure 4.11. Corresponding to this situation in higher altitudes, the temperature in 850 hPa increased because of the transport of warm air masses from southeastern directions. At the surface, a high pressure area was centered over Bulgaria, leading to a transport of warm continental air masses to Germany. Trajectories indicate that the dominant air masses between 01 April to 10 April, 2009 were aged maritime (xSp) and continental (cSp) air (Figure 4.12). The second episode (Episode II) of interest was from May 29 to June 20, 2009. In this period, Central Europe was influenced by a persistent trough, as can be seen from the exemplary field of the 500 hPa geopotential height in Figure 4.13. Corresponding trajectories are shown in Figure 4.14. The temperature in the 850 hPa level was only around 0 °C , especially in the northern part of Germany, which is lower in comparison to the long-term average. Corresponding to this persistent trough, several low pressure systems with their fronts influenced the weather in Germany. In the beginning of this time period, large areas of Germany were situated downstream of the trough leading to a meridional transport of maritime subpolar air (mP). Subsequently, air masses of the type mP were transported to the north of Spain, so that Germany was situated upstream of the trough and maritime air of the mid-latitudes (mSp) could establish. A change between mostly these 2 types of air masses repeated until the end of Episode II, but with a tendency to mSp in the southern and mP in the northern part of Germany.

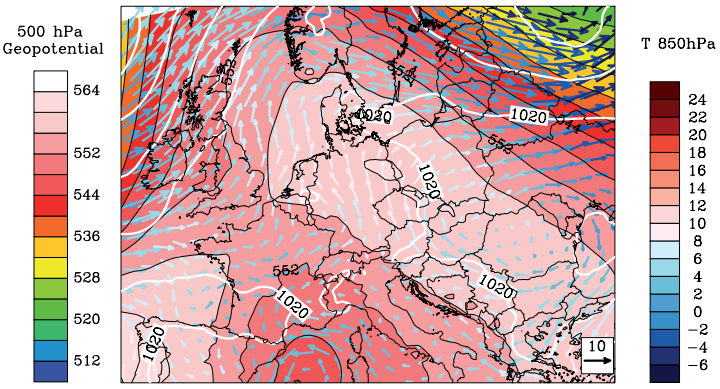

Figure 4.11.: *Typical meteorological situation during Episode* I*: Geopotential of the 500 hPa atmospheric level, wind vectors at the 850 hPa level colored in dependence of the 850 hPa temperature and the pressure at sea level (white contour lines) calculated with Weather Research and Forecast model (WRF v3.2.1) for April 03, 2009 at 12:00.*

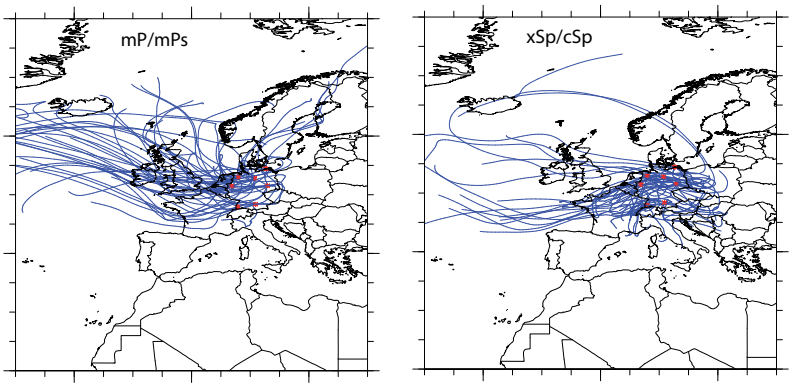

Figure 4.12.: *Backward trajectories during Episode* I*, calculated for 72 h using HYSPLIT model (Draxler and Hess, 1997). This episode could be separated into 2 parts. Between March 25 and March 31, 2009 a maritime warmed subpolar air mass (mPs) dominated the meteorological situation. Between April 01 and April 10, 2009 mostly aged martime (xSp) and continental (cSp) air masses influenced Germany.*

The general weather situation during the winter episode between January 24 and January 31, 2010 (Episode III) was characterized by a high pressure system in the northeastern part of Europe. Due to the very cold air in this region, the 500 hPa geopotential was very low, as can be seen from Figure 4.15. Especially the eastern part of Germany was influenced by this cold continental air mass with a temperature of −12 °C in the 850 hPa level. Low temperature with humid air and a noticeable wind from eastern and northeastern directions was situated in large areas over Germany. The vertical stratification showed a temperature inversion with slightly colder air at the surface and warmer air with a relative humidity of 20% reside over it, as can be seen from Figure 4.16. The air mass can be classified as almost entirely continental subpolar (cP) until January 27, 2010, as can be seen from the trajectories in Figure 4.17. With a new trough establishing in Central Europe from north-western directions, cP was forced back to eastern Europe after January 27, 2010, and maritime air masses from polar (mP) and arctic (mA) origins established in Germany until the end of Episode III.

Following the air mass classification described above, Episode I will be splitted into 2 parts, the

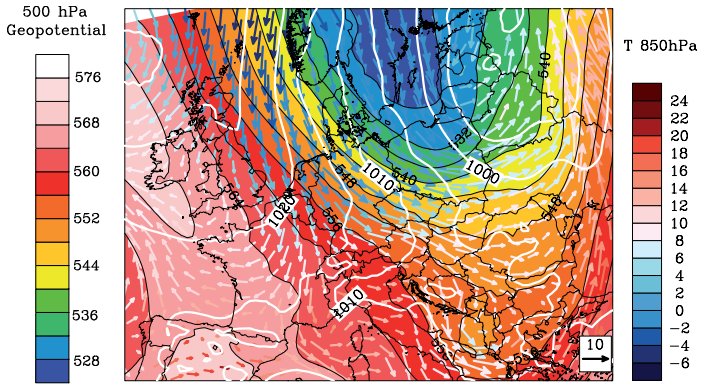

Figure 4.13.: *Typical meteorological situation during Episode* II*: Geopotential of the 500 hPa atmospheric level, wind vectors at the 850 hPa level colored in dependence of the 850 hPa temperature and the pressure at sea level (white contour lines) calculated with Weather Research and Forecast model (WRF v3.2.1) for June 03, 2009 at 12:00.*

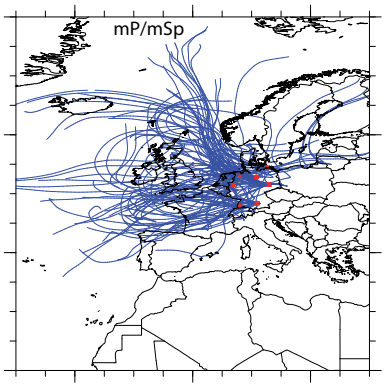

Figure 4.14.: *Backward trajectories during Episode* II*, calculated for 72 h using HYSPLIT model (Draxler and Hess, 1997). This episode was dominated by maritime subpolar air (mP) and martime air of the mid-latitudes (mSp).*

more maritime Episode I - m and the more continental Episode I - c. Since Episode II was almost entirely influenced by maritime air masses, it is designated as Episode II - m in the following steps of data evaluation. The winter Episode III can also be clearly separated into 2 parts, which will be designated as Episode III - c and Episode III - m.

4.3.2. Determining experimental mass absorption coefficients

Theoretical studies based on Mie-calculations for simple spherical particles as well as more complicated algorithms for the calculation of optical properties of fractal aggregates suggest that the mass absorption coefficient of soot particles from the combustion of diesel fuel will most often not exceed $7\,m^2\,g^{-1}$ at a wavelength of 550 nm (Fuller et al., 1999). Assuming a soot particle that is freshly emitted, its structure exhibits branches of small spherical primary particles. As its fractal dimension increases from values around 1.5 to values greater than 2, the particle appears more compact with a less open structure. This often occurs during atmospheric aging processes. Such a particle would have a decreased mass absorption coefficient in comparison to an open structured soot particle with a same number of primaries (Liu et al., 2005). The opposite occurs

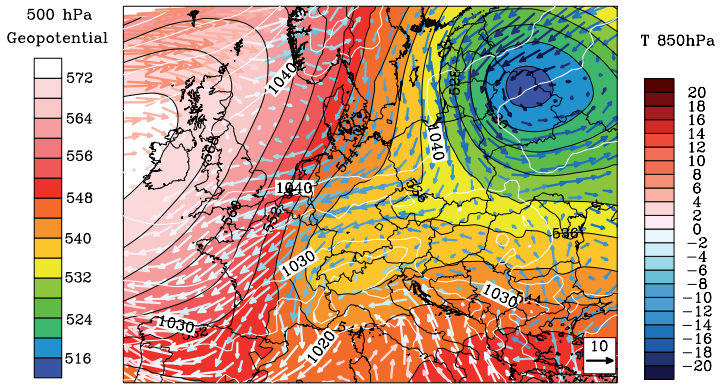

Figure 4.15.: *Typical meteorological situation during Episode* III*: Geopotential of the 500 hPa atmospheric level, wind vectors at the 850 hPa level colored in dependence of the 850 hPa temperature and the pressure at sea level (white contour lines) calculated with Weather Research and Forecast model (WRF v3.2.1) for January 26, 2010 at 12:00.*

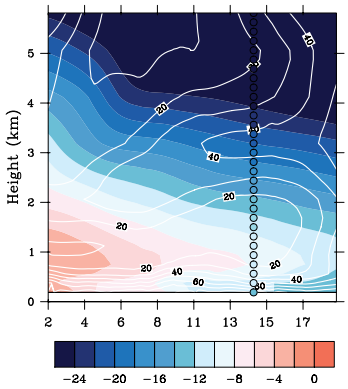

Figure 4.16.: *Cross section along* 52.2 °N *with temperature shown in colored contour levels and relative humidity in white contour lines calculated with Weather Research and Forecast model (WRF v3.2.1) for January 26, 2010 at 12:00. The vertical temperature profile measured in Lindenberg (*52.2 °N , 14.1 °E *) is shown in color-filled circles.*

if the particles are getting internally mixed with other non-absorbing substances during atmospheric aging processes. This leads to an enhancement of the mass absorption coefficient, with values that could be greater than 10 $m^2\,g^{-1}$ at a wavelength of 550 nm (Fuller et al., 1999).
In this work, particle samples were analyzed by means of Raman-spectroscopy stemming from near traffic, urban background, regional and mountain observational sites in 3 episodes and therefore cover a broad range of the state of soot from freshly emitted to aged particles. As described in the section before, the 3 episodes are separated into 5 distinct prevailing air masses. All values of m_{GC} were calculated by using Equation 4.1. The mass absorption coefficient of graphitic carbon (δ_{GC}) can then be calculated from the quotient of σ_{ap} and m_{GC}, as given in Equation 2.11. Characteristic values were obtained from the slopes of orthogonal regression lines for each site and each air mass (cf. Table 4.1). The uncertainties of each single value of δ_{GC} were derived by Gaussian error propagation, using the uncertainties from MAAP measurements of 12% (Petzold and Schönlinner, 2004) and the errors of m_{GC}. Errors of m_{GC}, in turn, were determined by Gaussian error propagation. Therefore, the errors of the integral over the

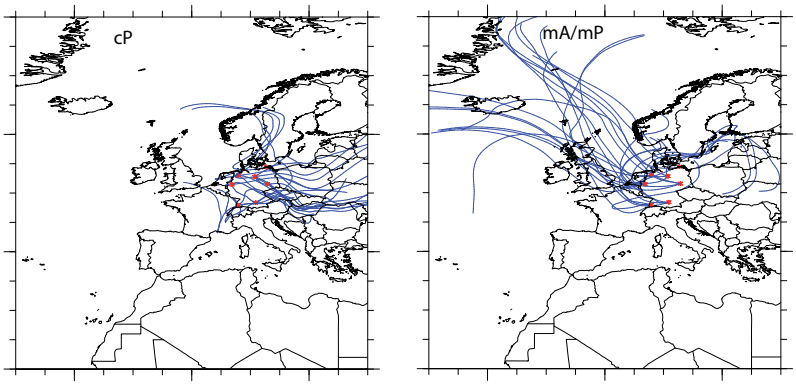

Figure 4.17.: *Backward trajectories during Episode* III*, calculated for 72 h using HYSPLIT model (Draxler and Hess, 1997). This episode could be separated into 2 parts. Between January 24 and January 28, 2010 a continental subpolar air mass (cP) dominated the meteorological situation. Between January 29 and January 31, 2010 a mostly maritime arctic (mA) and maritime subpolar (mP) air mass was situated over Germany.*

G-band in the Raman-spectrum of atmospheric particle samples on the MAAP filter medium were determined by repeated measurements of individual samples to be 14%. The measurements were partly repeated with a time delay of several months, leading to a larger difference. This may explain the difference to the uncertainty that was presented in Section 4.1.2 for laboratory generated Printex®90 particles. The calibration constant, that is used to convert the integral over the G-band into a mass loading on the filter medium, has an uncertainty of 1.4%. Additional errors of m_{GC} are introduced by A_{spot} (5%), $\dot{V}$ (3 - 7%) and t_{samp} (around 1%). These errors propagate to an uncertainty of m_{GC} of 15 -17%. Altogether, this leads to an uncertainty of single values of δ_{GC} of 19 - 21%, depending on the flow rate that is used inside the MAAP at individual measurement sites.

Episode I

In association with the meteorological situation in Episode I - m, m_{GC} ranged between 0.1 μg m^{-3} at mountain locations to 4 μg m^{-3} at near traffic observation sites as can be seen in Figure 4.18. Corresponding absorption coefficients for each sample from MAAP measurements showed also relatively low values between 0.2 Mm^{-1} and 18 Mm^{-1} at mountain and traffic sites, respectively. As the meteorological situation changed in Episode I - c, m_{GC} increased to values between 0.5 and 15 μg m^{-3} with corresponding values of σ_{ap} between 2 and 55 Mm^{-1}. This more polluted continental air mass established later at the observation sites in the southern part of Germany with the largest delay at the alpine site Mt. Zugspitze. For both air masses, the time series of m_{GC} and σ_{ap} show a very similar temporal behavior, indicating a high degree of correlation and the dominance of GC as absorbing species in the measured particle populations.
At the traffic observation site, δ_{GC} exhibited a slight decrease as the air mass changed from Episode I - m to Episode I - c. The variability over the whole time period was comparably large with single values between 2.5 and 7.5 m^{2}g^{-1}. This also reflects in the large scatter of the data points in a m_{GC} - σ_{ap} plot, as can be seen in Figure 4.21. Orthogonal regressions yielded charac-

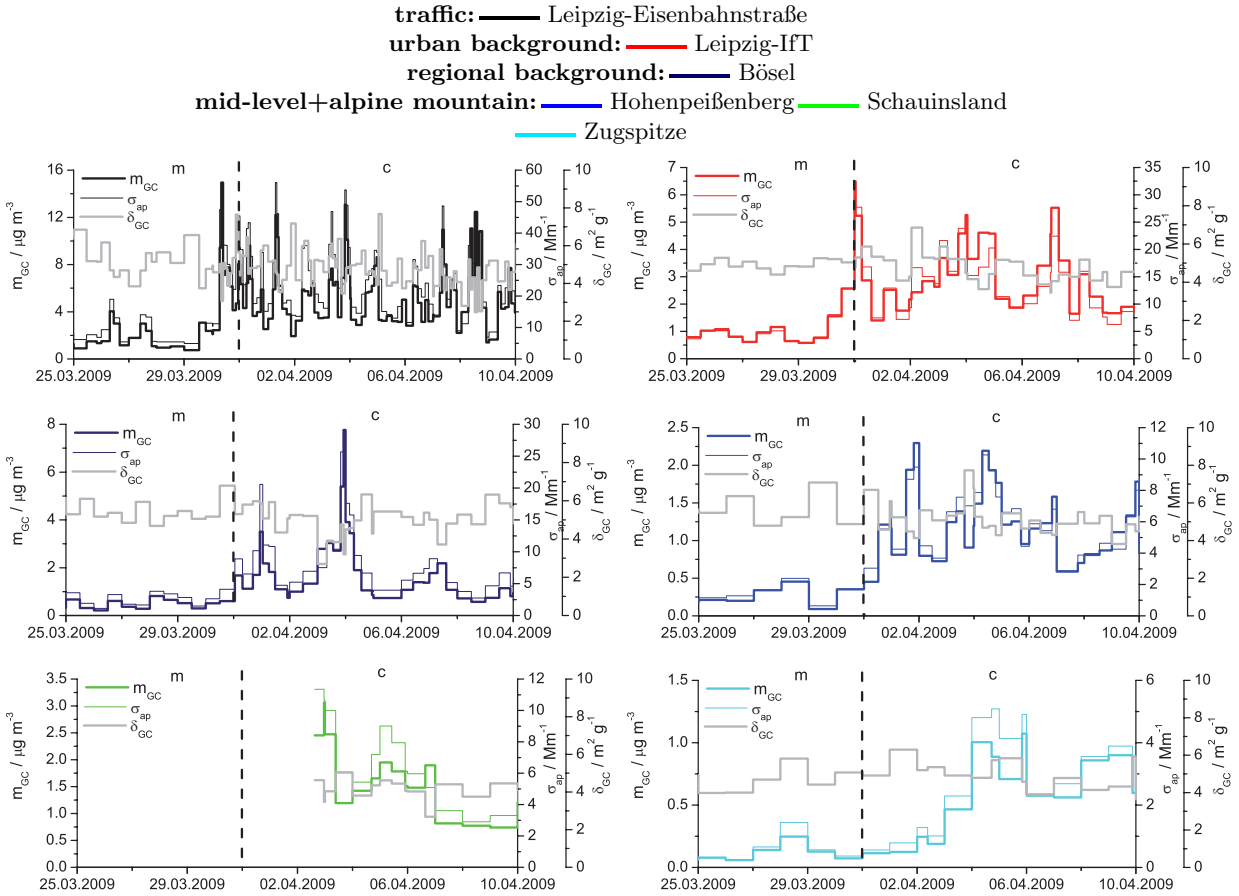

Figure 4.18.: *Determining aerosol mass absorption coefficients (δ_{GC}) during Episode* I*: Time series of the mass concentration of graphitic carbon (m_{GC}), absorption coefficient (σ_{ap}) and δ_{GC} at 6 observation sites in the German Ultrafine Aerosol Network (GUAN). A change from mostly maritime (m) to mostly continental (c) air masses is indicated by a vertical line.*

teristic values of 4.6 $m^2\,g^{-1}$ for Episode I - m and Episode I - c but with a poorer correlation for the more continental air mass. At the urban background site, the temporal variability of δ_{GC} was not so pronounced as at the traffic site. A characteristic value of 5.1 $m^2\,g^{-1}$ was determined for Episode I - m and Episode I - c, respectively. At the regional background site in the northwestern part of Germany, the variation of individual single values of δ_{GC} was between 2.6 and 6.7 $m^2 g^{-1}$, with a short time period in the beginning of Episode I - c showing decreased values. The slopes of the regression lines are 5.5 $m^2\,g^{-1}$ for the more maritime and 5.2 $m^2\,g^{-1}$ for the more continental air mass. At the mid-level mountain Hohenpeißenberg in the southern part of Germany, the observed values of δ_{GC} ranged between 3.8 and 7.7 $m^2 g^{-1}$. From the regression, values of δ_{GC} of 4.4 $m^2\,g^{-1}$ for Episode I - m and 4.6 $m^2\,g^{-1}$ for Episode I - c were calculated. Results for the other mid level mountain site Schauinsland show lower values of δ_{GC} but, unfortunately, only about 50% of data was available because of a failure of the measurement system. However, the samples are only from Episode I - cfor which a value of δ_{GC} of 4.2 $m^2\,g^{-1}$ was determined by regression. The time series of δ_{GC} for the alpine mountain site Zugspitze shows a weak maximum between March 27 and April 06, 2009 with highest values around 6.3 $m^2 g^{-1}$. The lowest values observed in the whole time period were around 3.7 $m^2 g^{-1}$. From regression, values of δ_{GC} of 5.8 $m^2\,g^{-1}$ for

Episode I - m and 4.8 $m^2 g^{-1}$ for Episode I - c were calculated. In summary and as can be seen in Figure 4.21, individual single values of δ_{GC} were almost entirely between 2 and 8 $m^2 g^{-1}$. The correlations between m_{GC} and σ_{ap} are at least good at individual observation sites.

	Episode I				Episode II		Episode III				Berner	
	m		c		m		c		m			
	slope	R^2	slope	R^2	slope	R^2	slope	R^2	slope	R^2	slope	R^2
Leipzig-Eisenbahnstraße	4.60	0.86	4.62	0.75	-	-	-	-	-		6.75	0.65
Leipzig-IfT	5.07	0.99	5.11	0.86	4.21	0.73	6.58	0.68	4.23	0.96	6.34	0.77
Augsburg	-	-	-	-	-	-	-	-	-	-	6.59	0.66
Bösel	5.50	0.90	5.21	0.93	5.00	0.84	6.42	0.53	5.99	0.97	4.57	0.84
Melpitz	-	-	-	-	-	-	7.39	0.63	5.45	0.98	4.43	0.84
Hohenpeißenberg	4.43	0.97	4.58	0.85	5.11	0.77	6.11	0.86	5.24	0.99	4.32	0.75
Schauinsland	-	-	4.21	0.87	4.29	0.81	4.29	0.94	5.82	0.97	6.41	0.48
Zugspitze	5.81	0.98	4.79	0.81	3.97	0.96	4.91	0.99	3.85	0.98	-	-

Table 4.1.: *Results of orthogonal regressions with slope (characteristic value of δ_{GC} in $m^2 g^{-1}$) and coefficient of determination (R^2) between mass concentration of graphitic carbon (m_{GC}) and absorption coefficient (σ_{ap}) for 3 episodes divided into 5 different air masses (m=maritime, c=continental, cf. Section 4.3.1) and Berner samples of 2009 and 2010.*

Episode II

Additional filter samples stemming from Episode II - m were selected for a subsequent Raman spectroscopic analysis. Observed values of m_{GC} ranged between 0.1 $\mu g\, m^{-3}$ at mountain sites and 2.9 $\mu g\, m^{-3}$ at the urban site, respectively. The variability at individual measurement sites is small in comparison to Episode I. Corresponding values of σ_{ap} were expectably highest (9.4 Mm^{-1}) at the urban site and with lowest (0.4 Mm^{-1}) at mountain sites. As already observed for Episode I, a very similar temporal behavior of m_{GC} and σ_{ap} can be seen in Figure 4.19, identifying again GC as the dominant absorber of solar radiation at a wavelength of 637 nm. The variability of δ_{GC} during this time period at the urban background site was smaller with values between 3.2 and 5.5 $m^2 g^{-1}$. Applying again the method of orthogonal regression, a typical value of 4.2 $m^2\, g^{-1}$ was calculated. Regional background values of δ_{GC} ranged between 2.4 and 6.5 $m^2 g^{-1}$. The lowest value of this range was measured for a very short sampling period and, therefore, possesses larger uncertainties mainly due to lower filter loadings. When considering this fact, the lower bound would be 3.9 $m^2 g^{-1}$. A value of 5 $m^2\, g^{-1}$ was characteristic for the regional site during Episode II - m. Regarding the increased uncertainty for very short sampling periods, the range of δ_{GC} at the mid-level mountain site Hohenpeißenberg is 4.2 - 6.2 $m^2\, g^{-1}$ with a characteristic value of 5.1 $m^2 g^{-1}$. At the other 2 mountain sites, the ranges of δ_{GC} were 3.5 - 6.6 $m^2\, g^{-1}$ at Schauinsland and 3.6 - 5.7 $m^2\, g^{-1}$ at Zugspitze. From regression, values of δ_{GC} of 4.3 $m^2\, g^{-1}$ for Schauinsland and 4.0 $m^2\, g^{-1}$ for Zugspitze were derived. In summary, the value range of δ_{GC} is narrower in comparison to Episode I. The majority of values was between 4 and 6 $m^2 g^{-1}$, as can be seen in Figure 4.21.

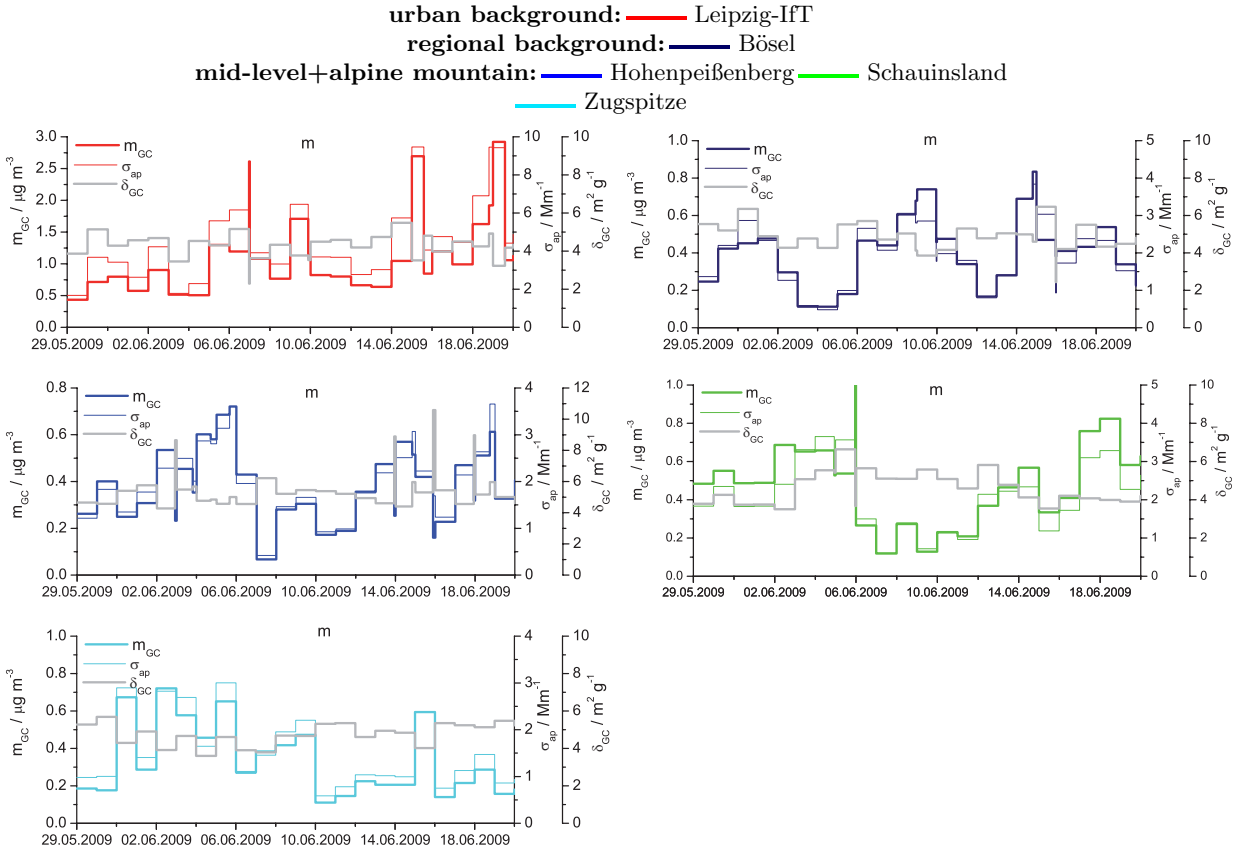

Figure 4.19.: *Determining aerosol mass absorption coefficients (δ_{GC}) during Episode* II*: Time series of the mass concentration of graphitic carbon (m_{GC}), absorption coefficient (σ_{ap}) and δ_{GC} at 6 observation sites in the German Ultrafine Aerosol Network (GUAN). This episode was dominated by maritime air masses (m).*

Episode III

To determine the range of δ_{GC} in Central Europe during winter months, additional samples from Episode III were measured. The time series of σ_{ap}, m_{GC} and δ_{GC} are shown in Figure 4.20. Especially at the measurement sites in the northern part of Germany, very high values of m_{GC} occurred in association with the meteorological situation during Episode III - c. The maxima of m_{GC} in this continental air mass ranged between 0.2 $\mu g\,m^{-3}$ at the alpine mountain site and 20 $\mu g\,m^{-3}$ at the urban site. Corresponding values of σ_{ap} were in the range between 1.2 and 104 Mm^{-1}. These high values indicate a very polluted conditions, which are likely to be caused by high emissions because of low temperatures in combination with an inversion layer at the surface, as shown in Section 4.3.1. Such a situation was not often observed in the years 2009 and 2010, as can be seen from the time series of absorption coefficients in Figure 4.6. A steep decrease in m_{GC} and σ_{ap} occurred at the beginning of Episode III - m. Observed values ranged between 0.07 - 2.4 $\mu g\,m^{-3}$ and 0.4 - 10 Mm^{-1}, respectively. The temporal behavior of m_{GC} and σ_{ap} is very similar for both very different air masses. In contrast to Episode I and Episode II, a clear change in individual single values of δ_{GC} during Episode III can be seen at the regional and urban observation sites in the northern part of Germany. At the urban background site in Leipzig, δ_{GC} had its maximum of 8.3 $m^2\,g^{-1}$ in the continental air mass. The lowest values

down to $4\,m^2\,g^{-1}$ were observed in the marine air mass. Typical values from regression were $6.6\,m^2\,g^{-1}$ for Episode III - c and $4.2\,m^2\,g^{-1}$ for Episode III - m. A similar temporal behavior was found for the regional background sites Bösel and Melpitz, with maximum values up to $10\,m^2\,g^{-1}$ and minimum values of $4.3\,m^2g^{-1}$. One implausible value of δ_{GC} measured for Bösel was not considered. For Episode III - c, the slopes of regression lines are $6.4\,m^2\,g^{-1}$ for Bösel and $7.4\,m^2\,g^{-1}$ for Melpitz. In contrast, for Episode III - m they are smaller with values of δ_{GC} of $6.0\,m^2\,g^{-1}$ for Bösel and $5.5\,m^2\,g^{-1}$ for Melpitz. It has to be mentioned that the correlations at these 3 sites are only moderate for Episode III - cwith coefficients of determination between 0.53 and 0.68. In addition, the regression lines show a systematic positive offset. At mountain sites, δ_{GC} was relatively constant, although signals of this continental air mass are visible in the time series of m_{GC} and σ_{ap}. At the mid-level mountain sites Hohenpeißenberg and Schauinsland, the ranges of values are 4.4 - $7.1\,m^2\,g^{-1}$ and 3.6 - $6.8\,m^2g^{-1}$, respectively. Characteristic values of δ_{GC} during Episode III - c were $6.1\,m^2\,g^{-1}$ at Hohenpeißenberg and $5.2\,m^2\,g^{-1}$ at Schauinsland. In Episode III - m, values slightly changed to 5.2 and $5.8\,m^2g^{-1}$, respectively. Nearly no change was observed at the alpine mountain site with a range of values of δ_{GC} between 4.6 and $6.2\,m^2g^{-1}$. Characteristic values were 4.9 and $3.9\,m^2\,g^{-1}$ during Episode III - c and Episode III - m, respectively.

4.3.3. Discussion of mass absorption coefficients

Variability

Summarizing the results presented in the previous section, the highest values during Episode I were measured at Zugspitze and Bösel and the lowest at Schauinsland. The range of values of δ_{GC} from orthogonal regression is between 4.2 and $5.8\,m^2g^{-1}$. In Episode II the range of characteristic values is similar, with δ_{GC} between 4.0 and $5.1\,m^2g^{-1}$. In contrast, a broader range of characteristic values was determined for the winter Episode III, with δ_{GC} between 3.9 and $7.4\,m^2g^{-1}$. A tendency to higher values in winter season can be observed, since δ_{GC} for Episode III - m is also mostly higher than δ_{GC} in maritime air masses in the summer. Cozic et al. (2008) found an opposite behavior on the high alpine mountain site Jungfraujoch and suggested that higher summer values are due to enhanced coatings of soot particles with organic materials because of a higher photochemical activity.

The observed variability in δ_{GC} may result from a significant fraction of particles, which are not GC but contributed to σ_{ap}. For example, organic aerosol particles may contribute to light absorption coefficients (Andreae and Gelencsér, 2006). Adapt this on the current study using MAAP and Raman-spectrometer to determine δ_{GC} it turns out that possible contributions of organic aerosols to σ_{ap} are rather small at a wavelength of 637 nm, as can be seen from the steep decrease in absorption spectra towards this wavelength (Sun et al., 2007). Favez et al. (2009) found a contribution of biomass burning aerosols of not more than 8 % at this wavelength. An additional absorber of radiation is mineral dust. Since its absorption is correlated with the particle number concentration greater than 1 μm (Müller et al., 2009) at least near source regions, there should be a negligible influence on PM_1 absorption even if significant amounts of this species would be present. In addition, absorption coefficients of mineral dust decrease strongly

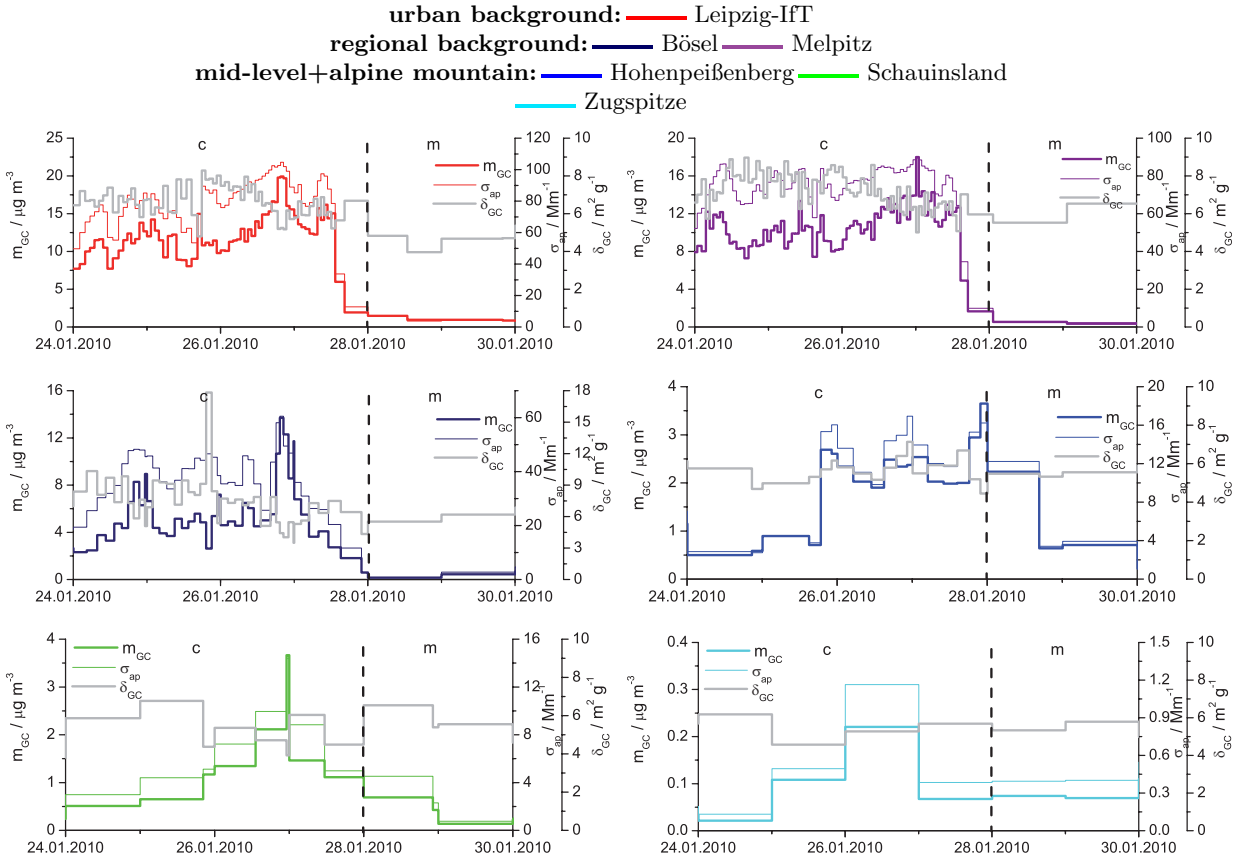

Figure 4.20.: *Determining aerosol mass absorption coefficients (δ_{GC}) during Episode* III*:Time series of the mass concentration of graphitic carbon (m_{GC}), absorption coefficient (σ_{ap}) and δ_{GC} at 6 observation sites in the German Ultrafine Aerosol Network (GUAN). A change from mostly continental (c) to mostly maritime (m) air masses is indicated by a vertical line.*

with increasing wavelength (Petzold et al., 2009).

More likely, the variability in δ_{GC} is due to changes in the state of mixture. In several studies listed in Table 4.2, laboratory generated as well as ambient soot particles were analyzed concerning the effect of a coating on their mass absorption coefficient. In all studies it was found that the mass absorption coefficient increases if particles are getting coated with non-absorbing material. Reported changes in the mass absorption coefficient from laboratory measurement using a single particle soot photometer (Shiraiwa et al., 2010) are for example 50 % as shell volume fraction is 88 %. Using transmission electron microscopy before and after removing water soluble material from the particle samples, Naoe et al. (2009) determined a change of 25 % in the mass absorption coefficient as shell volume fraction is around 50 %.

Regarding the measurement sites of the present work, a larger fraction of coated soot particles can be expected at mountain sites in comparison to near source locations in the urban environment, due to aging processes. This could generally not be confirmed by measurements of δ_{GC}, since the highest values were not measured at mountain sites such as the Zugspitze.

The difference in δ_{GC} between prevailing air masses was systematically analyzed by averaging individual single values of m_{GC} and σ_{ap} for each site and each of the 5 air masses. The resulting scatterplot of average σ_{ap} and m_{GC} is shown in Figure 4.22. Characteristic values of δ_{GC} were

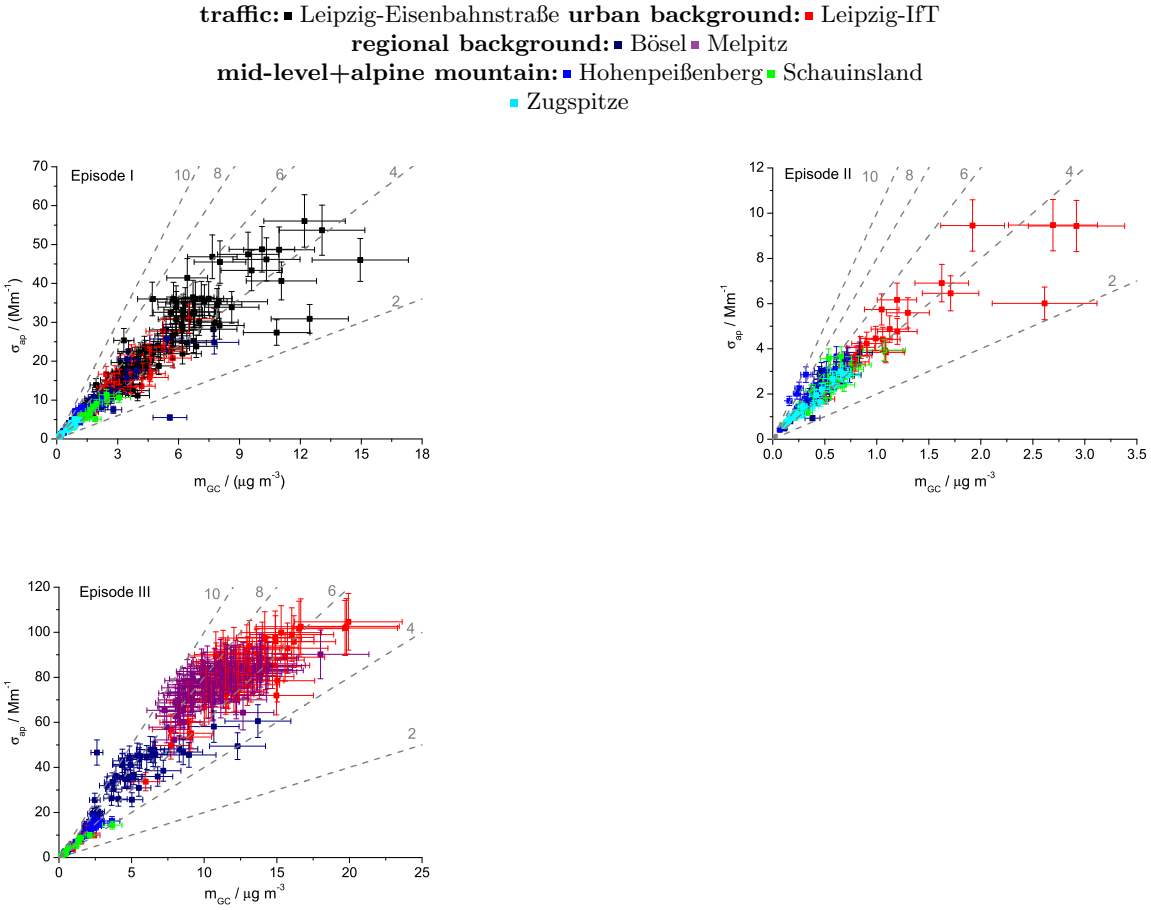

Figure 4.21.: *Scatterplot between mass concentration of graphitic carbon (m_{GC}) and absorption coefficient (σ_{ap}) for every sample of the 3 episodes. Lines with slopes of 2, 4, 6, 8 and 10 $m^2\ g^{-1}$ are added as gray lines for a rough orientation.*

derived from orthogonal regression. Despite particle samples were taken in completely different air masses, the variation of δ_{GC} from regression analysis is only about 17%. The maximum value of $6.3\,\mathrm{m^2\,g^{-1}}$ was determined for the continental air mass during Episode III - c. The lowest value of δ_{GC} was observed during the clean maritime air mass. Regarding the air mass effect, δ_{GC} should be highest in an air mass containing a large fraction of internally mixed (coated) soot particles. The concentrations but also the fraction of internally mixed soot particles should be increased in aged air masses with only a few or even no precipitation events in the last days, since the dominant removal process of soot particles is wet deposition. This should be mostly the case during stable high pressure weather conditions. Adding additional freshly emitted soot particles, the overall state of mixture should not change significantly. In contrast, aged air masses from maritime origins and frequent precipitation processes in the near past should contain lower concentrations but also a high fraction of internally mixed soot particles. Assuming that such an air mass passes over continental areas with fresh soot emissions, an externallyl mixed soot fraction would be added. Depending on the initial concentrations of internally mixed soot particles, the introduced externally mixed fraction may be dominant and, therefore, changing the overall mixing state. This could explain the findings that δ_{GC} is highest in the aged continental air mass during Episode III - c but lowest in the maritime air mass Episode II - m.

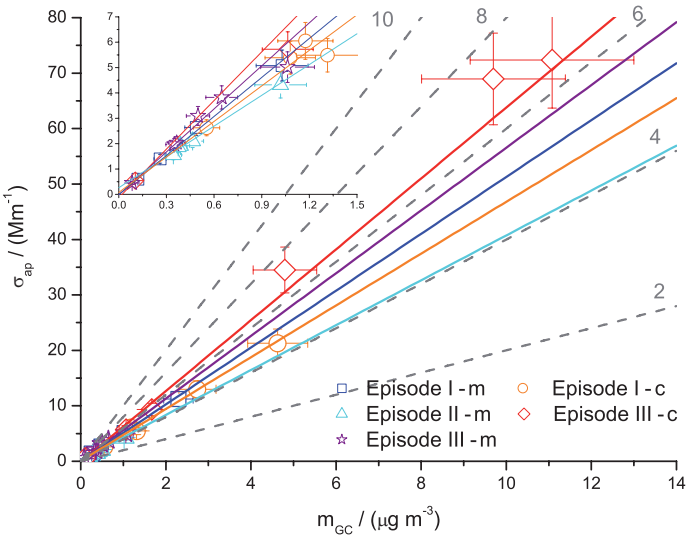

Figure 4.22.: *Scatterplot between mass concentration of graphitic carbon (m_{GC}) and absorption coefficient (σ_{ap}) for prevailing air masses during Episode* I, *Episode* II *and Episode* III. *Lines with slopes of 2, 4, 6, 8 and 10 $m^2\ g^{-1}$ are added as gray lines for a rough orientation.*

Comparison with mass absorption coefficients concerning EC

As previously shown in Section 4.1.3, there is a good agreement between m_{GC} from Raman measurement and m_{EC} from thermographic analysis of Berner impactor samples, at least for the regional observation site in Bösel. Additional Berner samples were taken at traffic, urban and mountain locations. They were compared with the daily averaged absorption coefficients from MAAP in Figure 4.23. Resulting slopes and coefficients of determination are summarized in Table 4.1. The slopes again represent a characteristic mass absorption coefficient designated as δ_{EC} because it is based on EC mass concentrations. Individual single values of δ_{EC} were mostly between 2 and 10 $\mathrm{m^2 g^{-1}}$, except some higher values measured at urban and traffic observation sites. The slopes of the regression lines indicate higher values of δ_{EC} at urban and traffic sites in comparison to regional and mountain sites. Values obtained, ranged between 6.6 and 6.8 $\mathrm{m^2\,g^{-1}}$ and 4.3 and 4.6 $\mathrm{m^2 g^{-1}}$, respectively. The value of δ_{EC} determined for Schauinsland has a higher uncertainty, since the correlation is poor with R^2 of 0.48 and the regression line has a larger positive offset. The reason for the difference between urban and regional sites is unclear but is assumed to have a methodological origin. As mentioned in Section 3.2.3, no charring correction was performed during the thermographic analysis. Assuming 2 particle samples with a constant amount of EC but different amounts of OC, the thermographic analysis would give different concentrations of EC, since different amounts of OC charred during the procedure. Taking this into account, the difference in δ_{EC} between urban and regional sites could be explained by a difference in the average OC/EC ratio, which must have been higher at urban sites. Comparing these findings to δ_{EC} values derived by Petzold and Schönlinner (2004), a nearly similar difference between urban and rural location was found as can be seen in Table 4.2. It is worth mention, that Petzold and Schönlinner used a similar combination of measurement devices. In summary, the ranges of δ_{GC} and δ_{EC} fit very well. The tendency to higher values at urban locations as observed for δ_{EC} can, indeed, not be seen in δ_{GC}.

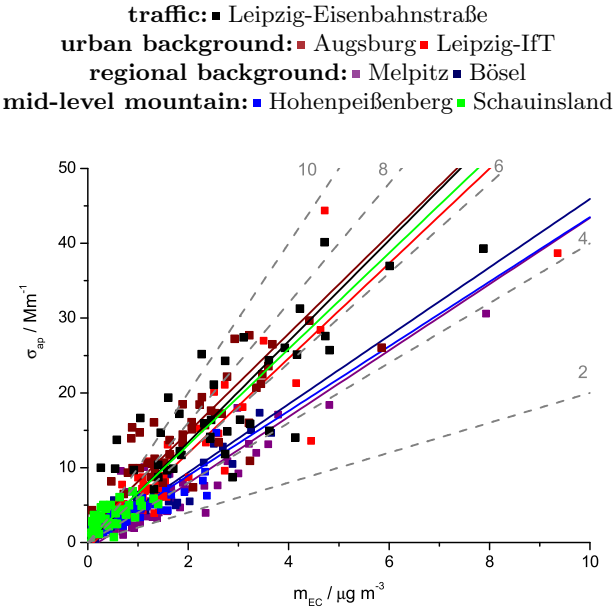

Figure 4.23.: *Scatterplot between mass concentration of elemental carbon (m_{EC}) and absorption coefficient (σ_{ap}) for every Berner sample taken in 2009 and 2010. Lines with slopes of 2, 4, 6, 8 and 10 $m^2\ g^{-1}$ are added as gray lines for a rough orientation.*

Comparison with previous studies

Before comparing the values of δ_{GC} to values in the open literature it has to be mentioned that, in general, mass absorption coefficients of soot may be determined by a combination of various methods for mass concentration and absorption coefficient determination. It has to be considered that different methods of mass determination are not necessarily sensitive to the same properties of soot particles. Depending on the calibration standard used for individual methods, different masses may be measured when analyzing the same soot sample. In addition, the absorption coefficient may introduce uncertainties. Even the unit to unit variability of several photometers such as the particle soot absorption photometer (PSAP) may be up to 30% (Müller et al., 2011). However, the absolute value of δ_{GC} was compared to values of mass absorption coefficients measured in other studies and summarized in Table 4.2. When referring to the listed literature values, the mass absorption coefficient is also designated as δ_{EC}, since for nearly every value soot mass concentration were determined by a thermographic method. For that reason, the observed span of δ_{EC} in Table 4.2 may be due to a difference of soot properties such as size or state of mixture but also due to different measurement methods. However, the values of δ_{EC} range between 3.58 and 18.3 $m^2\ g^{-1}$ for regional, mountain and urban sites in a wavelength range of 550 to 870 nm. In order to compare them, all values were adjusted to the wavelength of the MAAP using an Angström exponent of -1, which is typical for soot. The values measured in the present study are at the lower bound of the cited values of δ_{EC}. Going more into detail, an average value of 11.3 $m^2\ g^{-1}$ can be derived for mountain sites, which is more than a factor of 2 higher than δ_{GC} found in this study. For regional locations, a slightly lower

Site	Type	Author	Absorption coefficient	Mass concentration of soot	Mass absorption coefficient / $m^2\,g^{-1}$
Jungfraujoch, Switzerland	mountain	Cozic et al. (2008)	MAAP (637 nm)	EC/OC[1]	11.1 (summer), 7.4 (winter)
Manora Peak, India	mountain	Ram et al. (2010)	optical attenuation converted to σ_{ap} (687 nm)	EC/OC[1]	14.5 (summer), 11.64 (winter)
Maledives (aircraft)		Mayol-Bracero et al. (2002)	PSAP (550 nm)	EC/OC[2]	8.1
Manaus, Brazil	regional (tropical)	Gilardoni et al. (2011)	MAAP (637 nm)	EC/OC[3]	4.7
Guangzhou, China	regional	Kondo et al. (2009)	PSAP, COSMOS (565 nm)[7]	EC/OC[1]	12.03 (unheated), 9.87 (heated)
Yufa, China	regional/urban	Kondo et al. (2009)	PSAP, COSMOS (565 nm)[7]	EC/OC[1]	15.71 (unheated), 11.64 (heated)
Mexico City, Mexico	regional/ urban	Doran et al. (2007)	Photoacoustic (870 nm)	EC/OC[1]	8.5
Brighton, Colorado	regional	Moosmüller et al. (1998)	Photoacoustic (685 nm)	EC/OC[4]	3.58
Gosan, South Korea	regional	Chuang et al. (2003)	PSAP (550 nm)	EC/OC[1]	12.6 (PM_1), 14.8 (PM_{10})
Finokalia, Greece	regional	Sciare et al. (2003)	PSAP	EC/OC[1]	7.5
kleiner Feldberg, Germany	regional	Petzold and Schönlinner (2004)	MAAP (637 nm)	EC/OC[5]	4.8
Tsukuba, Japan	regional	Naoe et al. (2009)	PSAP (565 nm)	EC/OC[4]	10 (uncoated), 13 (coated)
Berlin, Germany	urban	Petzold and Schönlinner (2004)	MAAP (637 nm)	EC/OC[5]	6.3
Vienna, Austria	urban	Hitzenberger et al. (2006)	MAAP (637 nm)	EC/OC[5]	3.88-8.43
Atlanta, USA	urban	Carrico et al. (2003)	PSAP (550 nm)	EC/OC[1 5 6]	18.3/9.3/5.3
Toronto, Canada	urban	Knox et al. (2009)	Photoacoustic (760 nm)	EC/OC[1]	9.3-9.9 (unheated), 6.9-9.1 (heated)
Tokyo, Japan	urban	Kondo et al. (2009)	PSAP, COSMOS (565 nm)[7]	EC/OC[1]	14.97 (unheated), 6.69 (heated)
Laboratory	flame soot coated (sulfuric acid+water)	Khalizov et al. (2009)	difference extinction and scattering (532 nm)[8]	DMA/APM	8.7 (uncoated), 12.6 (coated)
Laboratory	graphite particles (coated)	Shiraiwa et al. (2010)	Photoacoustic (532 nm)	SP2[9]	5.1 (uncoated), 10 (coated (D_p/D_{core}=2)

[1] EC/OC analyzer Sunset Laboratory, as described in Birch and Cary (1996)
[2] EC/OC by evolved gas analysis, EGA (Novakov et al., 1997)
[3] EC/OC Dual optical carbonaceous analyzer (Sunset Laboratory), EUSAAR2-protocol (Cavalli et al., 2010)
[4] EC/OC by thermal/optical reflectance from desert research institute (DRI) (Chow et al., 1993)
[5] EC/OC by a themal method following VDI (1996)
[6] EC/OC by a Rupprecht and Patashnick Series 5440 ambient carbon particulate monitor
[7] σ_{ap} at 565 nm by a Continuous Soot Monitoring System (COSMOS, Kanomax, Osaka, Japan) Miyazaki et al. (2008)
[8] σ_{ap} at 532 nm by nephelometer and cavity ring-down spectrometer
[9] BC by Laser induced incandescence as described in Gao et al. (2007)

Table 4.2.: *Summary of studies regarding mass absorption coefficients (δ_{EC}).*

average value of 9.4 $m^2\,g^{-1}$ can be calculated from Table 4.2, considering only δ_{EC} for untreated samples. This is again a factor of 2 higher than the values of δ_{GC} observed during Episode I and Episode II. For urban sites, a value of 9.8 $m^2\,g^{-1}$ can be derived. In summary, there is a similar tendency to higher values of δ_{EC} at regional location, as it was found in the present study. In order to eliminate the uncertainty introduced by different absorption measurement devices, only studies using the MAAP were considered in the following. In this case, again, highest values are derived for mountain sites with δ_{EC} of 9.3 m^2g^{-1}. The values of regional and urban sites are 4.7 and 6.2 m^2g^{-1}, respectively. They are much closer to δ_{GC} from the present study. Calculating an average of all values of δ_{EC} determined using the MAAP and adjusting this average value to the PSAP wavelength of 550 nm assuming again an Angström exponent of -1, a value of 7.8 $m^2\,g^{-1}$ can be derived. This is about 40% smaller than the average value of all PSAP measurements, which cannot be explained by a wrong assumption of the Angström exponent. In comparison to the PSAP, the MAAP has a much smaller unit to unit variability between than 3 and 8% as shown in Section 3.2.1 and in Müller et al. (2011). More likely, large parts of this discrepancy are therefore due to the uncertainty of PSAP measurements. The reason for the uncertainty of the PSAP is mainly attributed to uncertainties in flow and spot size measurement (Müller et al., 2011). In addition, the conventional correction of PSAP data using the Bond-correction (Bond et al., 1999) is inadequate, when a large fraction of particles is non-absorbing (Müller et al., 2011).

4.3.4. Effects of the mixing state on the mass absorption coefficient

For the estimation of the soot mixing state and its effect on δ_{GC}, the microphysical optical model described in Section 3.4 was used. With this method, Episode III was more precisely investigated, since δ_{GC} showed the largest variability in this time period. To run this model, additional information about ambient and non-volatile particle number size distributions were used. In general, volatility measurements can be used to determine the fraction of low and high volatile particles (Wehner et al., 2009) as a function of their size and estimate the shell and core diameters, respectively (Cheng et al., 2009). Because a simplified version of such a measurement system was used in the present study, heating just the whole particle number size distribution, some assumptions had to be made. As a result of this model, the fraction of external mixed soot particles can be derived.

The time series of the external mixed fraction for three observation sites are shown in Figure 4.24. In addition, simulated values of σ_{ap} are shown for a completely internal and completely external mixed case. The measured absorption coefficient is almost entirely in the range whose lower and upper bounds are defined by the external and internal case, respectively. The external mixed soot fraction showed values around 60% at the urban site and around 50% at the regional sites in the polluted air mass (Episode III - c). After the air mass change in Episode III - m, the external mixed soot fraction increased to values around 90% at all 3 observation sites. In Figure 4.25, δ_{GC} in dependence on the external mixed soot fraction is shown. As can be seen, the highest mass absorption coefficients were observed when the external mixed soot fraction was lowest. Higher values of δ_{GC} in combination with a higher internal mixed soot fraction are

in agreement with theory and experimental findings, as mentioned in Section 4.3.3.

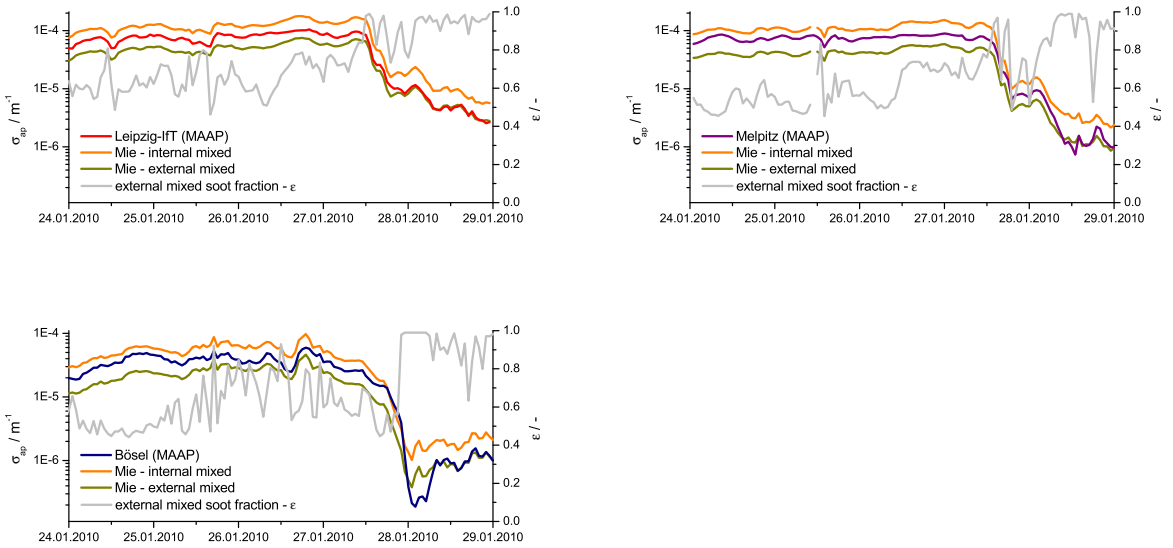

Figure 4.24.: *Comparison between time series of measured and calculated absorption coefficients (σ_{ap}) and model derived external mixed soot fraction (ϵ) for Leipzig-IfT, Melpitz and Bösel during Episode* III.

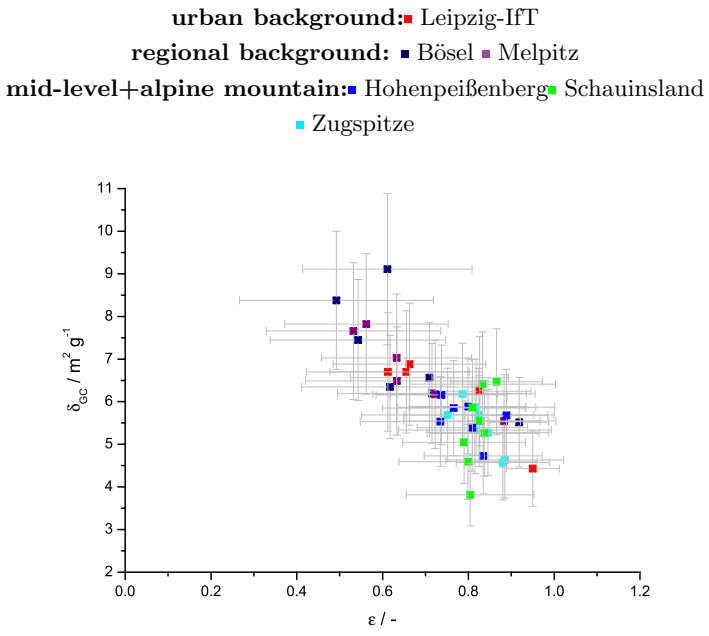

Figure 4.25.: *Comparison between measured daily averaged mass absorption coefficients (δ_{GC}) and calculated external mixed soot fractions (ϵ).*

5. Regional Modeling

5.1. Model validation against observations

In this section, the results of three model runs with slightly different settings and EC emission rates are considered, in order to perform a sensitivity study, especially on the simulation of BC. The settings for the first model run, designated as R1, are described in Section 3.5. The results of this initial run validation are summarized in Table 5.2. In the second simulation, designated as R2, the module that reads in the emission rates was slightly modified, so that all fine mode EC emissions could be read in. In addition the scaled EUCAARI EC emission inventory was used, as described in Section 3.5.3. The third model run, which is designated as R3 in the following, is designed as an emission sensitivity run, where the original EUCAARI EC emission inventory used in R1 was simply multiplied by a factor of 2, since global emissions estimates of EC may also vary by a factor of 0.5 - 2 (Vignati et al., 2010; Ramanathan and Carmichael, 2008) and a factor of 2 - 5 on regional scale (Ramanathan and Carmichael, 2008). Furthermore, the optical properties, especially the simulated absorption coefficient, will be validated. The ratio between BC mass and absorption is analyzed from a comparison of δ_{mod} and measured δ_{GC} during Episode I. The goodness of simulation of different model variables are evaluated in terms of mean bias (MB, Equation B.1), the mean normalized bias (MNB, Equation B.3) , the root mean square error (RMSE, Equation B.2) and the correlation coefficient (R, Equation B.4).

5.1.1. Meteorology

For the simulation of aerosol processing in the atmosphere it is essential that the meteorological conditions in terms of temperature, relative humidity and wind are well represented by the model. As a first step in model validation, the 4-dimensional meteorological variables calculated with R1 for the nested domain were compared to measurements from vertical soundings of the atmosphere, provided by the University of Wyoming[1]. The vertical profiles of 9 locations in Germany were extracted from model output of R1. They were compared to corresponding soundings in terms of parameters described in Appendix B.

In Figure 5.1, exemplary scatter plots between modeled and measured temperature, relative humidity and horizontal wind components at a height of 500 m a.s.l. at Lindenberg observation site are shown. The modeled and measured temperature is well correlated, but slightly underestimated by the model. From humidity comparison, it can be seen, that the model slightly overestimates the water vapor content in the 500 m model level with a moderate correlation of 0.67. The simulation of meridional and zonal wind components is good in comparison to

[1] http://weather.uwyo.edu/upperair/sounding.html

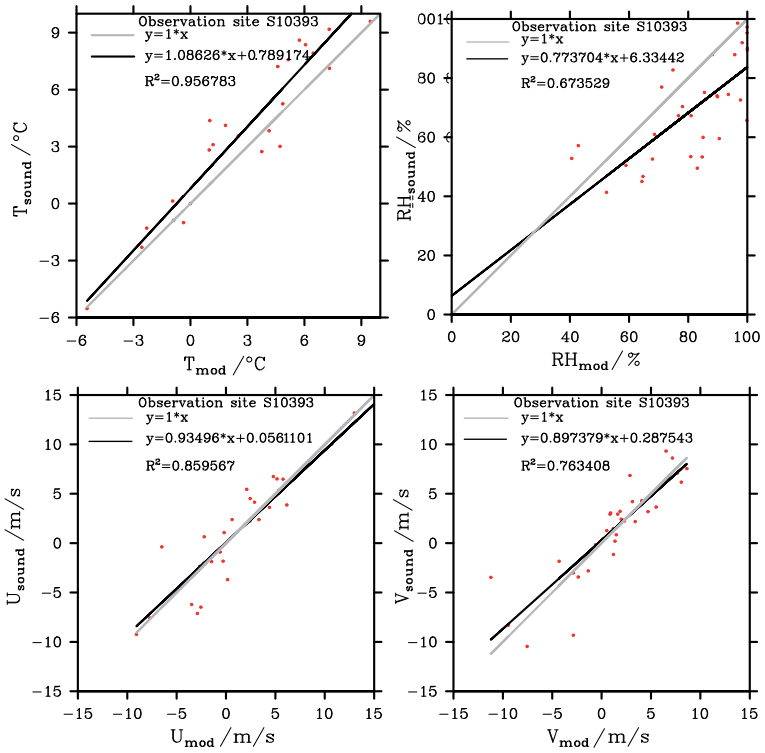

Figure 5.1.: *Comparison between measured and modeled temperature (T), relative humidity (RH) and wind x-y-components (U and V) for 500 m a.s.l at Lindenberg observation site (S10393) in the time period between March 24 to April 09, 2009.*

measurements, as can be seen from the regression lines. The average values of the validation metrics over all 9 sounding sites for different levels of the nested model domain are shown in Figure 5.2 and in Table 5.1. From the plot of the mean model bias it can be concluded that the simulated temperature is too low by around 1 °C in the lowest layers with increasing bias towards higher altitudes, whereas the correlations are getting better towards higher atmospheric levels. As mentioned before and confirmed by the comparison with other sites, the simulated humidity is too high below 1 km. Between 1 and 3 km, the humidity is too low. The correlations between model and measurements are only moderate at all levels under consideration. The zonal and meridional wind components are simulated too high in the lowest atmospheric levels, but especially the meridional component shows only a negligible deviation from measurements above 500 m. The correlations are mostly good and increase towards the free troposphere.

The aerosol dispersion in the atmosphere strongly depends on the stability conditions. An unstable atmosphere in the lowest layers leads to a well mixed planetary boundary layer, which is the case when solar insolation is highest. To analyze the stability of the atmosphere, the virtual potential temperature can be used. The potential temperature without humidity effects is defined as the temperature an air parcel would take on if it is led dry adiabatic from a specific level characterized by its pressure to a reference pressure. It makes temperatures in different atmospheric heights comparable to each other. When considering humidity effects, the virtual potential temperature can be defined as the dry potential temperature an air parcel has to take on, to have the same density as moist air. For saturated air it can be calculated following Stull (1988) and using potential temperature, water vapor saturation mixing ratio and liquid water

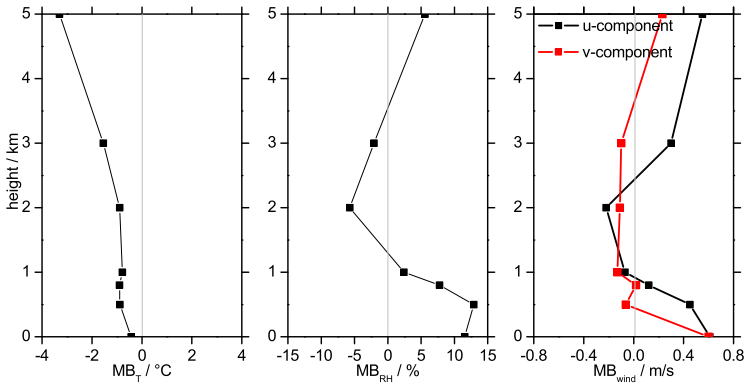

Figure 5.2.: *Mean Bias (MB) in temperature (T), relative humidity (RH) and wind x-y-components (U and V) as a function of height a.s.l. as average values over 9 sounding sites in the time period between March 24 to April 09, 2009.*

Level	T		RH		U		V	
	R	RMSE	R	RMSE	R	RMSE	R	RMSE
0	0.89	2.28	0.60	17.03	0.84	3.06	0.79	2.64
500	0.94	2.02	0.59	18.80	0.92	2.60	0.88	2.54
800	0.95	1.85	0.58	18.56	0.94	2.51	0.89	2.59
1000	0.96	1.73	0.61	18.06	0.93	2.63	0.91	2.40
2000	0.98	1.46	0.70	21.30	0.95	2.37	0.93	2.28
3000	0.98	1.90	0.72	21.38	0.94	2.64	0.94	2.47
5000	0.99	3.45	0.73	18.16	0.96	2.78	0.95	3.02

Table 5.1.: *Root mean square error (RMSE) and correlation coefficient (R) between model and measurement for temperature (T), relative humidity (RH) and wind x-y-components. RMSE and R are average values over all sounding sites in the time period between 24.03.2009 - 09.04.2009.*

mixing ratio. If the air is unsaturated, the liquid water mixing ratio becomes zero and only the water vapor mixing ratio is considered in the calculation. The vertical profile of the virtual potential temperature can be used to derive the stability in the atmosphere. If this quantity is decreasing with height, the atmosphere is locally unstable in this region. If it is constant, the atmosphere is stratified neutral in the appropriate region. An increasing virtual potential temperature is equivalent to a stable atmosphere. In Figure 5.3, the profiles of the vertical gradient of the virtual potential temperature (lapse rate) from model and soundings are shown. The lapse rate is negative in an unstable and positive in a stable atmosphere. It can be seen from Figure 5.3(a) that in the lowest levels up to 300 m the atmosphere is unstable to neutral at noon, and that the model correlates well with the measurement. It seems that the instability is slightly underestimated by the model. Above 300 m, the atmosphere is stable, and an overestimation of stability from model can be seen. At midnight (Figure 5.3(b)), the atmosphere becomes very stable below 300 m. Again, the model and the measurement correlate well. Only small changes in profiles can be seen above 300 m in comparison to the noon profiles. These results suggest that the vertical mixing of particles due to instability of the atmosphere could be somewhat underestimated by the model in lower atmospheric levels.

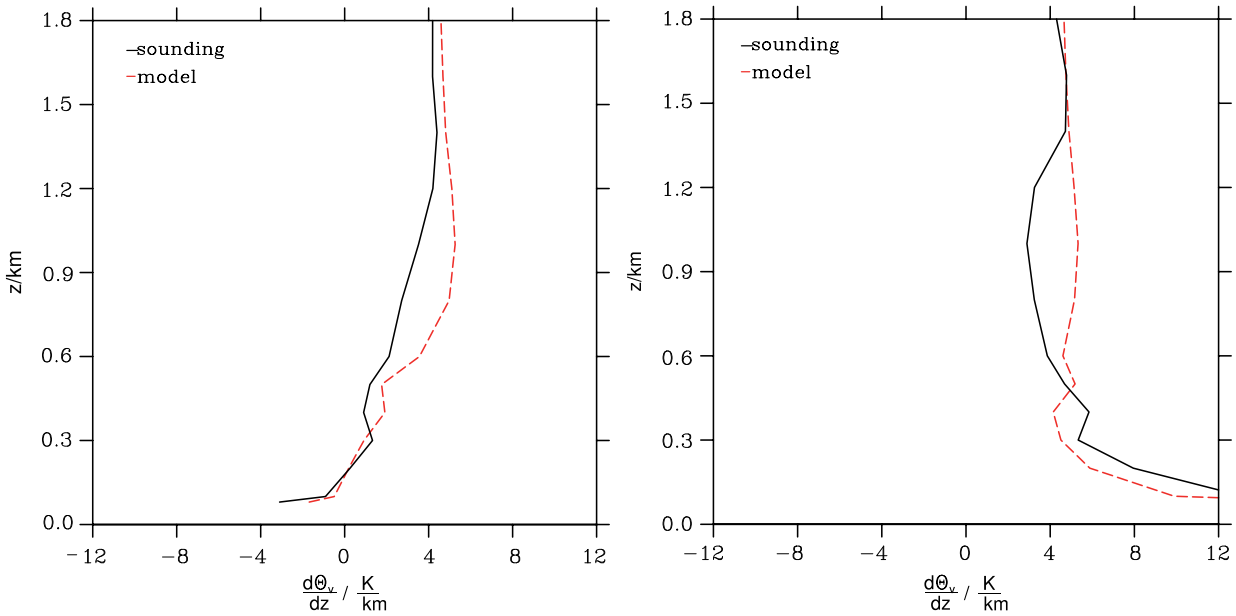

(a) At noon.

(b) At midnight.

Figure 5.3.: *Vertical profiles of lapse rates of the virtual potential temperature Θ_v as an average of model and sounding values at 9 observation sites in the time period between March 24 to April 09, 2009.*

5.1.2. Aerosol particles and gases

In a first validation step regarding aerosol particles, the simulated PM_{10} mass concentrations were compared to measurements using the initial run (R1) results for the time period under consideration. For this purpose, daily averaged PM_{10} mass concentrations measured by the UBA at 392 sites were considered. The observation sites are of various types with traffic to regional background characteristics. The results of this comparison in terms of MNB and R are shown in Figure 5.4. The values of MNB show a pattern in Germany, with an overestimation of PM_{10} in the western and northeastern part and an underestimation in the eastern and southeastern part. The range of MNB is between 1.33 and -0.52, which represents a maximum overestimation of 133% and a minimum underestimation of 52%. The reason for this pattern is unclear, but it suggests that there is possible over and underestimation of the emission rates of particulate matter, respectively. Since there was a significant air mass change from mostly marine to continentally influenced in this time period as described in Section 4.3.1, uncertainties in emission numbers in neighboring countries are also possible. Overall, the model slightly underestimates PM_{10} in Germany in the time period under consideration with MB of -6.1 $\mu g\,m^{-3}$, which corresponds to a value of MNB of -9%. The correlation coefficients between model and measurement are mostly good with R between 0.6 and 0.95 and show no such pattern. This confirms, in agreement with the previous section, that the meteorological conditions are simulated correctly in the whole modeled time period. When summarizing all pairs of modeled and measured PM_{10} concentrations, a correlation coefficient of 0.77 was found for Germany, as can be seen in Table 5.2.

The column integrated aerosol mass was qualitatively validated by a comparison of the column

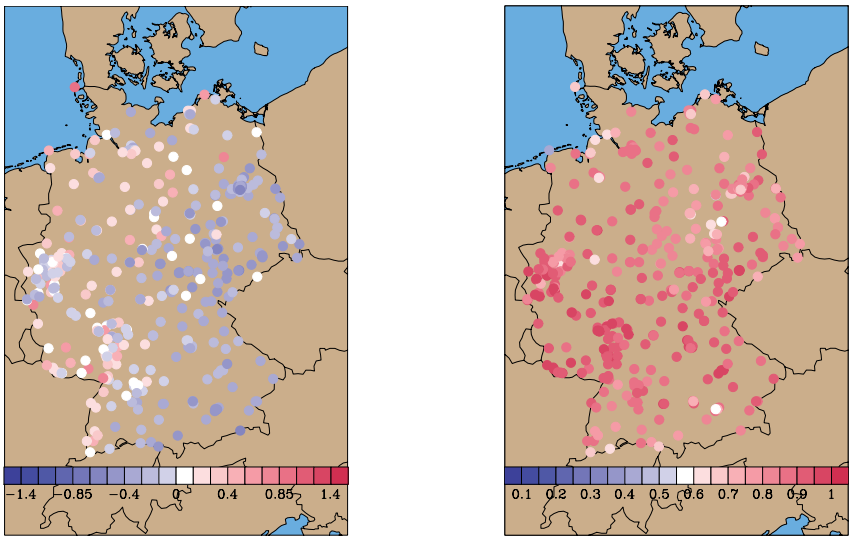

(a) Mean normalised bias. (b) Correlation coefficient.

Figure 5.4.: *Comparison between modeled and measured daily PM_{10} mass concentrations in the time period between 24.03.2009 and 09.04.2009. Measurements performed by the German Federal Environmental Agency.*

integrated aerosol optical thickness *AOT* from model and measurements. This can be done since, beside particle chemical composition and number size distribution, *AOT* is a function of the column integrated aerosol mass concentration (Kaufman and Fraser, 1983). The Moderate Resolution Imaging Spectroradiometer (MODIS) is an instrument that measures the spectral radiance in 36 channels aboard Aqua and Terra satellites. The reflectance data in three channels (0.47 ,0.66 and 2.12 μm) is used to derive the total spectral *AOT* (Levy et al., 2007). This data product was validated with Aerosol Robotic Network (AERONET) sun photometer measurements (Holben et al., 1998) in several studies, and it was found that MODIS *AOT* is often positively biased by up to 50 % (Schaap et al., 2008) and 48 % Remer et al. (2005) over the European land surface. This bias was attributed to uncertainties in land surface reflectance in the MODIS *AOT* retrieval and possible cloud contamination (Schaap et al., 2008).
In Figure 5.5 (a), the quotient between model *AOT* from summation over all model levels and MODIS *AOT* at 550 nm is shown. Since WRF calculates aerosol optical properties at only four wavelengths, as described in Section 3.5.1, linear interpolation between *AOT* at 400 and at 600 nm was used to derive the *AOT* at 550 nm. Because MODIS data is only available at specific times, *AOT* from WRF was only calculated for time periods when MODIS data was available. Average values are shown in Figure 5.5 (a). Most of the measurements are from the continental influenced air mass, because cloud free cases occurred more frequently during that time in Central Europe. Over most regions in Germany MNB is between -0.4 to 0.4. A positive Bias can be seen in the northeastern and southwestern part of Germany. When looking at MNB in PM_{10} in Figure 5.4, it becomes obvious that the largest values of MNB in Germany were also determined for the region in the southwestern part. Since this effect can not only be seen in the column but also at the surface, it is likely that this is due to uncertainties in emissions, which are maybe too high in this region. In eastern regions shown in Figure 5.5 (a), MNB in *AOT* is

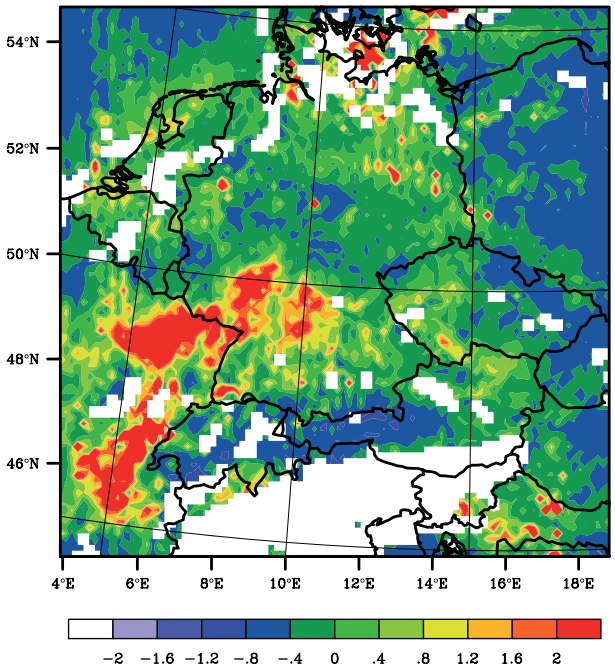

(a) Quotient between modeled and measured (MODIS) *AOT* (dimensionless).

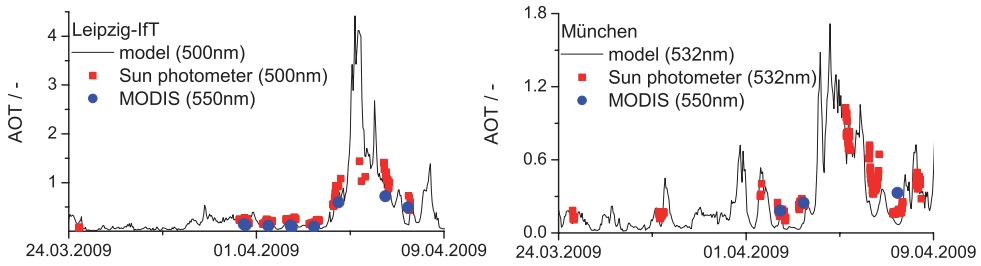

(b) Time series of *AOT* measured with a sun photometer at Munich and Leipzig-IfT and corresponding model values.

Figure 5.5.: *Comparison between modeled and measured aerosol optical thickness (AOT). Simulated values of AOT were considered for times and locations with available MODIS data.*

around -40 to -80%. In addition, the time series of modeled *AOT* was compared to AERONET sunphotometer measurements performed at two observation sites in Germany. The extracted MODIS *AOT* data at those locations is also shown (Figure 5.5 (b)). In spite there are only a few simultaneous measurements of MODIS and sunphotometer in the considered time period, *AOT* of both devices is nearly the same and shows a good correlation. This suggests that the MODIS data is unbiased concerning possible uncertainties in surface reflectance. Regarding only *AOT* of those two AERONET sites for comparison with model values, MNB was found to be 15% and the correlation is moderate with $R = 0.68$ (cf. Table 5.2). Nevertheless, there are large regions in the modeling domain D02, where *AOT* is not simulated correctly.

The modeled values of m_{BC} were compared to the values of m_{GC} measured by Raman spectroscopy and shown in Section 4.3.2. Measured mass concentrations were averaged to the maximum length of the sampling interval of 1 day, using weighting based on sampling time. For this comparison, the traffic site Leipzig-Eisenbahnstraße was not considered, since the model is

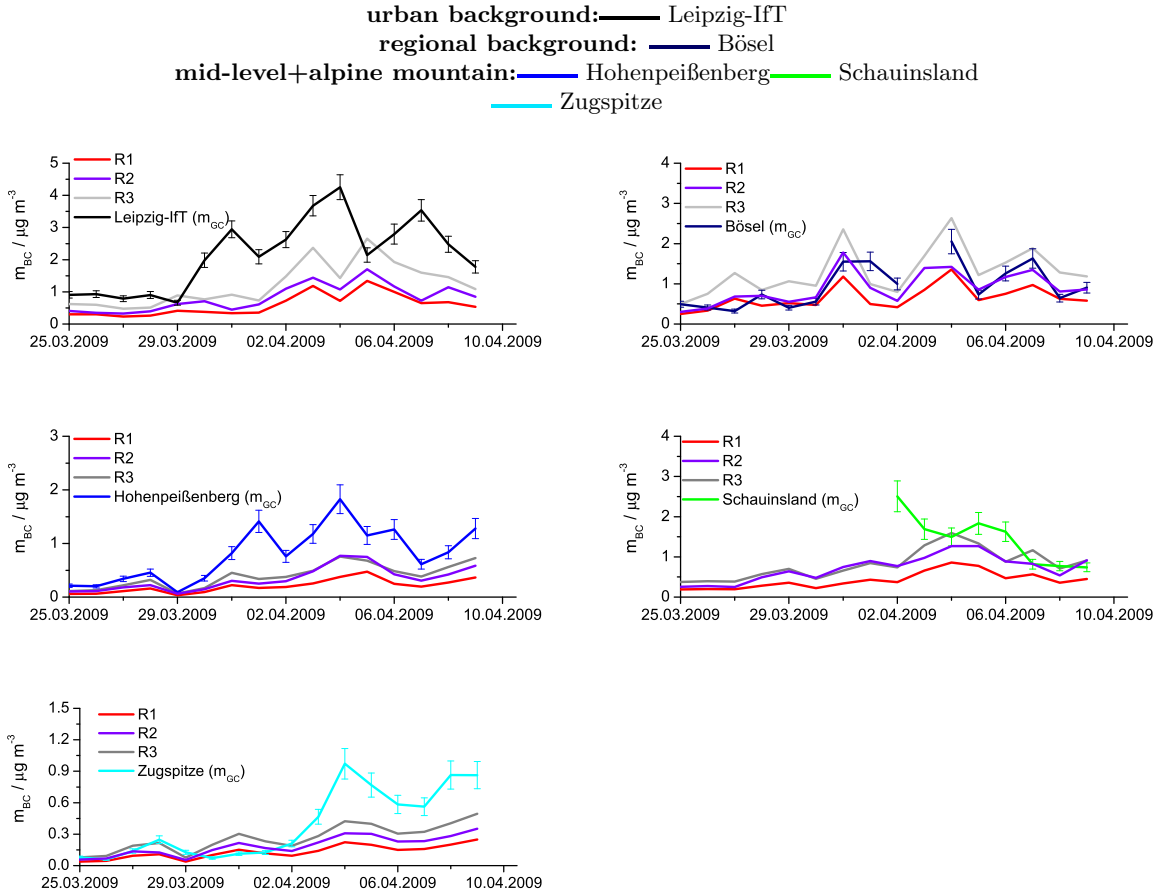

Figure 5.6.: *Comparison between measured and modeled soot mass concentrations.*

not capable to simulate such small-scale variability observed in this street canyon. The time series of 5 observation sites and corresponding model values are shown in Figure 5.6. The spatial distribution of MNB and R are shown in Figure 5.7. At the urban background site Leipzig-IfT, m_{GC} increased from 1 to a maximum of 4 $\mu g\,m^{-3}$ during this time period. This behavior can also be seen in the modeled values of m_{BC} for R1, but on a lower level. On average, the model underestimates m_{BC} by about 80% and the correlation is moderate (R=0.55). At the regional site, the temporal behavior as well as the magnitude of m_{BC} are much better reproduced by the model with R around 0.7 and MNB around -30%. At the mid-level mountain sites, modeled m_{BC} again correlates good with measurements at least at Mt. Hohenpeißenberg, but is also negatively biased with MNB between -50% and -80% . Even at the alpine mountain site, m_{BC} is well correlated, but also shows a substantial negative bias. Calculating the overall deviation of the model, m_{BC} is about 0.71 $\mu g\,m^{-3}$ to low, which corresponds to MNB of -53 % and R is 0.59. In a recently published modeling study by Tuccella et al. (2012) applying WRF-chem over Europe, it was found that the carbonaceous aerosol fraction contributes most to the error in $PM_{2.5}$ simulation. They found, that modeled m_{BC} is negatively biased by about 51%, comparing model values with chemical m_{EC} measurements at 4 stations from EMEP from the whole year 2007. This value is close to our findings, although only a comparable short time period, another determination method for soot and a different EC/OC emission inventory was used. Because of this large negative bias found for the simulation m_{BC}, the model performance re-

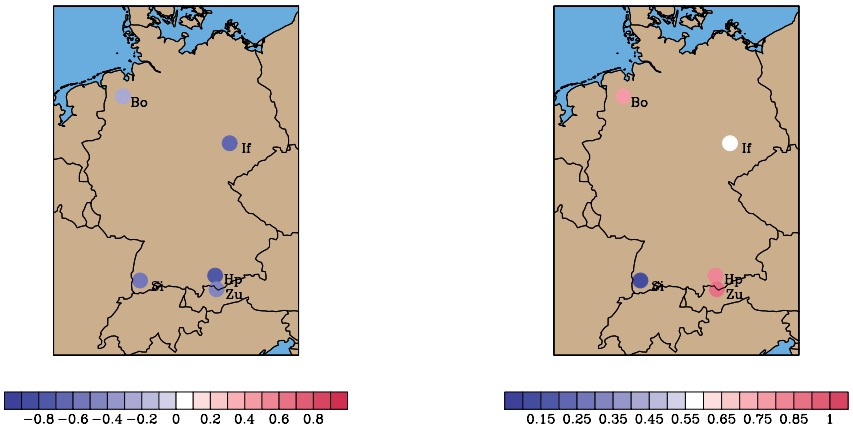

(a) Mean normalised Bias, run with EUCAARI EC emissions (R1).

(b) Correlation Coeffcient, run with EUCAARI EC emissions (R1).

Figure 5.7.: *Comparison between modeled and measured soot mass concentrations at GUAN sites Leipzig-IfT (If), Bösel (Bo), Hohenpeißenberg (Hp), Schauinsland (Si) and Zugspitze (Zu). Model values of BC mass concentration are compared to measurements of GC mass concentrations.*

garding gaseous combustion products was checked. Therefore, the volume mixing ratios of SO_2 and CO from hourly measurements of the UBA network were compared to corresponding R1 model values. The resulting time series are shown in Figure 5.8. In general, an increase of the SO_2 volume mixing ratio can be seen when the continental air mass was established in Central Europe as previously found for m_{GC}. This can be seen especially for the values measured at the regional site in Melpitz. When comparing with model values, the SO_2 volume mixing ratios show a very similar temporal behavior. During some events with higher values, the model seems to overestimate the SO_2 volume mixing ratio. At the mountain site Schauinsland the correlation is not good. Nevertheless, the measured and modeled values have the same magnitude, except for some shorter time periods. Summarizing all measurements and corresponding model values, the MNB shows an overestimation of around 83% with a poor correlation of $R = 0.40$. Comparing this to findings by Tuccella et al. (2012), they found a nearly double positive model bias of about 166%, but included much more observation sites in their analysis.

The CO mixing ratios show a less pronounced increase in the continental air mass at both stations under consideration (e.g. Figure 5.8 (b)). At both, the regional and the mountain observation site, modeled and measured values show a similar temporal behavior with an overall correlation coefficient of 0.60. A substantial negative bias of 61% is obvious at both stations, which is very similar to the bias found for m_{BC} and therefore suggests that emissions from combustion processes may be underestimated. All values of MNB and R, mentioned above, are shown in Table 5.2.

In summary, it can be stated, that the overall simulation of PM_{10} is good, although the values are too low in the eastern part and too high in the southwestern part of Germany. This somehow reflects to a certain extent in the simulation of AOT, which is also too low, especially in the regions to the east of Germany. BC is substantially underestimated by the model, which is also true for the gaseous combustion product CO.

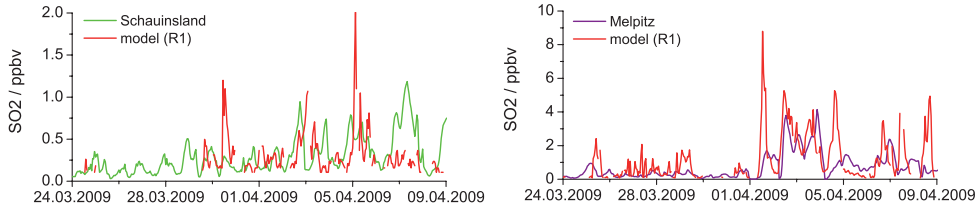

(a) SO_2 volume mixing ratios at Melpitz and Schauinsland.

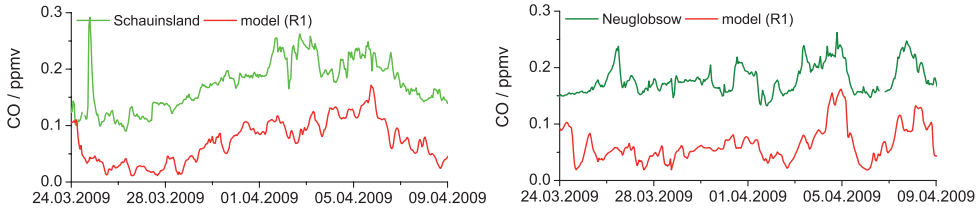

(b) CO volume mixing ratios at Neuglobsow and Schauinsland.

Figure 5.8.: *Time series of modeled and measured volume mixing ratios of atmospheric gases.*

5.1.3. Absorption coefficient

Aerosol optical properties such as extinction coefficient, single scattering albedo and asymmetry factor are determined in WRF using the Mie-theory as described in Sections 3.5.1 and 3.5.4. Using output variables of σ_{ext} and SSA at 600 and 1000 nm and Equation 2.10, the absorption coefficient at 637 nm can be derived from the model output by using linear interpolation. The absorption coefficient at this wavelength is desired since the MAAP, which is applied in this study, uses this wavelength as described in 3.2.1. All measurements were performed for dry aerosols, which is a problem when comparing with the modeled absorption coefficient, since simulated values are derived for wet particles. In several studies it was shown that soot, internally mixed with hydrophilic substances, (e.g. sulfate) is able to take up water, which then amplifies the absorption of solar radiation (Fuller et al., 1999; Nessler et al., 2005; Mikhailov et al., 2006). For that reason, the optical properties were calculated again, after the R1 model run was finished, using an offline version of the module 'optical_averaging' in WRF-Chem and the simulated concentrations of the chemical constituents as described in Section 3.5.4. For this offline run of the optical module, the aerosol water content was removed.

In Figure 5.9, the modeled and measured hourly values of the dry σ_{ap} are shown for 7 observation sites with urban, regional and mountain characteristics. An increase of σ_{ap} occurred in association with an increase in BC mass concentration during this episode, as shown before in Section 4.3.1. Regarding the urban sites, the increase is clearly visible in model values, at least for Leipzig-IfT. The model underestimates σ_{ap}, especially for the station in Augsburg. MNB is between -30% and -70% with values of R between 0.4 and 0.5. At the regional sites, the model simulates the absorption coefficient well, so that even some peak values are reflected in the model output. In addition, the correlation is better than at urban sites with values of R between 0.55 and 0.65, but in the entire period the model is positively biased with MNB around 60%. At the mid-level mountain sites the model is again on the level of measured σ_{ap}, except some shorter time periods in the beginning of April at Mt. Hohenpeißenberg. The values of MNB are between -30% and 30% with correlation coefficients between 0.2 and 0.6. Surprisingly, the best

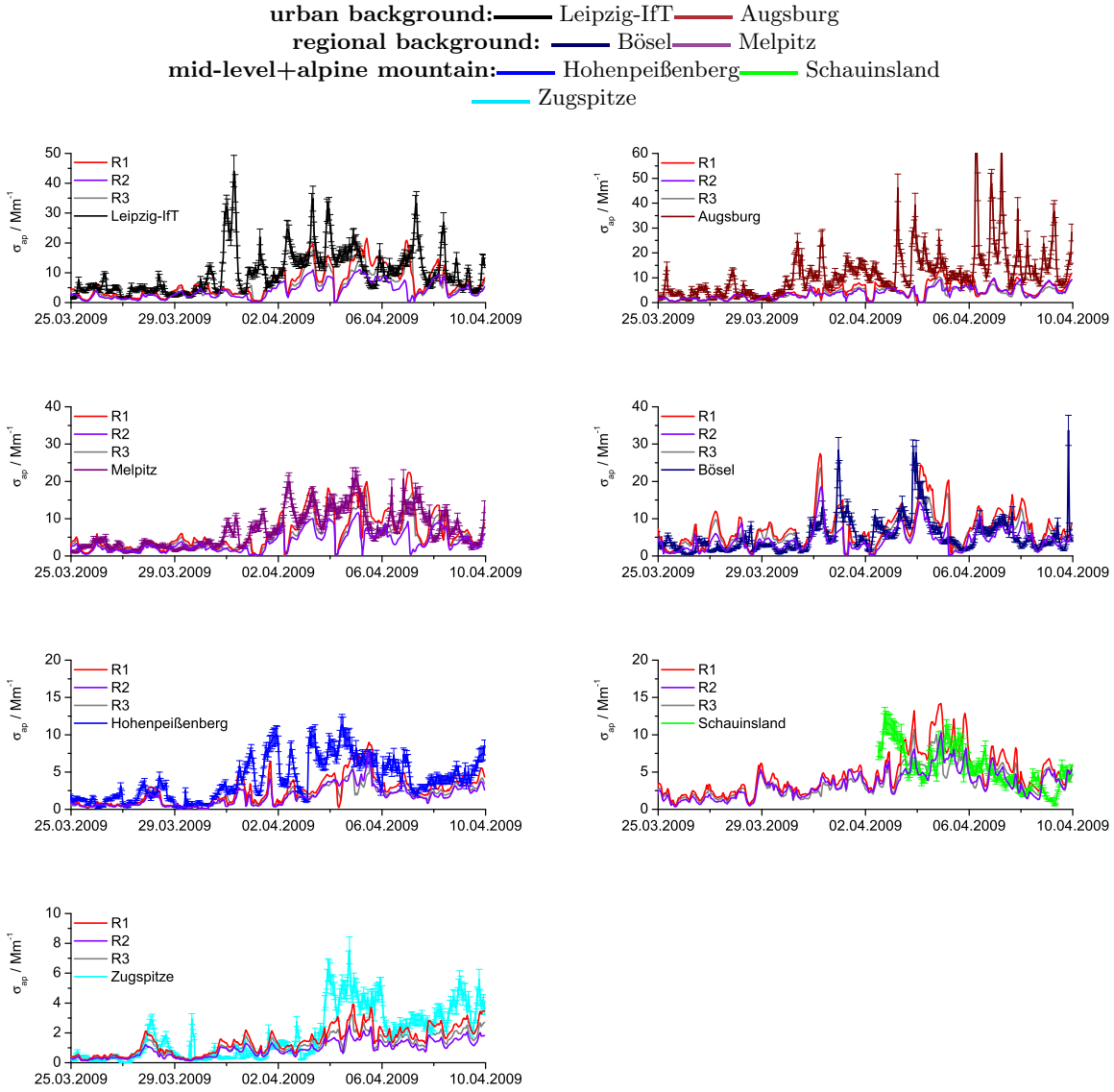

Figure 5.9.: *Comparison between measured and modeled absorption coeffcient (σ_{ap}).*

correlation between model and measurement is found for the alpine mountain site Zugspitze, with R= 0.7 and a small positive bias around 45%. In summary, a value of $MNB = 20\%$ was found as an average over all sites (cf. Table 5.2). The overall correlation coefficient was 0.43. If the water is not eliminated before the optical calculation, as it is usually the case, the MNB is nearly doubled (34%) , whereas the correlation remains unchanged.

Summarizing the findings of this section and the section before, simulated m_{BC} is too low and σ_{ap} is overall too high. Calculating the quotient of both following Equation 2.11, the dry modeled mass absorption coefficient at 637 nm designated as δ_{mod} can be derived. It can, in turn, be compared to the values presented for Episode I in Section 4.3.2. In Figure 5.11 the time series of daily averaged δ_{mod} for the R1 model run and the measurements of δ_{GC} are shown for 5 stations. As determined from measurements, δ_{GC} shows only little variation during this time period with values between 3 and 6 $m^2 g^{-1}$, which is on the same level at all observation sites ranging from urban to mountain characteristics. When looking at the model values a similar behavior can

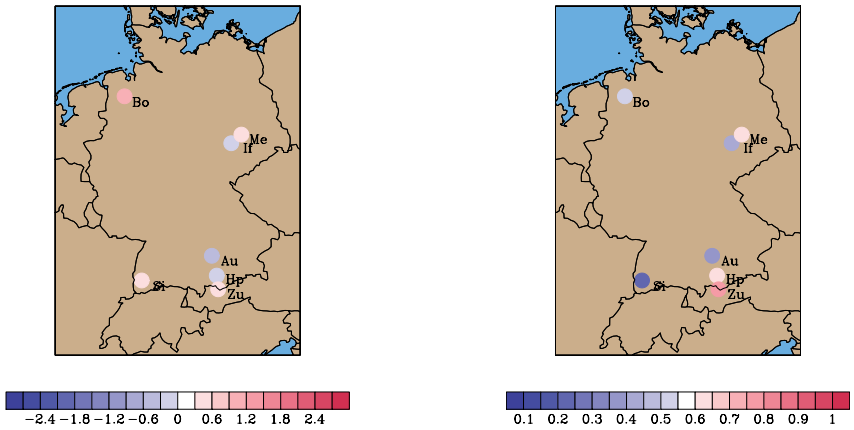

(a) Mean fractional Bias, run with double EC emissions.

(b) Correlation Coeffcient, run with double EC emissions.

Figure 5.10.: *Comparison between modeled and measured absorption coefficients at GUAN sites Leipzig-IfT (If), Bösel (Bo), Hohenpeißenberg (Hp), Schauinsland (Si) and Zugspitze (Zu).*

be seen. It has to be pointed out, that δ_{mod} is higher with values around 9 and 12 $\mathrm{m^2 g^{-1}}$. The overall MNB is 111%, which is equivalent to a mean bias of 5.34 $\mathrm{m^2 g^{-1}}$. Regarding humidified particles, MNB is even higher (133%) (cf. Table 5.2). This means that the model error in the simulation of m_{BC} is (over)compensated by a too large δ_{mod}, so that the simulated absorption behavior of particles is nearly right or even too pronounced. It must be mentioned, that interestingly the range of modeled values is close to the range of δ_{EC} given in Table 4.2 from the studies using the PSAP.

5.2. Sensitivity study on BC and optical adjustment

The simulated BC mass concentration strongly depends on the emissions of this species, because BC is a primary pollutant which has no secondary source. Once emitted into the atmosphere, it can be long-range transported because of its mostly hydrophobic nature, which impedes an incorporation into cloud droplets and subsequent rapid removal due to wet deposition (Heintzenberg, 1989). Nevertheless, the ability to uptake water and therefore the possible incorporation into cloud processes, may change due to coagulation or collision processes with more hygroscopic particles such as sulfuric acid (Ogren and Charlson, 1983). At the current state of the WRF development, the model is not capable to simulate the state of mixture of BC, and thus it is assumed that all chemical constituents are internally mixed (Chapman et al., 2009) in each bin. It may lead to an overestimation of the hygroscopic growth in the model and therefore an overestimation of the simulated dry and wet deposition as important removal processes(Ducret and Cachier, 1992), especially in near source regions. Since precipitation processes were of minor importance in the simulated period, especially during Episode I - c as shown in Section 4.3.1, it is assumed that the simulated m_{BC} is most sensitive to changes in EC emission rates.
Simulations were repeated with modified EC emission inventories. In order to match the simulated BC mass concentrations, 2 additional runs with modified emission rates (R2 and R3) were performed. According to Sections 3.5.3, original EUCAARI emissions from 2005 (used in R1)

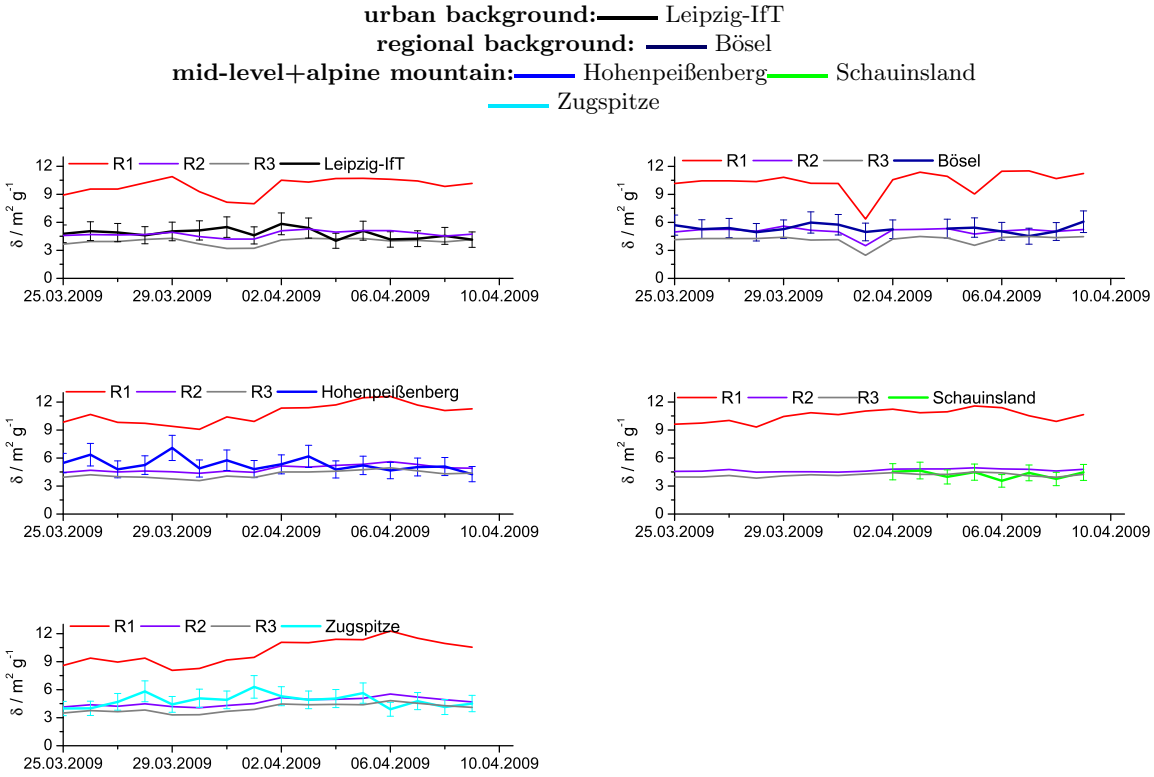

Figure 5.11.: *Comparison between measured (δ_{GC}) and modeled (δ_{mod}) mass absorption coefficients.*

were scaled to ARCTAS emissions from 2008 to account for the emission migration since 2005. For R3, EUCAARI emission rates were simply doubled. The simulated aerosol microphysical and optical properties were again compared to measurements in terms of MB, MNB, $RMSE$ and R. The resulting time series of m_{BC} for R2 and R3 are shown in Figure 5.6 and validation metrics are summarized in Table 5.3. In general, an increase of simulated m_{BC} towards the measured values can be seen at all observation sites and for both additional runs. At the urban background site in the eastern part of the modeling domain, the simulation of BC shows only a minor change for R2 in comparison to R1. If doubled EC emissions are used, a considerable improvement could be achieved. The difference between BC from R1 and R2 at the regional site is more pronounced, where the modeled values of R2 are on the same level as the measurements and the correlations are still very good. However, using R3 BC mass concentrations are overestimated. For the mid-level mountain sites m_{BC} from R2 and R3 is nearly the same but still too low especially at Mt. Hohenpeißenberg. For Mt. Zugspitze, using R2 leads to lower values of m_{BC} than for R3, but for both runs the simulated values are too low. Summarizing the results of this comparison, the simulation of BC is improved with MNB -36% for R2 and -6% for R3, whereas the simulation of the pattern remains nearly unchanged with R= 0.59 for R2 and R= 0.61 for R3. In addition, increasing the EC emissions, leads to a slight improvement of the PM_{10} simulation with MNB changed to 7% and -6%, respectively. Also the column aerosol mass seems to be improved, since the deviation between modeled and measured AOT is smaller for both, MODIS and sunphotometer comparison.

For adjusting the modeled to the measured absorption behavior, the imaginary part of the BC

Class	Model variable	Number of sites	MB	MNB	$RMSE$	R
Meteorology	T	9	-1.27[1]	-0.06	2.39[1]	0.99
	U	9	0.16[2]	0.37	2.92[2]	0.96
	V	9	0.13[2]	0.32	2.84[2]	0.95
	RH	9	4.83[3]	0.6	17.81[3]	0.85
Gases	SO_2	5	0.10[4]	0.83	0.86[4]	0.40
	CO	2	-0.10[5]	-0.61	0.11[5]	0.60
Aerosol	PM_{10}	392	-6.10[6]	-0.09	14.67[6]	0.77
	BC	5	-0.71[6]	-0.53	1.07[6]	0.59
Aerosol optics	AOT[7]	2/2	-0.02/0.15[8]	-0.04/0.13	0.03/0.51[8]	0.78/0.68
	σ_{ap-wet}	7	-1.07[9]	0.34	37.63[9]	0.41
	σ_{ap-dry}	7	-1.57[9]	0.2	36.73[9]	0.43
	$\delta_{mod-wet}$	5	6.42[10]	01.33	42.54[10]	-0.10
	$\delta_{mod-dry}$	5	5.34[10]	01.11	30.35[10]	-0.11

[1] Unit of temperature T is $^{\circ}C$
[2] Unit of wind speed is $\mathrm{m\,s^{-1}}$
[3] Unit of relative humidity is %
[4] Unit of volume mixing ratio is ppbv
[5] Unit of volume mixing ratio is ppmv
[6] Unit of mass concentration is $\mu\mathrm{g\,m^{-3}}$
[7] Measasurements from MODIS/Sunphotometer
[8] dimensionless
[9] Unit of absorption coefficient is $\mathrm{Mm^{-1}}$
[10] Unit of mass absorption coefficient is $\mathrm{m^2\,g^{-1}}$

Table 5.2.: *Summary of values of mean bias (MB), mean normalised bias (MNB), root mean square error ($RMSE$) and correlation coefficient (R) derived from a comparison of different measurements and corresponding model values simulated in the base run (R1).*

complex refractive index was varied, as described in Section 3.5.4. δ_{mod} was chosen because, as an intensive property, it is independent of the aerosol mass. In addition, it accounts for the mixing state information, as already discussed in Section 4.3.4. The method was applied using the simulated mass concentrations of all chemical constituents of the base run R1. The derived time series of the adjusted imaginary part is shown in Figure 5.12. The imaginary part shows only small variations, indicating that the constancy of δ_{mod} is well represented by the model as already shown in the section before. Therefore, an average value of 0.26 was derived, which is much smaller than the commonly used value from Bond and Bergstrom (2006) of 0.71. In this review paper, refractive indices from many other studies are summarized. They found that most of them lie on a line in a plot, where the real part of the refractive index of atmospheric soot is on the x-axis and the imaginary part is on the y-axis. They argued that soot has a single refractive index, and this variation is due to a change in the void fraction in the soot particles. The value found by the adjustment procedure is outside the range given by Bond and Bergstrom (2006) for atmospheric soot particles.

To further examine the possible reason for the discrepancy between the adjusted and commonly used imaginary part of BC refractive index, a simplified procedure in comparison to WRF for estimating aerosol absorption coefficient by Mie-theory was applied. The first simplification is the usage of only two chemical constituents, i.e. BC and the non absorbing part of atmospheric aerosols. Both constituents are characterized by there complex refractive index of $1.85+0.71i$ for BC and around $1.55+1\text{E-}7i$ as a typical value for the non-absorbing part of atmospheric par-

ticles. The particle number size-distributions are assumed to be a decomposition of log-normal functions, given in Equation 2.5. Soot is assumed to have an average geometric diameter of 100 nm and a geometric standard deviation of 1.9. Non-absorbing particles are represented by a log-normal distribution with a geometric diameter of 200 nm and a geometric standard deviation of 2. This means that the aerosols are distributed almost entirely in the Aitken and Accumulation size range. When using the particle volume of both constituents in each bin, the refractive index of the effective medium as a function of the particle size can be derived by volume averaging as described in Section 2.3.1. This mixing rule is also applied in the particle optics module in WRF-chem. Passing this information to the Mie-code for spheres provided by Bohren and Huffman (1983), the efficiency factors for absorption can be derived. Integrating them over the sum of all particles using Equation 2.9, the absorption coefficient can be derived. Using further the density of $1.8\,\mathrm{g\,cm^{-3}}$, as it is used in WRF, δ_{mod} can be derived. For the settings described above, a value of $11.2\,\mathrm{m^2\,g^{-1}}$ was calculated, which is in the range of values that are typical for the base run (R1) as can be seen from Figure 5.11. When the imaginary part of complex refractive index is changed to 0.26, which is the value derived from the adjustment procedure, a value of $4.4\,\mathrm{m^2\,g^{-1}}$ is calculated. This is in the range of measured values as well as values derived for the simulations R2 and R3, where the adjusted imaginary part is also used as can be seen from Figure 5.11. Assuming that none of the log-normally distributed BC particles are mixed with a non-absorbing particle and taking the original imaginary part of 0.71, a value of 3.8 $\mathrm{m^2\,g^{-1}}$ is calculated. This value is even lower than the measured values, although the imaginary part was used that led to values of δ_{mod} being more than 50% larger as in the internal mixed case. This strongly suggests that the low imaginary part of the BC refractive index from adjustment compensates for the missing consideration of the BC mixing state in the model. In contrast to the model assumption of a completely internal mixture, most of the BC should be externally mixed during Episode I. Nevertheless, this value was chosen since its usage leads to the smallest deviation between modeled and measured mass absorption coefficients.
As mentioned before for the runs R2 and R3, the adjusted imaginary part of BC refractive index was used. From Figure 5.9 it can be seen that this leads to a slight decrease of modeled absorption coefficients at all 7 sites under consideration. Especially for R3, the overall MNB is improved with a value of -2% as can be seen from Table 5.3. The overall pattern remains almost the same since the correlation coefficient only slightly increased from 0.43 to 0.47 for R2 and 0.45 for R3, respectively. Summarizing the effects of mass improvement and adjustment of the absorption behavior on the comparison between model and measurements, it can be stated that the smallest deviation between model and measurement concerning most of the variables mentioned before, are derived by using R3.

5.3. Radiative forcing of soot particles

The effect of BC on the radiation balance at the surface and at TOA was examined by comparing the net irradiances from R3 and an additional unperturbed model run with no anthropogenic and natural EC emissions. The radiative forcing at the surface can be calculated using Equation 2.13. At TOA, the radiative forcing was also evaluated using Equation 2.14. These calculations were repeated for R3, but using the unmodified imaginary part of BC refractive index, in order

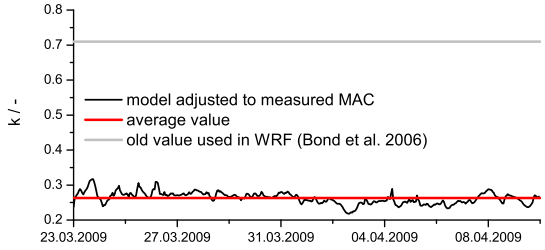

Figure 5.12.: *Times series of adjusted imaginary part of model complex refractive index of BC (k).*

Class	Model variable	Number of sites	MB	MNB	$RMSE$	R
Aerosol	$PM10$	392 / 392	-2.4 / -5.35	0.07 / -0.06	13.71 / 14.24	0.76 / 0.78
	BC	5 / 5	-0.56 / -0.3	-0.36 / -0.06	0.83 / 0.54	0.59 / 0.61
Aerosol optics	AOT_{MODIS}	2 / 2	-0.03 / -0.03	-0.03 / -0.01	0.03 / 0.02	0.75 / 0.74
	AOT_{Sunph}	2 / 2	0.10 / 0.11	0.04 / 0.07	0.32 / 0.43	0.71 / 0.67
	σ_{ap-dry}	7 / 7	-3.23 / -2.51	-0.23 / -0.04	40.89 / 38.61	0.47 / 0.45
	$\delta_{mod-dry}$	5 / 5	-0.15 / -0.87	-0.01 / 0.16	0.58 / 1.39	-0.03 / -0.07

Table 5.3.: *Summary of values of mean bias (MB), mean normalised bias (MNB), root mean square error ($RMSE$) and correlation coefficient (R) derived from a comparison of different measurements and corresponding model values simulated in the runs R2 / R3.*

to estimate the effect of the adjusted absorption behavior on the radiative forcing. For the evaluation of the radiative forcing, grid cells containing cloud ice or water were not considered. In Figure 5.13, the temporal evolution of the vertical cross section of the cloud-fraction as well as the modeled and measured incoming solar radiation at the surface is shown. As can be seen, there are two days in the beginning of April, which were simulated almost completely cloud free. Comparing the modeled and measured incoming solar radiations, an undisturbed diurnal cycle can be seen in both days. The temporal evolution of the radiative forcing at the surface and at TOA for April 03, 2009 in the nested model domain is shown in Figure 5.14 for both model runs. In general, the BC radiative forcing is negative at the surface and positive at TOA. The absolute value is higher at the surface than at TOA, which is in agreement with previous studies (Haywood and Shine, 1997; Ramanathan and Carmichael, 2008). For R3 it can be seen that the BC radiative forcing at the surface is mostly between -2 and -10 $\mathrm{W\,m^{-2}}$ in large parts of the model domain. For the same concentrations the radiative forcing at the surface using the unmodified imaginary part of BC refractive index is higher with values between -4 and -16 $\mathrm{W\,m^{-2}}$. In some grid cells the values may be even higher especially when large point sources are situated in immediate vicinity as can be seen for example in combination with Figure 3.5 in the northwestern part of the Czech Republic. The radiative forcing for R3 at TOA is comparably small with values mostly between 0 and 4 $\mathrm{W\,m^{-2}}$. Using the unmodified BC refractive index, values between 2 and 6 $\mathrm{W\,m^{-2}}$ were determined. In comparison to the globally and annually averaged values at TOA as summarized by the ICCP, the regional radiative forcing in Europe

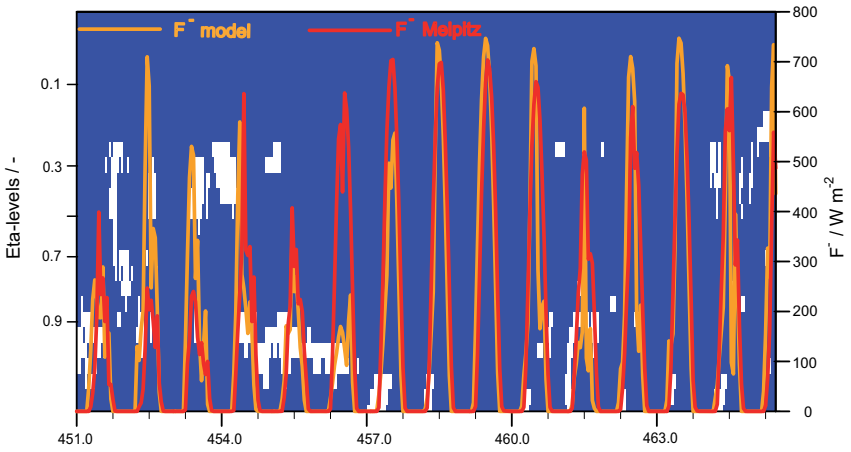

Figure 5.13.: *Time series in days since January 01, 2008 of measured and modelled incoming solar radiation (F^-) and vertical cross section of cloud fractions for Melpitz.*

may be considerably larger.

The local radiative forcing extracted from Figure 5.14 for 2 GUAN measurement sites is shown in Figure 5.15. In addition, the reduction in forcing at the surface and at TOA, when using the adjusted imaginary part of BC refractive index in comparison to the unmodified value is shown. In Waldhof for example, the maximum radiative forcing at the surface is -7 W m^{-2} for the unmodified imaginary part and around -3.5 W m^{-2} for the new settings. This corresponds to a lowering in radiative forcing of around 50%. At TOA the radiative forcing is even more decreased with values around 65 %. Taking also the values for Leipzig-IfT into account, the decrease in radiative forcing at TOA and the surface is mostly between 30 and 70 %.

The starting point for the modeling study presented in this chapter, were measurements of the absorption coefficient and the subsequently determined GC mass concentrations applying the new Raman-method for different measurement sites of the GUAN network. Using these measurements, reliable values of the mass absorption coefficient were experimentally determined as described in Sections 4.3.2. This offered the opportunity to validate WRF-Chem concerning the simulation of BC mass concentrations and the corresponding light absorption coefficients for a certain episode (cf. Episode I, Section 4.3.1). It was found that the model in average underestimates the BC mass concentrations, but slightly overestimates the absorption coefficient. Comparing measured and modeled mass absorption coefficients, a model bias of 111 % was found. However, after reasonable adjustment of the simulated BC to measured GC mass concentrations by modifying emission rates, the simulation could be improved. The results of the present work strongly suggest that conventional emission inventories of BC need to be up-scaled. This finding is emphasized by the results presented in Tuccella et al. (2012), that BC from their model calculations was similarly biased.

The simulation of the absorption coefficient could be improved by adjusting the modeled to the measured mass absorption coefficients, modifying the imaginary part of the BC refractive index. The very low value of 0.26 that was found by the adjustment procedure, can be explained

as a compensation for the missing treatment of the BC mixing state in the model. Jacobson (2001) pointed out, that the BC radiative forcing strongly depends on its mixing state, by explicitely simulating the aging of BC due to processes like coagulation and condensation. The calculations confirmed that due to aging a certain fraction of the BC particles become internally mixed. In this case the forcing is much higher as for the case when all BC particles are treated externally mixed. In the present study it was shown with the aid of real measurements of δ_{GC} as an indirect measure for the mixing state, that treating all particles internally mixed as it is done in the current version of WRF-Chem leads to an overestimation of the radiative forcing at the surface and at TOA between 30 and 70 %. Lowering the absorption of solar radiation by soot particles leads to a decrease in emission of thermal radiation after the absorption process and thereby reduces the heating of their environment. Consequently, adjusting the absorption behaviour to real measurements leads to a significantly lower effect of soot particles on the radiation balance and further reduces their semi-direct effect at least on regional scale. The results clearly show that the BC mixing state has to be accounted for in regional models, so that an externally mixed fraction of BC may coexist. Recent attempts simulate the mixing state by using a 2 dimensional representation of particle size distributions in box models (Oshima et al., 2009). In this 2 dimensional representation, particles of one size class may have varying mass fractions of BC. Condensation and evaporation processes lead to a growth or a shrinkage and therefore to a shift of the particles between the size classes and BC mass fractions. A more realistic but computational expensive approach was presented by Riemer et al. (2009), explicitly simulating the state of mixture of individual particles in a moving volume along a trajectory. The size of individual particles may change by condensation and evaporation. Particles may be added or removed by emission and coagulation, respectively.

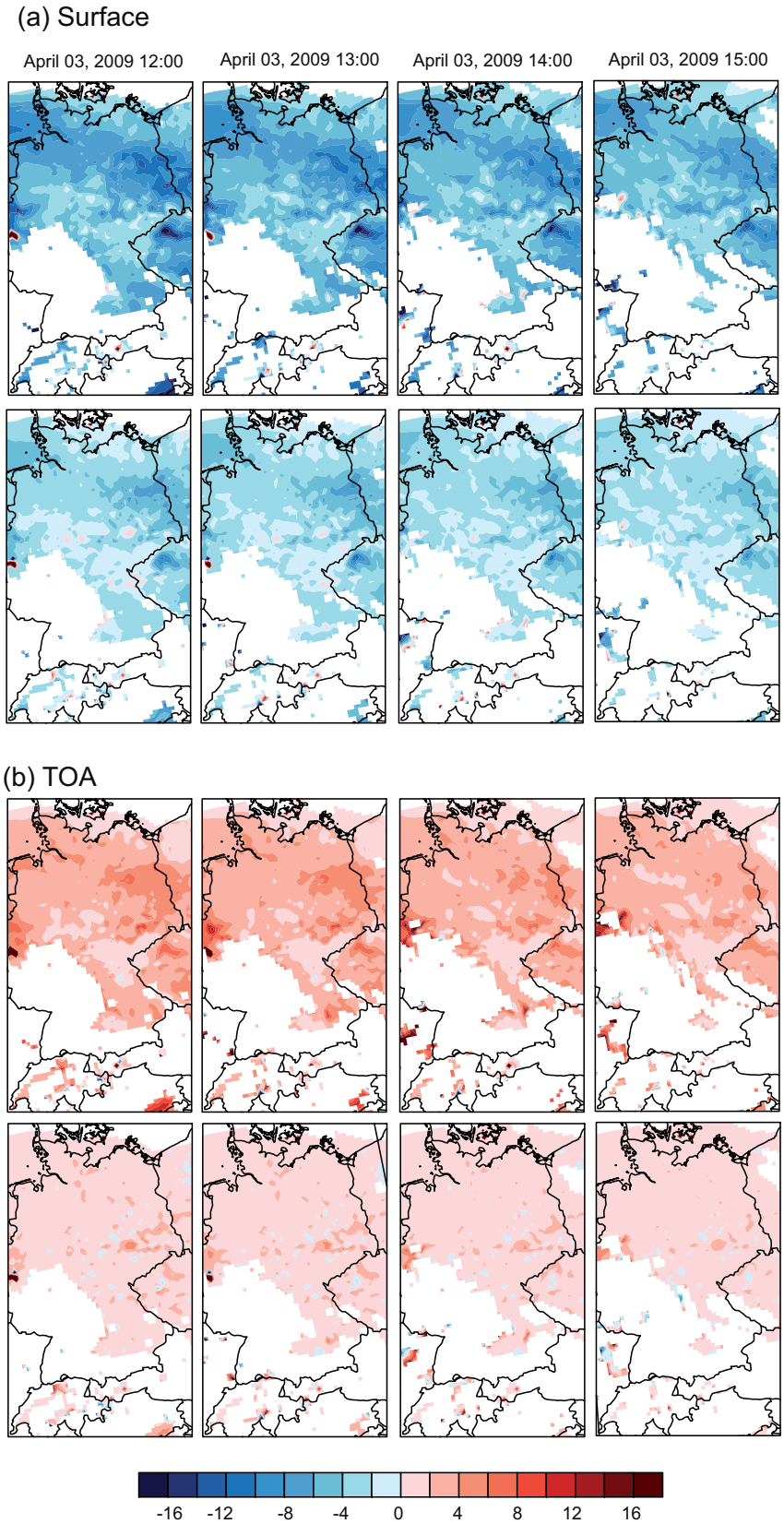

Figure 5.14.: *Direct radiative forcing in $W m^{-2}$ (time period: April 03, 2009 12:00 - 15:00) of BC at (a) the surface and (b) the top of the atmosphere, derived from the comparison of the runs with and without EC emissions. In (a) and (b) the upper panels refer to the run R3 using the unmodified imaginary part of BC in each case, whereas for the lower panels the adjusted value of 0.26 was used.*

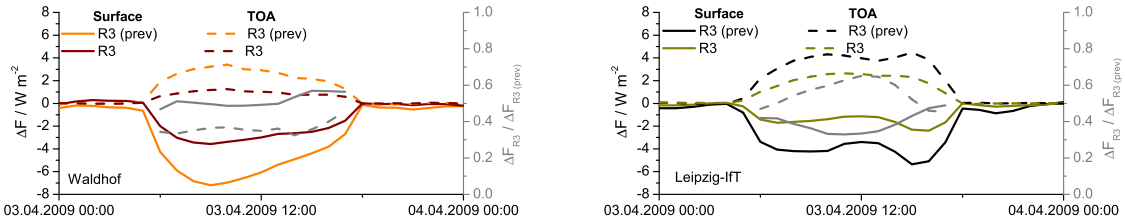

Figure 5.15.: *Local direct radiative forcing and ratio between radiative forcings for the runs with adjusted imaginary part of BC refractive index (R3) and the run with the unmodified value (R3 (prev)). All values are from the cloud-free time period between April 03 and April 04, 2009.*

6. Conclusion

An atmospheric observation data set including 2 years of optical, microphysical and chemical aerosol properties in Central Europe was analyzed with regard to the absorptive characteristics and radiative forcing associated with soot particles. In this integrated approach, important aspects of soot particles regarding the concentration of black carbon (BC), graphitic carbon (GC) and elemental carbon (EC) were investigated. The term BC basically accounts for absorptive components of soot particles, which are particularly small graphitic domains also designated as GC. This refractory fraction of atmospheric soot particles evolves at a high temperature. Taking these conditions as fixed, the term EC can be defined. The relation between BC, GC and EC is not necessarily constant and depends predominantly on the conditions during the production of soot particles and their stage of aging in the atmosphere. The measurements were performed in the German Ultrafine Aerosol Network (GUAN), incorporating observations at mountain, regional, urban and traffic locations. The combination of measurement devices enabled a determination of the soot mass absorption coefficient as a very important quantity, since it accounts for the change in absorption of solar radiation per unit soot mass during atmospheric aging processes. This quantity is widely used in modeling studies to estimate the radiative forcing of soot particles. In the present work, the measured mass absorption coefficients were utilized to adjust the absorption behavior simulated by a regional model (Weather Research and Forecast model coupled with a chemical transport module, WRF-Chem) to real measurements and to finally improve the estimation of the radiative forcing of atmospheric soot particles.

Aerosol light absorption coefficients at a wavelength of 637 nm were measured by Multi Angle Absorption Photometers (MAAP), which sample particles on glass microfiber filter tape during measurement. In the first step, a new method was developed to subsequently analyze soot particles on these samples by Raman-spectroscopy, determining (GC) mass concentrations. A laboratory calibration established a solid relationship between the Raman-signal and the mass of GC in individual particle samples collected on MAAP glass microfiber filters. The reference material Printex®90 was intensively characterized in terms of size, structure and GC fraction in comparison to atmospheric soot particles, and deemed suitable for calibration. In the calibration experiment, the mass of Printex®90 on the calibration samples was determined gravimetrically, while corresponding Raman-signals of GC were recorded by a Raman-spectrometer. A linear relationship between gravimetric masses and corresponding GC Raman-signal was found. The absorption coefficient from MAAP can be combined with the mass concentration to derive a mass absorption coefficient concerning GC (δ_{GC}).

In the next step, a carefully selected set of particle filter samples covering 3 distinct episodes and of 6 different measurement sites were analyzed by applying the new Raman-method for δ_{GC}. The particular weather situations were selected according to the back trajectories and the heat content of the air masses. The samples could be further grouped into 5 distinct episodes for

which δ_{GC} was quantified by orthogonal regression analysis. The samples from two maritime and one continental influenced summer period and one maritime and one continental influenced winter period were measured. Using the new Raman-method for measuring the GC content in selected particle samples, a unique data set of δ_{GC} was achieved. Interestingly, no systematic trend of δ_{GC} at different observational sites was found. For example, the values at the alpine mountain site Zugspitze ranged between 3.9 and 5.8 m^2g^{-1}, while they were only slightly different at the urban background site Leipzig-IfT, exhibiting values between 4.2 and 6.6 m^2g^{-1}. The average effect of individual air masses on δ_{GC} was also analyzed. It was found that δ_{GC} was relatively constant during the 2 maritime and the continental summer episodes with average values between 4 and 5 $m^2\,g^{-1}$. The most enhanced values of δ_{GC} were found for the aged continental air mass in winter with values between 5.5 and 6.5 m^2g^{-1}.

Values of δ_{GC} were compared to mass absorption coefficients concerning EC from a thermographic method (δ_{EC}). The values of δ_{EC} and δ_{GC} were found to be very similar at regional observation sites, but at a poorer correlation. Systematic, but slightly higher values of δ_{EC} were observed at urban observational sites, which could be attributed to a missing charring correction during the thermographic analysis.

The level of δ_{GC} were also compared to literature values, concluding that the δ_{GC} of the present study is at the lower bound of a broad range (3.6 - 18.3 m^2g^{-1}) of mass absorption coefficients measured in several previous studies in literature. However, it has to be mentioned, that in other studies absorption coefficients were mostly related to mass concentrations of EC. Nevertheless, the comparison within these literature values remains uncertain since different temperature programs for the EC mass determination and different methods for measuring absorption coefficients were used by researchers. It is an interesting observation that systematically higher values were determined if particle soot absorption photometers (PSAP) were used. The values of δ_{EC} from literature were, however, within the range of δ_{EC} and δ_{GC} of the present study if also MAAPs were applied. This suggests that the broad range is, to some extent, due to uncertainties in PSAP measurements (Müller et al., 2011), which were not used in this work. It can be summarized that conventionally used mass absorption coefficients might be too high and that an average value of 5 $m^2\,g^{-1}$ at 637 nm is more realistic.

The reason for enhanced values of δ_{GC} in the continental winter episode was explored by applying a Mie shell-core model using conditioned and unconditioned particle number size distributions, GC mass concentrations and absorption coefficients. It was found for maritime and continental air masses, that the measured absorption coefficients were almost entirely between the bounds given by simulated absorption coefficient assuming a completely external mixture and internal mixture, respectively. The difference between modeled and measured values could be iteratively minimized by introducing the fraction of external mixed soot particles. The time series of this variable suggests that a larger fraction of externally mixed soot particles occurred in the maritime winter air mass. In addition, lower mass absorption coefficients were found to be associated with higher externally mixed fractions from the microphysical optical model.

To finally estimate the radiative forcing caused by BC in the Central European troposphere, WRF-Chem was applied for the 2 week summer period 2009 containing the transition from the maritime to the continental episode. Before the calculation of radiative forcing, the model

was validated concerning the simulation of meteorological variables, aerosol mass concentrations and aerosol absorption coefficient. It was found that the model predicts temperatures too low, humidities too high and horizontal wind components slightly too high. Vertical stability conditions, however, were usually well reproduced, even in the planetary boundary layer. Particulate matter (PM_{10}) was overall well simulated with a mean normalized bias of -9 %. The aerosol column was relatively well represented, except some regions in southwestern Germany, which was explored by measurements of the aerosol optical thickness (AOT). However, the predicted BC mass concentrations were biased by -50 %. Despite the negative bias in BC mass concentrations, the dry absorption coefficient was slightly positively biased by 20 %. It has to be mentioned that the dry model absorption coefficients were used, since measurements were performed also on dried particles. In addition, the modeled mass absorption coefficients were scrutinized, because of the finding, that too high absorption coefficients were simulated in association with too low BC mass concentrations. It was found that modeled mass absorption coefficients were positively biased by about 110 % in comparison to δ_{GC} from measurements. The modeled values showed only little variation in the 2 week period and at all observational sites, as it was also found from measurements.

By a small sensitivity study of BC on the emission of this species, the simulation of BC could be improved by scaling the high resolution EUCAARI emission inventory. This was done by scaling it to a more suitable inventory from 2008, which is justified by the fact that the EUCAARI inventory represents the emission situation in 2005, whereas the simulated period was in 2009. In a second scaling procedure each grid cell was multiplied by a factor of 2, since BC emission estimates may vary by a factor of 2 - 5 on regional scale (Ramanathan and Carmichael, 2008). The simulation of BC could be significantly improved by using the inventory, which was scaled by the factor of 2. The modeled mass absorption coefficient was adjusted to measurements of δ_{GC} by varying the imaginary part of BC refractive index in the model. The resulting imaginary part was very low, which could be explained as a compensation for a missing external mixed particle fraction.

In the final step the radiative forcing of soot particles in Central Europe was determined from the model output. The maximum radiative forcing at the surface reached values up to -10 $W\,m^{-2}$ for the adjusted model run. At the top of the atmosphere, the radiative forcing is positive with values up to 4 $W\,m^{-2}$. These results show that the regional radiative forcing of BC and therefore its effect on regional scale maybe significantly higher than globally and annually averaged values as reported by the Intergovernmental Panel on Climate Change (IPCC, Forster et al. (2007)). It was also found that the forcing is lowered by around between 30 % and 70 % using the adjusted in comparison to the previous model settings.

The procedure of adjusting the modeled mass absorption coefficients to the measured values of δ_{GC} can be seen as a first approach to indirectly account for the real mixing state, at least in the optics module of a regional model, since the mass absorption coefficient and the BC mixing state are in a close relationship. The modeling results for the radiative forcing of BC at the surface and top of the atmosphere based on experimental values of δ_{GC} showed, that conventional model settings concerning the soot mixing state lead to an overestimation of the radiative forcing by around a factor of 2, as a result of treating BC as completely internally mixed instead of explic-

itly calculating the mixing state of this species. As a result, the direct and semi-direct effect of BC tends to be overestimated. The results of this work strongly suggest that the mixing state of soot has to be considered when calculating the aerosol optical properties in radiative transfer modules of regional models in future studies. Some approaches exist to explicitly simulate the mixing state of BC in a Box model (Oshima et al., 2009; Riemer et al., 2009). It has to be mentioned that implementing such an approach would further increase the computational time of regional aerosol models. Moreover, the present work showed the importance of directly measuring the mixing state atmospheric soot particles. Current techniques base on the principle of laser induced incandescence (Schwarz et al., 2006) or the volatile tandem differential mobility analyzer (VTDMA) technique as described in Wehner et al. (2009). Furthermore, the application of a VTDMA would allow for a determination of a 2 dimensional aerosol representation by measuring the particle number concentration as a function of the particle diameter and the non-volatile fraction, which is associated with soot (Rose et al., 2006). Such a two dimensional representation is also used in the box model of Oshima et al. (2009) for simulating the evolution of the soot mixing state. Nevertheless, the VTDMA technique for measuring the soot mixing state has still some uncertainties, since the non-volatile volume is not entirely decomposed of soot Engler et al. (2007). Further research is needed to explore the chemical composition of the non-volatile volume.

This work clearly showed that the soot mass absorption coefficient shows only little variation, even for a broad spectrum of atmospheric conditions. Additionally, the assumption of a completely internal mixture of soot particles in models deemed not suitable. The results rather suggest that a large fraction of soot particles exists in an external mixed state in the Central European troposphere, which has to be considered in future modeling studies. Taking this into account, the direct radiative forcing of soot particles may be significantly lower in comparison to the completely internal mixed case.

A. Chi-square minimization

If the deviation between a measured and a modeled quantity should be determined one approach is the minimization of χ^2 with

$$\chi^2(q) = \sum_{i=1}^{K} \left| \frac{s_i^{mod}(q) - s_i^{meas}}{s_i^{meas}} \right|^2 \tag{A.1}$$

with s_i^{meas} is the value of the i-th of K measurements and s_i^{mod} is the corresponding modeled value. When applying a model the result depends on several input parameters. For simplicity we assume that the model result depends only on one parameter q. The deviation between model and measurement is minimal if the derivative of $\chi^2(q)$ with respect to q is 0.

$$\chi^{2\prime}(q) = \frac{d\chi^2(q)}{dq} = 0 \tag{A.2}$$

Often the relation between q and s_i^{mod} is no simple function, so that equation A.2 can not be calculated directly. If this is the case an iterative method has to be used. A popular root finding algorithm is the Newton-Raphson method (Press et al., 1986). Following this algorithm, the root of the derivative can be found by repeating the procedure of calculating

$$\begin{aligned} \Delta q &= -\frac{\chi^{2\prime}(q)}{\chi^{2\prime\prime}(q)} \\ q_{new} &= q + \Delta q \end{aligned} \tag{A.3}$$

until q_{new} converges to a certain value. Calculating the derivatives numerically by central differences, equation A.3 can be rewritten as

$$\Delta q = \frac{(\chi^2(q+q\prime) - \chi^2(q-q\prime)) \cdot q\prime}{2 \cdot (\chi^2(q-q\prime) - 2 \cdot \chi^2(q) + \chi^2(q+q\prime))} \tag{A.4}$$

with the prime denotes a small change in q.

B. Model validation metrics

For the validation of a regional air quality model regarding e.g. simulated concentrations of chemical constituents different metrics can be used following definitions in Boylan and Russell (2006). The Mean Bias (MB) with

$$MB = \frac{1}{K}\sum_{i=1}^{K}(C_{m_i} - C_{o_i}) \tag{B.1}$$

can be regarded as the mean deviation between model C_m and observed C_o values over N time steps. In addition the Root Mean Error ($RMSE$) can be used which is defined as the square root of the mean squared error with

$$RMSE = \sqrt{\frac{1}{K}\sum_{i=1}^{K}(C_{m_i} - C_{o_i})^2} \tag{B.2}$$

Since these metrics give the deviation in terms of an absolute value (e.g. in $\mu\mathrm{g\,m^{-3}}$), a comparison of MB or $RMSE$ between locations with different concentration levels is not possible. To account for this the Mean Normalised Bias (MNB) with

$$MNB = \frac{1}{K}\sum_{i=1}^{K}\frac{(C_{m_i} - C_{o_i})}{C_{o_i}} \tag{B.3}$$

can be used which is the average observation-normalised deviation between model and observation. To quantify the model performance concerning e.g. the temporal behaviour of the concentration of a chemical constituent the Pearson Correlation Coefficient R with

$$R = \frac{\sum_{i=1}^{K}(C_{m_i} - \overline{C_m})(C_{o_i} - \overline{C_o})}{\sum_{i=1}^{K}(C_{m_i} - \overline{C_m})^2 \sum_{i=1}^{K}(C_{o_i} - \overline{C_o})^2} \tag{B.4}$$

can be used.

Bibliography

A. Ackerman, O. Toon, D. Stevens, A. Heymsfield, V. Ramanathan, and E. Welton. Reduction of Tropical Cloudiness by Soot. *Science*, 288(5468):1042–1047, 2000. doi: 10.1126/science.288.5468.1042.

T. Ackerman and O. Toon. Absorption of visible radiation in atmosphere containing mixtures of absorbing and nonabsorbing particles. *Applied Optics*, 20(20):3661–3667, 1981. doi: 10.1364/AO.20.003661.

M. Andreae and A. Gelencsér. Black carbon or brown carbon? the nature of light-absorbing carbonaceous aerosols. *Atmospheric Chemistry and Physics*, 6(10):3131–3148, 2006. doi: 10.5194/acp-6-3131-2006.

J. Barnard, J. Fast, G. Paredes-Miranda, W. Arnott, and A. Laskin. Technical note: Evaluation of the WRF-Chem aerosol chemical to aerosol optical properties module using data from the MILAGRO campaign. *Atmospheric Chemistry and Physics*, 10(15):7325–7340, 2010. doi: 10.5194/acp-10-7325-2010.

Y. Batonneau, S. Sobanska, J. Laureyns, and C. Bremard. Confocal Microprobe Raman Imaging of Urban Tropospheric Aerosol Particles. *Environmental Science & Technology*, 40(4):1300–1306, 2006. doi: 10.1021/es051294x.

M. Birch and R. Cary. Elemental Carbon-Based Method for Monitoring Occupational Exposures to Particulate Diesel Exhaust. *Aerosol Science and Technology*, 25(3):221–241, 1996. doi: 10.1080/02786829608965393.

W. Birmili, F. Stratmann, and A. Wiedensohler. Design of a DMA-based size spectrometer for a large particle size range and stable operation. *Journal of Aerosol Science*, 30(4):549–553, 1999. doi: 10.1016/S0021-8502(98)00047-0.

W. Birmili, K. Weinhold, S. Nordmann, A. Wiedensohler, G. Spindler, K. Müller, H. Herrmann, T. Gnauk, M. Pitz, J. Cyrys, H. Flentje, C. Nickel, T. Kuhlbusch, G. Löschau, D. Haase, F. Meinhardt, A. Schwerin, L. Ries, and K. Wirtz. Atmospheric aerosol measurements in the German Ultrafine Aerosol Network (GUAN) - Part 1 Soot and Particle Number Size Distributions. *Gefahrst. Reinh. Luft*, 69(2009):137–145, 2009.

W. Birmili, K. Heinke, M. Pitz, J. Matschullat, A. Wiedensohler, J. Cyrys, H. Wichmann, and A. Peters. Particle number size distributions in urban air before and after volatilisation. *Atmospheric Chemistry and Physics*, 10(10):4643–4660, 2010. doi: 10.5194/acp-10-4643-2010.

C. Bohren and D. Huffman. *Absorption and scattering of light by small particles*. Wiley Online Library, 1983.

T. Bond and R. Bergstrom. Light absorption by carbonaceous particles: An investigative review. *Aerosol Science and Technology*, 40(1):27–67, 2006. doi: 10.1080/02786820500421521.

T. Bond, T. Anderson, and D. Campbell. Calibration and Intercomparison of Filter-Based Measurements of Visible Light Absorption by Aerosols. *Aerosol Science and Technology*, 30 (6):582–600, 1999. doi: 10.1080/027868299304435.

T. Bond, D. Streets, K. Yarber, S. Nelson, J. Woo, and Z. Klimont. A technology-based global inventory of black and organic carbon emissions from combustion. *Journal of Geophysical Research*, 109(14):203, 2004. doi: 10.1029/2003JD003697.

J. Boylan and A. Russell. PM and light extinction model performance metrics, goals, and criteria for three-dimensional air quality models. *Atmospheric Environment*, 40(26):4946–4959, 2006. doi: 10.1016/j.atmosenv.2005.09.087.

Bruker. *Benutzerhandbuch für FT-Raman Modul FRA 106.*, 1994.

Bruker. *Benutzerhandbuch für das Fourier Spectrometer IFS 28 und IFS 55 EQUINOX®.*, 1995.

Bruker. *OPUS manual.*, 1999.

C. Cantrell. Technical note: Review of methods for linear least-squares fitting of data and application to atmospheric chemistry problems. *Atmospheric Chemistry and Physics*, 8(17): 5477–5487, 2008. doi: 10.5194/acp-8-5477-2008.

C. Carrico, M. Bergin, J. Xu, K. Baumann, and H. Maring. Urban aerosol radiative properties: Measurements during the 1999 Atlanta Supersite Experiment. *Journal of Geophysical Research*, 108(8422):10–1029, 2003. doi: 10.1029/2001JD001222.

F. Cavalli, M. Viana, K. Yttri, J. Genberg, and J. Putaud. Toward a standardised thermal-optical protocol for measuring atmospheric organic and elemental carbon: The EUSAAR protocol. *Atmospheric Measurement Techniques*, 3:79–89, 2010. doi: 10.5194/amt-3-79-2010.

E. Chapman, W. Gustafson Jr., R. Easter, J. Barnard, S. Ghan, M. Pekour, and J. Fast. Coupling aerosol-cloud-radiative processes in the WRF-chem model: Investigating the radiative impact of elevated point sources. *Atmospheric Chemistry and Physics*, 9(3):945–964, 2009. doi: 10.5194/acp-9-945-2009.

Y. Cheng, H. Eichler, A. Wiedensohler, J. Heintzenberg, Y. Zhang, M. Hu, H. Herrmann, L. Zeng, S. Liu, T. Gnauk, E. Brüggemann, and L. He. Mixing state of elemental carbon and non-light-absorbing aerosol components derived from in situ particle optical properties at Xinken in Pearl River Delta of China. *Journal of Geophysical Research*, 111(D20):D20204, 2006. doi: 10.1029/2005JD006929.

Y. Cheng, M. Berghof, R. Garland, A. Wiedensohler, B. Wehner, T. Müller, H. Su, Y. Zhang, P. Achtert, A. Nowak, U. Pöschl, T. Zhu, M. Hu, and L. Zeng. Influence of soot mixing state on aerosol light absorption and single scattering albedo during air mass aging at a polluted

regional site in northeastern China. *Journal of Geophysical Research*, 114(D2):D00G10, 2009. doi: 10.1029/2008JD010883.

M. Chou, M. Suarez, C. Ho, M. Yan, and K. Lee. Parameterizations for Cloud Overlapping and Shortwave Single-Scattering Properties for Use in General Circulation and Cloud Ensemble Models. *Journal of climate*, 11(2):202–214, 1998. doi: 10.1175/1520-0442(1998)011¡0202:PFCOAS¿2.0.CO;2.

J. Chow, J. Watson, L. Pritchett, W. Pierson, C. Frazier, and R. Purcell. The DRI thermal/optical reflectance carbon analysis system: Description, evaluation and applications in US air quality studies. *Atmospheric Environment*, 27(8):1185–1201, 1993. doi: 10.1016/0960-1686(93)90245-T.

P. Chuang, R. Duvall, M. Bae, A. Jefferson, J. Schauer, H. Yang, J. Yu, and J. Kim. Observations of elemental carbon and absorption during ACE-Asia and implications for aerosol radiative properties and climate forcing. *Journal of Geophysical Research*, 108(8634):15, 2003. doi: 10.1029/2002JD003254.

A. Clarke and K. Noone. Soot in the Arctic snowpack: A cause for perturbations in radiative transfer. *Atmospheric Environment (1967)*, 19(12):2045–2053, 1985. doi: 10.1016/0004-6981(85)90113-1.

W. Cooke and J. Wilson. A global black carbon aerosol model. *Journal of Geophysical Research*, 101(D14):19395–19, 1996. doi: 10.1029/96JD00671.

J. Cozic, B. Verheggen, E. Weingartner, J. Crosier, K. Bower, M. Flynn, H. Coe, S. Henning, M. Steinbacher, S. Henne, M. Collaud Coen, A. Petzold, and U. Baltensperger. Chemical composition of free tropospheric aerosol for PM1 and coarse mode at the high alpine site Jungfraujoch. *Atmospheric Chemistry and Physics*, 8(2):407–423, 2008. doi: 10.5194/acp-8-407-2008.

A. Cuesta, P. Dhamelincourt, J. Laureyns, A. Martinez-Alonso, and J. Tascón. Raman microprobe studies on carbon materials. *Carbon*, 32(8):1523–1532, 1994. doi: 10.1016/0008-6223(94)90148-1.

W. Demtröder. *Laserspektroskopie*, volume 4. Springer, 1993.

B. Dippel and J. Heintzenberg. Soot characterization in atmospheric particles from different sources by NIR FT Raman spectroscopy. *Journal of Aerosol Science*, 30, Supplement 1: S907S908, 1999. doi: 10.1016/S0021-8502(99)80464-9.

B. Dippel, H. Jander, and J. Heintzenberg. NIR FT Raman spectroscopic study of flame soot. *Physical Chemistry Chemical Physics*, 1(20):4707–4712, 1999. doi: 10.1039/A904529E.

J. Doran, J. Barnard, W. Arnott, R. Cary, R. Coulter, J. Fast, E. Kassianov, L. Kleinman, N. Laulainen, T. Martin, G. Paredes-Miranda, M. S. Pekour, W. J. Shaw, D. F. Smith, S. R. Springston, and X. Yu. The T1-T2 study: Evolution of aerosol properties downwind of Mexico city. *Atmospheric Chemistry and Physics*, 7(6):1585–1598, 2007. doi: 10.5194/acp-7-1585-2007.

R. Draxler and G. Hess. Description of the HYSPLIT4 modeling system. Technical report, NOAA Air Resources Laboratory, 1997.

M. Dresselhaus and G. Dresselhaus. Intercalation compounds of graphite. *Advances in Physics*, 30(2):139–326, 1981. doi: 10.1080/00018738100101367.

J. Ducret and H. Cachier. Particulate carbon content in rain at various temperate and tropical locations. *Journal of Atmospheric Chemistry*, 15(1):55–67, 1992. doi: 10.1007/BF00053609.

C. Engler, D. Rose, B. Wehner, A. Wiedensohler, E. Brüggemann, T. Gnauk, G. Spindler, T. Tuch, and W. Birmili. Size distributions of non-volatile particle residuals (D_p<800 nm) at a rural site in Germany and relation to air mass origin. *Atmospheric Chemistry and Physics*, 7(22):5785–5802, 2007. doi: 10.5194/acp-7-5785-2007.

J. Fast, W. Gustafson Jr, R. Easter, R. Zaveri, J. Barnard, E. Chapman, G. Grell, and S. Peckham. Evolution of ozone, particulates, and aerosol direct radiative forcing in the vicinity of Houston using a fully coupled meteorology-chemistry-aerosol model. *Journal of Geophysical Research*, 111(D21):D21305, 2006. doi: 10.1029/2005JD006721.

O. Favez, S. Alfaro, J. Sciare, H. Cachier, and M. Abdelwahab. Ambient measurements of light-absorption by agricultural waste burning organic aerosols. *Journal of Aerosol Science*, 40(7): 613–620, 2009. doi: 10.1016/j.jaerosci.2009.04.002.

P. Forster, V. Ramaswamy, P. Artaxo, T. Berntsen, R. Betts, D. Fahey, J. Haywood, J. Lean, D. Lowe, G. Myhre, J. Nganga, R. Prinn, G. Raga, M. Schulz, and R. Van Dorland. *Changes in Atmospheric Constituents and in Radiative Forcing. In: Climate Change 2007: The Physical Science Basis. Contribution of Working Group I to the Fourth Assessment Report of the Intergovernmental Panel on Climate Change*. Cambridge University Press, 2007.

A. Frey, D. Rose, B. Wehner, T. Müller, Y. Cheng, A. Wiedensohler, and A. Virkkula. Application of the Volatility-TDMA technique to Determine the Number Size Distribution and Mass Concentration of Less Volatile Particles. *Aerosol Science and Technology*, 42(10):817–828, 2008. doi: 10.1080/02786820802339595.

K. Fuller, W. Malm, and S. Kreidenweis. Effects of mixing on extinction by carbonaceous particles. *Journal of Geophysical Research*, 104(D13):15941–15954, 1999. doi: 10.1029/1998JD100069.

R. S. Gao, J. P. Schwarz, K. K. Kelly, D. W. Fahey, L. A. Watts, T. L. Thompson, J. R. Spackman, J. G. Slowik, E. S. Cross, J.-H. Han, P. Davidovits, T. B. Onasch, and D. R. Worsnop. A Novel Method for Estimating Light-Scattering Properties of Soot Aerosols Using a Modified Single-Particle Soot Photometer. *Aerosol Science and Technology*, 41(2):125–135, 2007. doi: 10.1080/02786820601118398.

M. Geb. Klimatologische Grundlagen der Luftmassenbestimmung. *Beilage zur Berliner Wetterkarte 50/81*, 1981.

S. Ghan, N. Laulainen, R. Easter, R. Wagener, S. Nemesure, E. Chapman, Y. Zhang, and R. Leung. Evaluation of aerosol direct radiative forcing in MIRAGE. *Journal of Geophysical Research*, 106(D6):5295–5316, 2001. doi: 10.1029/2000JD900502.

S. Gilardoni, E. Vignati, E. Marmer, F. Cavalli, C. Belis, V. Gianelle, A. Loureiro, and P. Artaxo. Sources of carbonaceous aerosol in the Amazon basin. *Atmospheric Chemistry and Physics*, 11(6):2747–2764, 2011. doi: 10.5194/acp-11-2747-2011.

G. Grell and D. Devenyi. A generalized approach to parameterizing convection combining ensemble and data assimilation techniques. *Geophysical Research Letters*, 29(14):1693, 2002. doi: 10.1029/2002GL015311.

G. Grell, S. Peckham, R. Schmitz, S. McKeen, G. Frost, W. Skamarock, and B. Eder. Fully coupled online chemistry within the WRF model. *Atmospheric Environment*, 39(37):6957–6975, 2005. doi: 10.1016/j.atmosenv.2005.04.027.

A. Guenther, T. Karl, P. Harley, C. Wiedinmyer, P. I. Palmer, and C. Geron. Estimates of global terrestrial isoprene emissions using MEGAN (Model of Emissions of Gases and Aerosols from Nature). *Atmospheric Chemistry and Physics*, 6(11):3181–3210, 2006. doi: 10.5194/acp-6-3181-2006.

S. Hasegawa and S. Ohta. Some measurements of the mixing state of soot-containing particles at urban and non-urban sites. *Atmospheric Environment*, 36(24):3899–3908, 2002. doi: 10.1016/S1352-2310(02)00343-6.

J. Haywood and K. Shine. Multi-spectral calculations of the direct radiative forcing of tropospheric sulphate and soot aerosols using a column model. *Quarterly Journal of the Royal Meteorological Society*, 123(543):1907–1930, 1997. doi: 10.1002/qj.49712354307.

J. Heintzenberg. Size-segregated measurements of particulate elemental carbon and aerosol light absorption at remote Arctic locations. *Atmospheric Environment (1967)*, 16(10):2461–2469, 1982. doi: 10.1016/0004-6981(82)90136-6.

J. Heintzenberg. Fine particles in the global troposphere A review. *Tellus B*, 41B(2):149–160, 1989. doi: 10.1111/j.1600-0889.1989.tb00132.x.

W. Hinds. *Aerosol technology: Properties, behavior, and measurement of airborne particles*. Wiley (New York), 1999.

R. Hitzenberger, A. Petzold, H. Bauer, P. Ctyroky, P. Pouresmaeil, L. Laskus, and H. Puxbaum. Intercomparison of thermal and optical measurement methods for elemental carbon and black carbon at an urban location. *Environmental Science and Technology*, 40(20):6377–6383, 2006. doi: 10.1021/es051228v.

B. Holben, T. Eck, I. Slutsker, D. Tanre, J. Buis, A. Setzer, E. Vermote, J. Reagan, Y. Kaufman, T. Nakajima, F. Lavenu, I. Jankowiak, and A. Smirnov. Aeronet A Federated instrument network and Data Archive for Aerosol Characterization. *Remote Sensing of Environment*, 66 (1):1–16, 1998. doi: 10.1016/S0034-4257(98)00031-5.

L. Huang, J. Brook, W. Zhang, S. Li, L. Graham, D. Ernst, A. Chivulescu, and G. Lu. Stable isotope measurements of carbon fractions (OC/EC) in airborne particulate: A new dimension for source characterization and apportionment. *Atmospheric Environment*, 40(15):2690–2705, 2006. doi: 10.1016/j.atmosenv.2005.11.062.

N. Ivleva, U. McKeon, R. Niessner, and U. Pöschl. Raman microspectroscopic analysis of size-resolved atmospheric aerosol particle samples collected with an ELPI: soot, humic-like substances, and inorganic compounds. *Aerosol Science and Technology*, 41(7):655–671, 2007. doi: 10.1080/02786820701376391.

M. Jacobson. Strong radiative heating due to the mixing state of black carbon in atmospheric aerosols. *Nature*, 409(6821):695–697, 2001. doi: 10.1038/35055518.

Z. Janjic. The Step-Mountain Eta Coordinate Model: Further Developments of the Convection, Viscous Sublayer, and Turbulence Closure Schemes. *Monthly Weather Review*, 122(5):927–945, 1994. doi: 10.1175/1520-0493(1994)122¡0897:NISTRU¿2.0.CO;2.

R. Johnson, J. Shah, R. Cary, and J. Huntzicker. An automated thermal-optical method for the analysis of carbonaceous aerosol. In *ACS Symposium Series*, volume 167, pages 223–233. ACS Publications, 1981.

Y. Kaufman and R. Fraser. Light Extinction by Aerosols during Summer Air Pollution. *Journal of Applied Meteorology*, 22(10):1694–1706, 1983. doi: 10.1175/1520-0450(1983)022¡1694:LEBADS¿2.0.CO;2.

S. Keller and J. Heintzenberg. Quantification of graphitic carbon on polycarbonate filters by Raman spectroscopy. *Journal of Aerosol Science*, 28, Supplement 1:609–610, 1997. doi: 10.1016/S0021-8502(97)85304-9.

W. Kelly and P. McMurry. Measurement of Particle Density by Inertial Classification of Differential Mobility Analyzer–Generated Monodisperse Aerosols. *Aerosol Science and Technology*, 17(3):199–212, 1992. doi: 10.1080/02786829208959571.

A. Khalizov, R. Zhang, D. Zhang, H. Xue, J. Pagels, and P. McMurry. Formation of highly hygroscopic soot aerosols upon internal mixing with sulfuric acid vapor. *Journal of Geophysical Research*, 114:D05208, 2009. doi: 10.1029/2008JD010595.

Z. Klimont, J. Cofala, I. Bertok, M. Amann, C. Heyes, and F. Gyarfas. Modelling particulate emissions in Europe: a framework to estimate reduction potential and control costs. Technical report, International Institute for Applied Systems Analysis, Laxenburg, Austria, 2002.

A. Knox, G. Evans, J. Brook, X. Yao, C. Jeong, K. Godri, K. Sabaliauskas, and J. Slowik. Mass Absorption Cross-Section of Ambient Black Carbon Aerosol in Relation to Chemical Age. *Aerosol Science and Technology*, 43(6):522–532, 2009. doi: 10.1080/02786820902777207.

Y. Kondo, L. Sahu, M. Kuwata, Y. Miyazaki, N. Takegawa, N. Moteki, J. Imaru, S. Han, T. Nakayama, N. Oanh, M. Hu, Y. J. Kim, and K. Kita. Stabilization of the Mass Absorption Cross Section of Black Carbon for Filter-Based Absorption Photometry by the use of a Heated Inlet. *Aerosol Science and Technology*, 43(8):741–756, 2009. doi: 10.1080/02786820902889879.

C. Kopp, A. Petzold, and R. Niessner. Investigation of the specific attenuation cross-section of aerosols deposited on fiber filters with a polar photometer to determine black carbon. *Journal of Aerosol Science*, 30(9):1153–1163, 1999. doi: 10.1016/S0021-8502(98)00786-1.

Ü. Köylü, G. Faeth, T. Farias, and M. Carvalho. Fractal and projected structure properties of soot aggregates. *Combustion and Flame*, 100(4):621–633, 1995. doi: 10.1016/0010-2180(94)00147-K.

K. Kupiainen and Z. Klimont. Primary emissions of submicron and carbonaceous particles in Europe and the potential for their control. Technical report, International Institute for Applied Systems Analysis, Laxenburg, Austria, 2004.

J. Lenoble. *Atmospheric radiative transfer*, volume 1. A. Deepak Pub, 1993.

R. Levy, L. Remer, S. Mattoo, E. Vermote, and Y. Kaufman. Second-generation operational algorithm: Retrieval of aerosol properties over land from inversion of Moderate Resolution Imaging Spectroradiometer spectral reflectance. *Journal of Geophysical Research*, 112:D13211, 2007. doi: 10.1029/2006JD007811.

Y. Lin, R. Farley, and H. Orville. Bulk Parameterization of the Snow Field in a Cloud Model. *Journal of Climate and Applied Meteorology*, 22(6):1065–1092, 1983. doi: 10.1175/1520-0450(1983)022¡1065:BPOTSF¿2.0.CO;2.

K. Liou. *An introduction to atmospheric radiation*, volume 84. Academic Press, 2002.

F. Liu, G. Smallwood, and D. Snelling. Effects of primary particle diameter and aggregate size distribution on the temperature of soot particles heated by pulsed lasers. *Journal of Quantitative Spectroscopy and Radiative Transfer*, 93(1-3):301–312, 2005. doi: 10.1016/j.jqsrt.2004.08.027.

N. Ma, C. Zhao, T. Müller, Y. Cheng, P. Liu, Z. Deng, W. Xu, L. Ran, B. Nekat, D. van Pinxteren, T. Gnauk, K. Müller, H. Herrmann, P. Yan, X. J. Zhou, and A. Wiedensohler. A new method to determine the mixing state of light absorbing carbonaceous using the measured aerosol optical properties and number size distributions. *Atmospheric Chemistry and Physics*, 12(5):2381–2397, 2012. doi: 10.5194/acp-12-2381-2012.

O. Mayol-Bracero, R. Gabriel, M. Andreae, T. Kirchstetter, T. Novakov, J. Ogren, P. Sheridan, and D. Streets. Carbonaceous aerosols over the Indian Ocean during the Indian Ocean Experiment (INDOEX): Chemical characterization, optical properties, and probable sources. *Journal of Geophysical Research*, 107:8030, 2002. doi: 10.1029/2000JD000039.

J. McConnell, R. Edwards, G. Kok, M. Flanner, C. Zender, E. Saltzman, J. Banta, D. Pasteris, M. Carter, and J. Kahl. 20th-Century Industrial Black Carbon Emissions Altered Arctic Climate Forcing. *Science*, 317(5843):1381–1384, 2007. doi: 10.1126/science.1144856.

S. Mertes, B. Dippel, and A. Schwarzenböck. Quantification of graphitic carbon in atmospheric aerosol particles by Raman spectroscopy and first application for the determination of mass absorption efficiencies. *Journal of Aerosol Science*, 35(3):347–361, 2004. doi: 10.1016/j.jaerosci.2003.10.002.

G. Mie. Beiträge zur Optik trüber medien, speziell kolloidaler Metallösungen. *Annalen der Physik*, 330(3):377–445, 1908. doi: 10.1002/andp.19083300302.

E. Mikhailov, S. Vlasenko, I. Podgorny, V. Ramanathan, and C. Corrigan. Optical properties of soot-water drop agglomerates: An experimental study. *Journal of Geophysical Research*, 111:D07209, 2006. doi: 10.1029/2005JD006389.

Y. Miyazaki, Y. Kondo, L. Sahu, J. Imaru, N. Fukushima, and M. Kano. Performance of a newly designed continuous soot monitoring system (COSMOS). *Journal of Environmental Monitoring*, 10(10):1195–1201, 2008. doi: 10.1039/B806957C.

H. Moosmüller, W. Arnott, C. Rogers, J. Chow, C. Frazier, L. Sherman, and D. Dietrich. Photoacoustic and filter measurements related to aerosol light absorption during the Northern Front Range Air Quality Study (Colorado 1996/1997). *Journal of Geophysical Research*, 103 (D21):28149–28157, 1998. doi: 10.1029/98JD02618.

T. Müller, A. Schladitz, A. Massling, N. Kaaden, K. Kandler, and A. Wiedensohler. Spectral absorption coefficients and imaginary parts of refractive indices of Saharan dust during SAMUM-1. *Tellus B*, 61(1):79–95, 2009. doi: 10.1111/j.1600-0889.2008.00399.x.

T. Müller, J. S. Henzing, G. de Leeuw, A. Wiedensohler, A. Alastuey, H. Angelov, M. Bizjak, M. Collaud Coen, J. E. Engström, C. Gruening, R. Hillamo, A. Hoffer, K. Imre, P. Ivanow, G. Jennings, J. Y. Sun, N. Kalivitis, H. Karlsson, M. Komppula, P. Laj, S.-M. Li, C. Lunder, A. Marinoni, S. Martins dos Santos, M. Moerman, A. Nowak, J. A. Ogren, A. Petzold, J. M. Pichon, S. Rodriquez, S. Sharma, P. J. Sheridan, K. Teinilä, T. Tuch, M. Viana, A. Virkkula, E. Weingartner, R. Wilhelm, and Y. Q. Wang. Characterization and intercomparison of aerosol absorption photometers: Result of two intercomparison workshops. *Atmospheric Measurement Techniques*, 4(2):245–268, 2011. doi: 10.5194/amt-4-245-2011.

H. Naoe, S. Hasegawa, J. Heintzenberg, K. Okada, A. Uchiyama, Y. Zaizen, E. Kobayashi, and A. Yamazaki. State of mixture of atmospheric submicrometer black carbon particles and its effect on particulate light absorption. *Atmospheric Environment*, 43(6):1296–1301, 2009. doi: 10.1016/j.atmosenv.2008.11.031.

R. Nessler, E. Weingartner, and U. Baltensperger. Effect of humidity on aerosol light absorption and its implications for extinction and the single scattering albedo illustrated for a site in the lower free troposphere. *Journal of Aerosol Science*, 36(8):958–972, 2005. doi: 10.1016/j.jaerosci.2003.10.002.

C. Neusüss, M. Pelzing, A. Plewka, and H. Herrmann. A new analytical approach for size-resolved speciation of organic compounds in atmospheric aerosol particles: Methods and first results. *Journal of Geophysical Research*, 105(D4):4513–4527, 2000. doi: 10.1029/1999JD901038.

S. Nordmann, W. Birmili, K. Weinhold, A. Wiedensohler, S. Mertes, K. Mller, T. Gnauk, H. Herrmann, M. Pitz, J. Cyrys, H. Flentje, L. Ries, and K. Wirtz. Atmospheric aerosol measurements in the German Ultrafine Aerosol Network (GUAN) - Part 2: Comparison of

measurements techniques for graphitic, light-absorbing, and elemental carbon, and the non-volatile particle volume under field conditions. *Gefahrst. Reinh. Luft*, 69(11/12):469–474, 2009.

T. Novakov, C. Corrigan, J. Penner, C. Chuang, O. Rosario, and O. Bracero. Organic aerosols in the Caribbean trade winds: A natural source? *Journal of Geophysical Research*, 102(D17): 21307–21313, 1997. doi: 10.1029/97JD01487.

J. Ogren and R. Charlson. Elemental carbon in the atmosphere: cycle and lifetime. *Tellus B*, 35(4):241–254, 1983. doi: 10.1111/j.1600-0889.1983.tb00027.x.

J. Ogren, P. Groblicki, and R. Charlson. Measurement of the removal rate of elemental carbon from the atmosphere. *Science of the Total Environment*, 36:329–338, 1984. doi: 10.1016/0048-9697(84)90284-5.

N. Oshima, M. Koike, Y. Zhang, Y. Kondo, N. Moteki, N. Takegawa, and Y. Miyazaki. Aging of black carbon in outflow from anthropogenic sources using a mixing state resolved model: Model development and evaluation. *Journal of Geophysical Research*, 114:D06210, 2009. doi: 10.1029/2008JD010680.

K. Park, F. Cao, D. Kittelson, and P. McMurry. Relationship between particle mass and mobility for diesel exhaust particles. *Environmental Science & Technology*, 37(3):577–583, 2003. doi: 10.1021/es025960v.

K. Park, D. Kittelson, and P. McMurry. Structural properties of diesel exhaust particles measured by transmission electron microscopy (TEM): Relationships to particle mass and mobility. *Aerosol Science and Technology*, 38(9):881–889, 2004a. doi: 10.1080/027868290505189.

K. Park, D. Kittelson, M. Zachariah, and P. McMurry. Measurement of inherent material density of nanoparticle agglomerates. *Journal of Nanoparticle Research*, 6(2):267–272, 2004b. doi: 10.1023/B:NANO.0000034657.71309.e6.

J. Penner and T. Novakov. Carbonaceous particles in the atmosphere: A historical perspective to the Fifth International Conference on Carbonaceous Particles in the Atmosphere. *Journal of Geophysical Research*, 101(D14):19373–19378, 1996. doi: 10.1029/96JD01175.

A. Peters, E. Liu, R. Verrier, J. Schwartz, D. Gold, M. Mittleman, J. Baliff, J. Oh, G. Allen, K. Monahan, and D. Dockery. Air Pollution and Incidence of Cardiac Arrhythmia. *Epidemiology*, 11(1):11–17, 2000.

A. Petzold and Nießner. Coloumetrische Messung der Rußbelastung in der Außenluft- Verfahrensentwicklung und Anwendung an Meßstellen unterschiedlicher belastung. *Gefahrst. Reinh. Luft*, 56:173–177, 1996.

A. Petzold and R. Niessner. Photoacoustic soot sensor for in-situ black carbon monitoring. *Applied Physics B: Lasers and Optics*, 63(2):191–197, 1996. doi: 10.1007/BF01095272.

A. Petzold and M. Schönlinner. Multi-angle absorption photometry–a new method for the measurement of aerosol light absorption and atmospheric black carbon. *Journal of Aerosol Science*, 35(4):421–441, 2004. doi: 10.1016/j.jaerosci.2003.09.005.

A. Petzold, H. Schloesser, P. Sheridan, W. Arnott, J. Ogren, and A. Virkkula. Evaluation of multiangle absorption photometry for measuring aerosol light absorption. *Aerosol Science and Technology*, 39(1):40–51, 2005. doi: 10.1080/027868290901945.

A. Petzold, K. Rasp, B. Weinzierl, M. Esselborn, T. Hamburger, A. Dörnbrack, K. Kandler, L. Schütz, P. Knippertz, M. Fiebig, and A. Virkkula. Saharan dust absorption and refractive index from aircraft-based observations during SAMUM 2006. *Tellus B*, 61(1):118–130, 2009. doi: 10.1111/j.1600-0889.2008.00383.x.

W. Press, B. Flanner, S. Teukolsky, and W. Vetterling. *Numerical recipes*, volume 547. Cambridge University Press, 1986.

K. Ram, M. Sarin, and P. Hegde. Long-term record of aerosol optical properties and chemical composition from a high-altitude site (Manora Peak) in Central Himalaya. *Atmospheric Chemistry and Physics*, 10(23):11791–11803, 2010. doi: 10.5194/acp-10-11791-2010.

C. Raman and K. Krishnan. A new type of secondary radiation. *Nature*, 121(3048):501–502, 1928.

V. Ramanathan and G. Carmichael. Global and regional climate changes due to black carbon. *Nature Geoscience*, 1(4):221–227, 2008. doi: 10.1038/ngeo156.

S. Reich and C. Thomsen. Raman spectroscopy of graphite. *Philosophical Transactions of the Royal Society of London. Series A: Mathematical, Physical and Engineering Sciences*, 362 (1824):2271–2288, 2004. doi: 10.1098/rsta.2004.1454 1471-2962.

L. Remer, Y. Kaufman, D. Tanré, S. Mattoo, D. Chu, J. Martins, R. Li, C. Ichoku, R. Levy, R. Kleidman, T. Eck, E. Vermote, and B. Holben. The MODIS Aerosol Algorithm, Products, and Validation. *Journal of the Atmospheric Sciences*, 62(4):947–973, 2005. doi: 10.1175/JAS3385.1.

N. Riemer, M. West, R. Zaveri, and R. Easter. Simulating the evolution of soot mixing state with a particle-resolved aerosol model. *Journal of Geophysical Research*, 114(D9):D09202, 2009. doi: 10.1029/2008JD011073.

D. Rose, B. Wehner, M. Ketzel, C. Engler, J. Voigtländer, T. Tuch, and A. Wiedensohler. Atmospheric number size distributions of soot particles and estimation of emission factors. *Atmospheric Chemistry and Physics*, 6(4):1021–1031, 2006. doi: 10.5194/acp-6-1021-2006.

H. Rosen and T. Novakov. Raman scattering and the characterisation of atmospheric aerosol particles. *Nature*, 266:708–710, 1977. doi: 10.1038/266708a0.

A. Sadezky, H. Muckenhuber, H. Grothe, R. Niessner, and U. Pöschl. Raman microspectroscopy of soot and related carbonaceous materials: Spectral analysis and structural information. *Carbon*, 43(8):1731–1742, 2005. doi: 10.1016/j.carbon.2005.02.018.

M. Schaap, R. Timmermans, R. Koelemeijer, G. de Leeuw, and P. Builtjes. Evaluation of MODIS aerosol optical thickness over Europe using sun photometer observations. *Atmospheric Environment*, 42(9):2187–2197, 2008. doi: 10.1016/j.atmosenv.2007.11.044.

J. Schauer, G. Lough, M. Shafer, W. Christensen, M. Arndt, J. DeMinter, and J. Park. Characterization of metals emitted from motor vehicles. Technical report, Health Effects Institute, 2006.

H. Schmid, L. Laskus, H. J. Abraham, U. Baltensperger, V. Lavanchy, M. Bizjak, P. Burba, H. Cachier, D. Crow, J. Chow, T. Gnauk, A. Even, H. ten Brink, K.-P. Giesen, R. Hitzenberger, C. Hueglin, W. Maenhaut, C. Pio, A. Carvalho, J.-P. Putaud, D. Toom-Sauntry, and H. Puxbaum. Results of the carbon conference international aerosol carbon round robin test stage i. *Atmospheric Environment*, 35(12):2111 – 2121, 2001. ISSN 1352-2310. doi: 10.1016/S1352-2310(00)00493-3.

J. Schmid, B. Grob, R. Niessner, and N. Ivleva. Multiwavelength Raman Microspectroscopy for Rapid Prediction of Soot Oxidation Reactivity. *Analytical Chemistry*, 83(4):1173–1179, 2011. doi: 10.1021/ac102939w.

J. Schwarz, R. Gao, D. Fahey, D. Thomson, L. Watts, J. Wilson, J. Reeves, M. Darbeheshti, D. Baumgardner, G. Kok, S. H. Chung, M. Schulz, J. Hendricks, A. Lauer, B. Kärcher, J. Slowik, K. Rosenhof, T. L. Thompson, A. Langford, M. Loewenstein, and K. Aikin. Single-particle measurements of midlatitude black carbon and light-scattering aerosols from the boundary layer to the lower stratosphere. *Journal of Geophysical Research*, 111:D16207, 2006. doi: 10.1029/2006JD007076.

J. Sciare, H. Bardouki, C. Moulin, and N. Mihalopoulos. Aerosol sources and their contribution to the chemical composition of aerosols in the Eastern Mediterranean Sea during summertime. *Atmospheric Chemistry and Physics*, 3(1):291–302, 2003. doi: 10.5194/acp-3-291-2003.

M. Shiraiwa, Y. Kondo, T. Iwamoto, and K. Kita. Amplification of Light Absorption of Black Carbon by Organic Coating. *Aerosol Science and Technology*, 44(1):46–54, 2010. doi: 10.1080/02786820903357686.

W. Skamarok, J. Klemp, J. Dudhia, D. Gill, D. Barker, M. Duda, X. Huan, W. Wang, and J. Powers. A Description of the Advanced Research WRF Version 3. Technical report, National Center for Atmospheric Research, Boulder, Colorado, 2008.

D. Streets, S. Gupta, S. Waldhoff, M. Wang, T. Bond, and B. Yiyun. Black carbon emissions in China. *Atmospheric Environment*, 35(25):4281–4296, 2001. doi: 10.1016/S1352-2310(01)00179-0.

R. Stull. *An introduction to boundary layer meteorology*, volume 13. Springer, 1988.

H. Sun, L. Biedermann, and T. Bond. Color of brown carbon: A model for ultraviolet and visible light absorption by organic carbon aerosol. *Geophysical Research Letters*, 34(17):L17813, 2007. doi: 10.1029/2007GL029797.

H. ten Brink, W. Maenhaut, R. Hitzenberger, T. Gnauk, G. Spindler, A. Even, X. Chi, H. Bauer, H. Puxbaum, J. Putaud, J. Tursic, and A. Berner. INTERCOMP2000: the comparability of methods in use in Europe for measuring the carbon content of aerosol. *Atmospheric Environment*, 38(38):6507–6519, 2004. doi: 10.1016/j.atmosenv.2004.08.027.

G. Thomas and K. Stamnes. *Radiative transfer in the atmosphere and ocean.* Cambridge University Press, 2002.

C. Thomsen and S. Reich. Double Resonant Raman Scattering in Graphite. *Physical Review Lletters*, 85(24):5214–5217, 2000. doi: 10.1103/PhysRevLett.85.5214.

P. Tuccella, G. Curci, G. Visconti, B. Bessagnet, L. Menut, and R. Park. Modeling of gas and aerosol with WRF/Chem over Europe: Evaluation and sensitivity study. *Journal of Geophysical Research*, 117:D03303, 2012. doi: 10.1029/2011JD016302.

F. Tuinstra and J. Koenig. Raman spectrum of Graphite. *Journal of Chemical Physics*, 53(3): 1126–1130, 1970. doi: 10.1063/1.1674108.

VDI 2465 Part 1: Measurement of soot (immission) chemical analysis of elemental carbon by extraction and thermal desorption of organic carbon. VDI/DIN-Handbuch Reinhaltung der Luft, 1996.

VDI 2465 Part 2: Measurement of soot (ambient air), thermographic determination of elemental carbon after thermal desorption of organic carbon. VDI/DIN-Handbuch Reinhaltung der Luft, 1999.

E. Vignati, M. Karl, M. Krol, J. Wilson, P. Stier, and F. Cavalli. Sources of uncertainties in modelling black carbon at the global scale. *Atmospheric Chemistry and Physics*, 10(6): 2595–2611, 2010. doi: 10.5194/acp-10-2595-2010.

A. Virkkula, N. Ahlquist, D. Covert, W. Arnott, P. Sheridan, P. Quinn, and D. Coffman. Modification, Calibration and a Field Test of an Instrument for Measuring Light Absorption by Particles. *Aerosol Science and Technology*, 39(1):68–83, 2005. doi: 10.1080/027868290901963.

B. Wehner, S. Philippin, and A. Wiedensohler. Design and calibration of a thermodenuder with an improved heating unit to measure the size-dependent volatile fraction of aerosol particles. *Journal of Aerosol Science*, 33(7):1087–1093, 2002. doi: 10.1016/S0021-8502(02)00056-3.

B. Wehner, M. Berghof, Y. Cheng, P. Achtert, W. Birmili, A. Nowak, A. Wiedensohler, R. Garland, U. Pöschl, M. Hu, and T. Zhu. Mixing state of nonvolatile aerosol particle fractions and comparison with light absorption in the polluted Beijing region. *Journal of Geophysical Research*, 114:D00G17, 2009. doi: 10.1029/2008JD010923.

E. Weingartner, H. Burtscher, and U. Baltensperger. Hygroscopic properties of carbon and diesel soot particles. *Atmospheric Environment*, 31(15):2311–2327, 1997. doi: 10.1016/S1352-2310(97)00023-X.

M. Wentzel, H. Gorzawski, K. Naumann, H. Saathoff, and S. Weinbruch. Transmission electron microscopical and aerosol dynamical characterization of soot aerosols. *Journal of Aerosol Science*, 34(10):1347–1370, 2003. doi: 10.1016/S0021-8502(03)00360-4.

H. Wex, C. Neusüß, M. Wendisch, F. Stratmann, C. Koziar, A. Keil, A. Wiedensohler, and M. Ebert. Particle scattering, backscattering, and absorption coefficients: An in situ closure and sensitivity study. *Journal of Geophysical Research*, 107:8122, 2002. doi: 10.1029/2000JD000234.

A. Wiedensohler, W. Birmili, A. Nowak, A. Sonntag, K. Weinhold, M. Merkel, B. Wehner, T. Tuch, S. Pfeifer, M. Fiebig, A. M. Fjäraa, E. Asmi, K. Sellegri, R. Depuy, H. Venzac, P. Villani, P. Laj, P. Aalto, J. A. Ogren, E. Swietlicki, P. Williams, P. Roldin, P. Quincey, C. Hüglin, R. Fierz-Schmidhauser, M. Gysel, E. Weingartner, F. Riccobono, S. Santos, C. Grüning, K. Faloon, D. Beddows, R. Harrison, C. Monahan, S. G. Jennings, C. D. O'Dowd, A. Marinoni, H.-G. Horn, L. Keck, J. Jiang, J. Scheckman, P. H. McMurry, Z. Deng, C. S. Zhao, M. Moerman, B. Henzing, G. de Leeuw, G. Löschau, and S. Bastian. Mobility particle size spectrometers: Harmonization of technical standards and data structure to facilitate high quality long-term observations of atmospheric particle number size distributions. *Atmospheric Measurement Techniques*, 5(3):657–685, 2012. doi: 10.5194/amt-5-657-2012.

R. Zaveri, R. Easter, J. Fast, and L. Peters. Model for simulating aerosol interactions and chemistry (MOSAIC). *Journal of Geophysical Research*, 113:D13204, 2008. doi: 10.1029/2007JD008782.

Acknowledgement

I want to thank all persons who contributed to this work, especially:

- Alfred Wiedensohler (IfT, Leipzig) and Wolfram Birmili (IfT, Leipzig) for their supervision.
- Yafang Cheng (MPI, Mainz, Germany), who supported me in getting all the skills that were needed for the modeling part of this work and for preparing the emission inventory.
- Gregory R. Carmichael (CGRER, University of Iowa, USA) for giving me the chance working at CGRER and learning more about the WRF-Chem modeling system.
- Kay Weinhold (IfT, Leipzig), for his help in evaluating the GUAN data and for his great experimental efforts for assuring the quality of this data set.
- Michael Panzer, for making lots of the Raman measurements presented in this work.
- Denier van der Gon (TNO, Utrecht, Netherlands) for providing the high resolution EU-CAARI EC/OC emission inventory used in the present work.
- Susan Klose (Umweltbundesamt, Germany), for providing the PM_{10} data set used for model evaluation.
- My family, for all their support and their motivating words in the past years.

I would particularly like to thank the Deutsche Bundestiftung Umwelt (DBU, Osnabrück, Germany) for generously supporting this work by their doctoral scholarship programme.